X-622-69-216

PREPRINT

NASA TM X-63564

BIDIRECTIONAL REFLECTANCE MEASUREMENTS FROM AN AIRCRAFT OVER NATURAL EARTH SURFACES

BARBARA BRENNAN

MAY 1969

GSFC

GODDARD SPACE FLIGHT CENTER

GREENBELT, MARYLAND

X-622-69-216

BIDIRECTIONAL REFLECTANCE MEASUREMENTS FROM AN AIRCRAFT OVER NATURAL EARTH SURFACES

Barbara Brennan

MAY 1969

Goddard Space Flight Center
Greenbelt, Maryland

TABLE OF CONTENTS

BIDIRECTIONAL REFLECTANCE MEASUREMENTS FROM AN AIRCRAFT OVER NATURAL EARTH SURFACES

INTRODUCTION

As part of a program to determine the reflectance patterns of solar radiation from natural surfaces, measurements were made over a variety of surfaces with a scanning radiometer mounted on a CV-990 aircraft. Of particular interest was the reflectance pattern dependence on surface type and solar zenith angle. Since many present meteorological satellites utilize narrow beam scanning radiometers and are not capable of measuring reflected energy in all directions, reflectance patterns for natural earth surfaces are needed to interpret these measurements in terms of the albedo of the earth.

INSTRUMENTATION

During the spring of 1966 and 1967 reflectance measurements were made with a Medium Resolution Infrared Radiometer (MRIR)* flown on NASA's Convair-990 high altitude research aircraft. This radiometer was a model of the MRIR instrument flown on the Nimbus meteorological satellites.

The MRIR is composed of five Casagrainian telescopes which focus incoming radiation reflected from a scan mirror into five optical channels characterized by different filters. Thermistor bolometers are used as detectors in all its channels.

A photograph of the MRIR is shown in Fig. 1. The scan mirror is mounted at an inclination of 45° to the axes of the telescopes on the left, seen reflected in the scan mirror. The scan mirror rotates so that the 50 milliradian instantaneous field of view scans through a 360° arc in a plane perpendicular to the axis of rotation in 7-1/2 seconds. The aircraft-borne instrument, shown inside an aerodynamic fairing in Fig. 2, scans in the vertical plane containing the longitudinal axis of the aircraft. Scanning is fore-to-aft in the downward looking direction, as depicted in Fig. 3.

*The term "Medium Resolution Infra-red Radiometer" (MRIR) is actually a misnomer, since the satellite instrument contains a channel which responds in part to visible radiation (.2μ to 4μ), and the airborne instrument contains two such channels (0.55μ to 0.85μ, and 0.2μ to 4μ). However, the term "MRIR" has been so widely adopted as to compel its use here.

Three MRIR channels are sensitive to infrared radiation. The other two, sensitive to solar radiation in the intervals 0.55-0.85μ and 0.2-4μ, were used in this study. Their effective spectral response functions are shown in Fig. 4.

DEFINITION OF TERMS

The geometric relationships involved in a study of cloud reflectances are shown in Fig. 5. Energy from the sun impinges on the earth's surface at a zenith angle ζ_0 and is reflected at a zenith angle θ, with an azimuth angle ϕ measured with respect to the principal plane of the sun from the forward scattering direction. The amount of energy reflected is generally dependent on these three angles. For this study, the reflectance zenith and viewing nadir angles can be considered to be equal.*

The term bidirectional reflectance is often used to characterize the reflection of a beam of solar radiation from a plane surface (as illustrated in Fig. 5). The effective bidirectional reflectance $\overline{\rho}$ can be expressed mathematically by

$$\overline{\rho}(\theta, \phi, \zeta_0) = \frac{\overline{N}(\theta, \phi, \zeta_0)}{\overline{H}^* \cos \zeta_0} \ (\text{ster}^{-1}) \tag{1}$$

where $\overline{N}(\theta, \phi, \zeta_0)$ is the effective radiance measured by a narrow beam radiometer, i.e., the integral over all wavelengths of the product of the actual radiance at the radiometer and the appropriate spectral response function shown in Fig. 4.

$\overline{H^*}$ is the effective solar irradiance and is obtained by integrating the product of the spectral solar irradiance, H^*_λ and the appropriate spectral response function ϕ_λ shown in Fig. 4 over all wavelengths.

$$\overline{H}^* = \int_0^\infty H^*_\lambda \, \phi_\lambda \, d\lambda \tag{2}$$

(The spectral solar irradiance given by Johnston[2] was used here.)

*A beam emerging from the surface at a zenith angle of 90° is observed at a nadir angle of 87° from an aircraft flying at an altitude of 40,000 feet. The difference between the two angles decreases to 0° as the viewing nadir angle goes to 0.

The effective directional reflectance, $\overline{R}(\zeta_0)$, may be obtained by integrating the effective bidirectional reflectance over the upward hemisphere, once the dependence of $\overline{\rho}$ on θ, ϕ, and ζ_0 is known. The effective directional reflectance can be expressed mathematically by

$$\overline{R}(\zeta_0) = \int_0^{2\pi} \int_0^{\pi/2} \overline{\rho}(\theta, \phi, \zeta_0) \cos\theta \sin\theta \, d\theta \, d\phi \qquad (3)$$

From Eq. (3) it follows that the directional reflectance of an isotropically reflecting surface is $\pi\overline{\rho}$.

Albedo is defined as the ratio of the amount of electromagnetic radiation reflected by a body to the amount incident upon it.[3] Measured earth surface albedoes, however, are dependent on the time and spectral interval of the measurements. For global heat balance studies, Raschke defines albedo as ". . . that part of the daily incoming flux of solar radiation which is reflected back to space.[4]" The daily time-averaged effective albedo $\overline{A}$ may be found by integrating the measured effective directional reflectances with respect to time from sunrise (t_1) to sunset (t_2),

$$\overline{A} = \frac{\int_{t_1}^{t_2} \overline{R}(\zeta_0(t) \cos \zeta_0(t) \, dt}{\int_{t_1}^{t_2} \cos \zeta_0(t) \, dt}. \qquad (4)$$

The albedo of a constant surface may be obtained from narrow beam satellite measurements, $\overline{N}(\theta, \phi, \zeta_0)$ once models for the spectral and time dependent functions are made.

EXPERIMENTAL PROCEDURE AND DATA REDUCTION

To measure effective radiance, for effective directional reflectance calculations with the aircraft-borne MRIR, it is advantageous to take measurements at as many nadir angles and azimuthal directions as possible. Since the solar zenith angle and cloud patterns are constantly changing, it is necessary to

measure the effective bidirectional reflectance of a surface in as short a time as possible. The CV-990, however, requires ten minutes just to turn around to change azimuthal direction. The rosette flight pattern, shown in Fig. 6, was chosen as a compromise between requirements for a large number of azimuthal directions on the one hand and a fairly short period of time required to fly the pattern on the other. With this one-and-a-half hour flight pattern, effective bidirectional reflectances with nadir angles ($0 \leq \theta \leq 90°$) are measured in five azimuths). By assuming symmetry around the principal plane, (directions 1 and 2 in Fig. 6), effective bidirectional reflectances are obtained for eight directions. These reflectance measurements are then integrated over a hemisphere to obtain effective directional reflectance.

The rosette pattern was changed in 1967, to check the assumptions of symmetry around the principal plane of the sun, to that shown in Fig. 7.

Each leg of a rosette lasted four to eight minutes, yielding thirty-two to sixty-four MRIR scans. These data were averaged by a computer in 1° nadir angle steps for each leg to produce one set of $\overline{\rho}(\theta, \phi, \zeta_0)$ vs. θ values for each leg. $\overline{\rho}(\theta, \phi, \zeta_0)$ was integrated numerically from $\theta = 0°$ to $\theta = \pi/2$ for a given azimuthal direction by Eq. (3). Each integrated value was plotted against ϕ and a curve was fitted through the points. The area under the curve was measured with a planimeter in order to find the effective directional reflectance.

RESULTS

Table I, (page 14) lists flight number, type of surface, aircraft and surface height, range of solar zenith angles over which a complete rosette was flown, and the calculated directional reflectance.

Table II, (page 61), lists flight number, type of surface, aircraft and surface height, and the range of solar zenith angles over which measurements in the principal plane of the sun where made.

The average bidirectional reflectances are plotted against nadir angle for each azimuth direction, and a polar plot for each complete rosette with isopleths of bidirectional reflectance is shown in Figs. 8-74.

Clouds, (Figs. 8-37, and 57-65) show a strong forward scattering peak and a slight backscattering peak with a minimum around the nadir. Measurements in the .2-4μ band are generally lower than those in the .55-.85μ region indicating that albedo measurements should not be taken in a narrow spectral interval but rather, should be taken in a wide interval encompassing as much of the solar spectrum as possible.

The ocean surfaces, shown in Figs. 46-53, and 66-74, show a slight back scattering peak with stronger forward scattering. The reflectance pattern is influenced by sun glitter in the forward scattering direction.

A forest, Figs. 38-45, shows a pattern similar to the strato cumulus pattern with strong forward and backward scattering with a minimum at low nadir angles. Bidirectional reflectances observed over sandy desert soils show very little anisotropy, as can be seen in Figs. 54-56. A slight back scattering peak has been observed in sand and grassland for very low sun angles by Salomonson[5] and Coulson, et al.[6] The measurements presented here do not show a forward scattering peak, presumably because the sun is not low enough in the sky to produce it.

The reflectance of most of the earth surfaces measured shows strong anisotropy, especially in the principal plane of the sun. The degree of anisotropy is dependent on the type of surface and generally increases with increasing solar zenith angle.

REFERENCES

1. K. L. Coulson, "Effect of Surface Reflection on the Angular and Spectral Distribution of Skylight," J.A.S. 25, 759-770, (1968).

2. Johnston, Satellite Environment Handbook, (Stanford Univ. Press, Stanford, 1961).

3. R. E. Huschke, Glossary of Meteorology, American Meteorological Society, Boston, Mass., (1959).

4. E. Raschke, "The Radiation Balance of the Earth-Atmosphere System from Radiation Measurements of the Nimbus II Meteorological Satellite," NASA Tech. Note TN D-4589, Washington, D.C., (1968).

5. V. V. Salomonson, "Anisotropy in Reflected Solar Radiation," Ph. D. Thesis, Atmospheric Science Technical Paper No. 128, Colorado State University, Fort Collins, (1968).

6. K. K. Coulson, G. M. Bouricius and E. L. Gray, "Optical Reflection Properties of Natural Surfaces," J. Geophys. Res., 70, 4601 (1965).

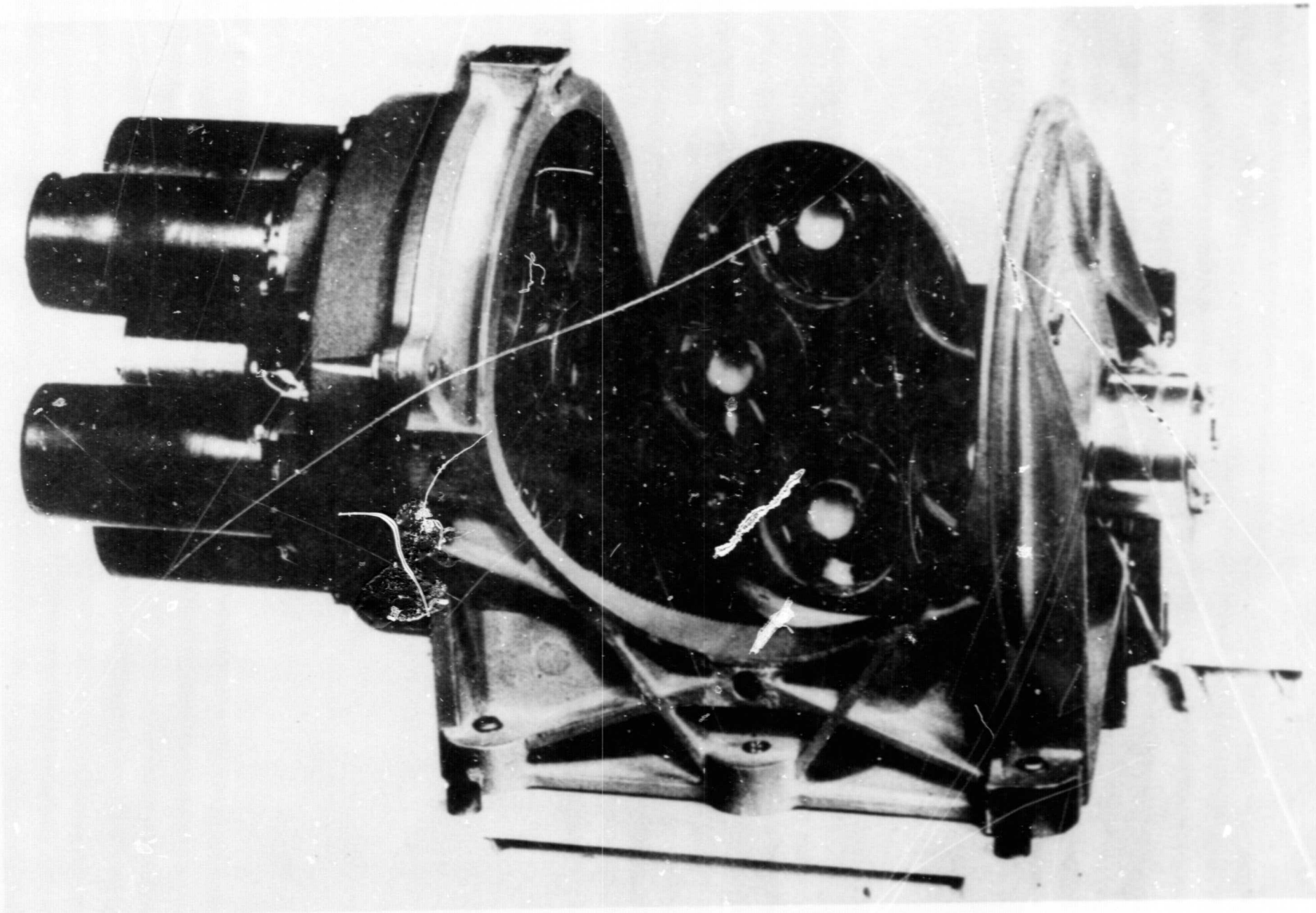

Figure 1–Medium Resolution Infrared Radiometer (MRIR).

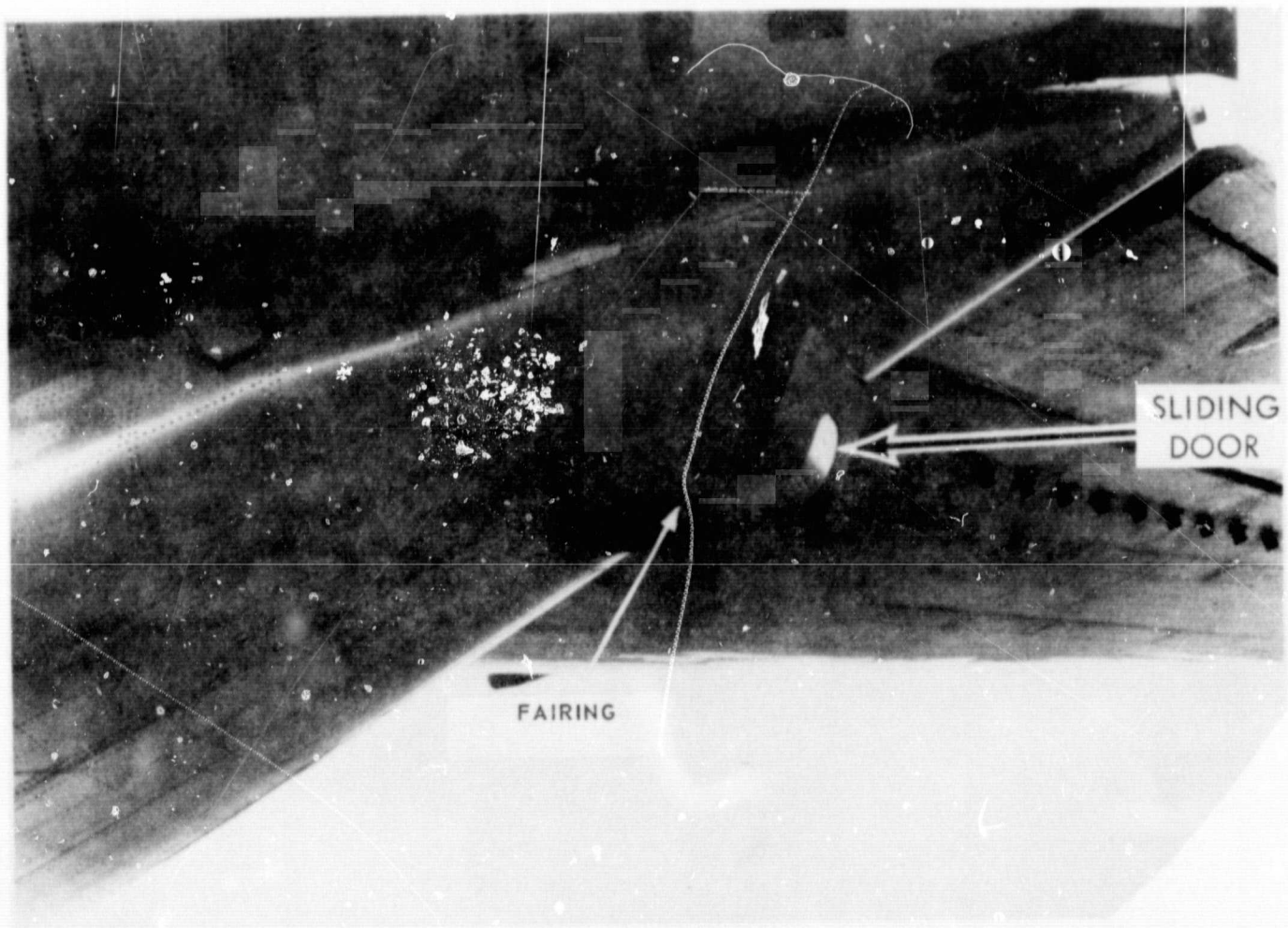

Figure 2–MRIR mounted on aircraft fairing.

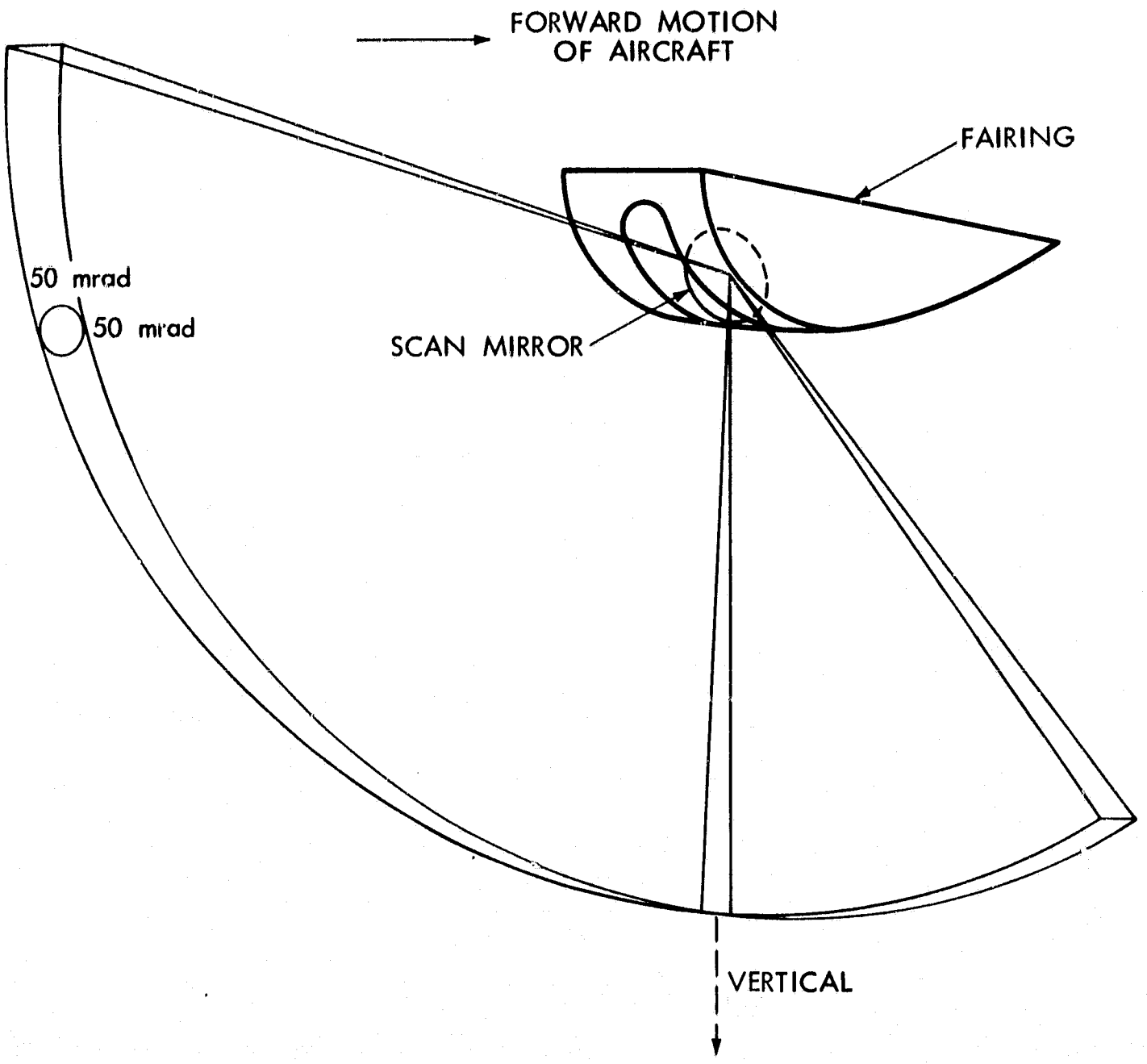

Figure 3–Earth-Sky portion of scan of MRIR mounted on jet aircraft.

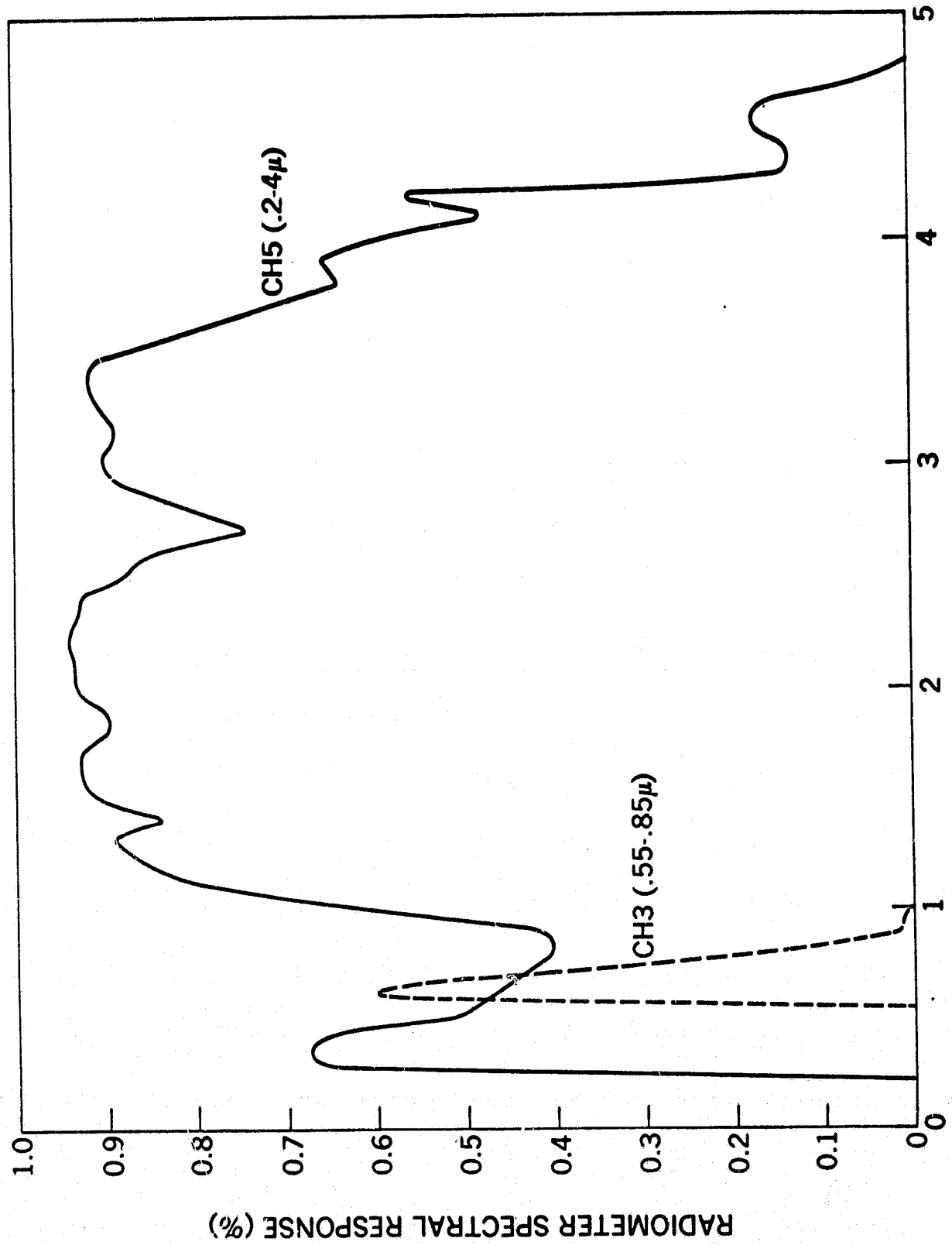

Figure 4–Spectral response of the two visible channels of the Nimbus Medium Resolution Infrared Radiometer.

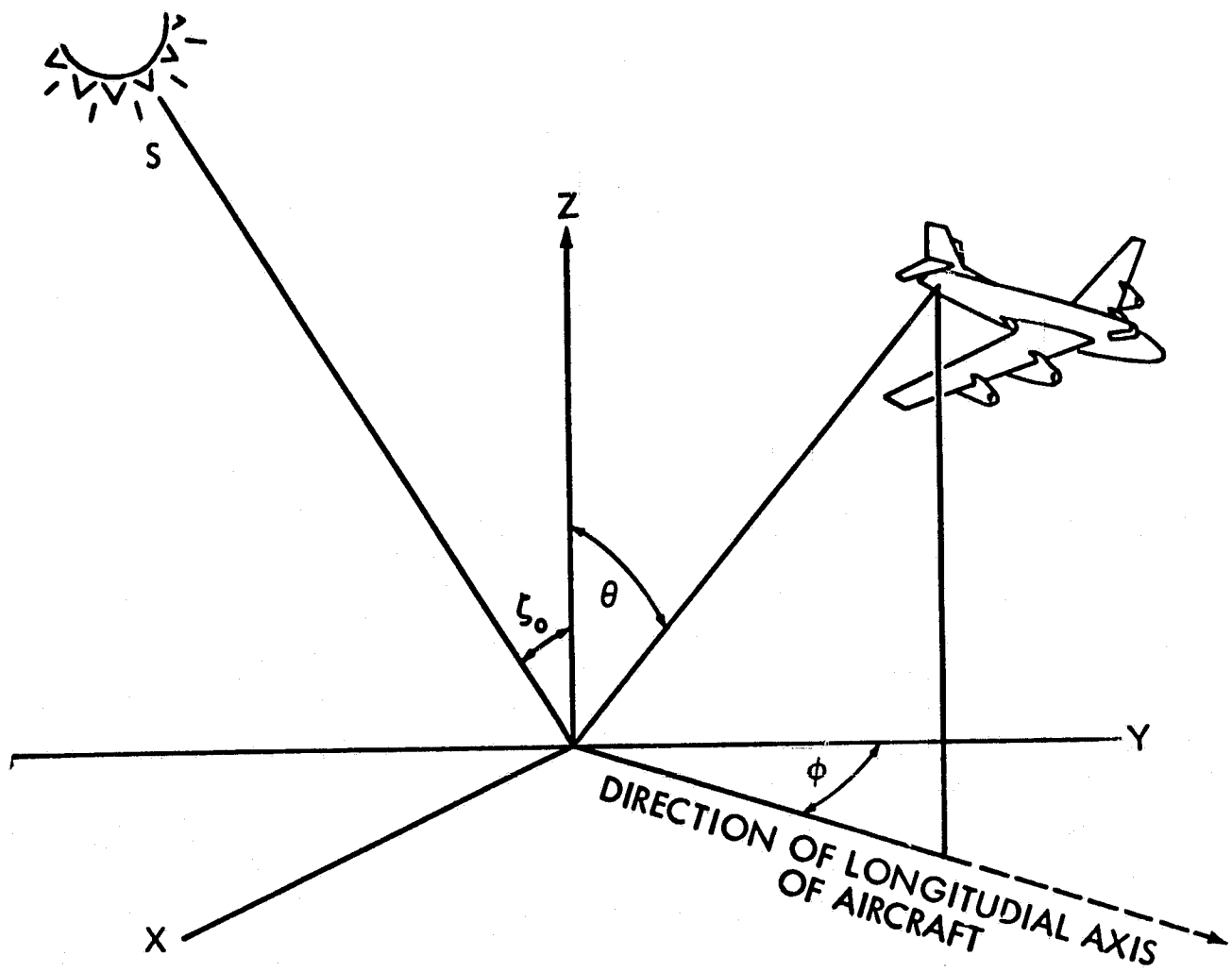

ζ_o = SOLAR ZENITH ANGLE

θ = NADIR ANGLE OF REFLECTED ENERGY

ϕ = HORIZONTAL ANGULAR DEPARTURE OF 990'S FLIGHT PATH OUT OF THE PRINCIPAL PLANE OF THE SUN

SZY = PRINCIPAL PLANE OF THE SUN.

Figure 5–Diagram showing nadir angles, azimuth and solar zenith angles. The sun's energy enters with a zenith angle of ζ_0 and is reflected with an angle of θ in the ϕ azimuthal direction.

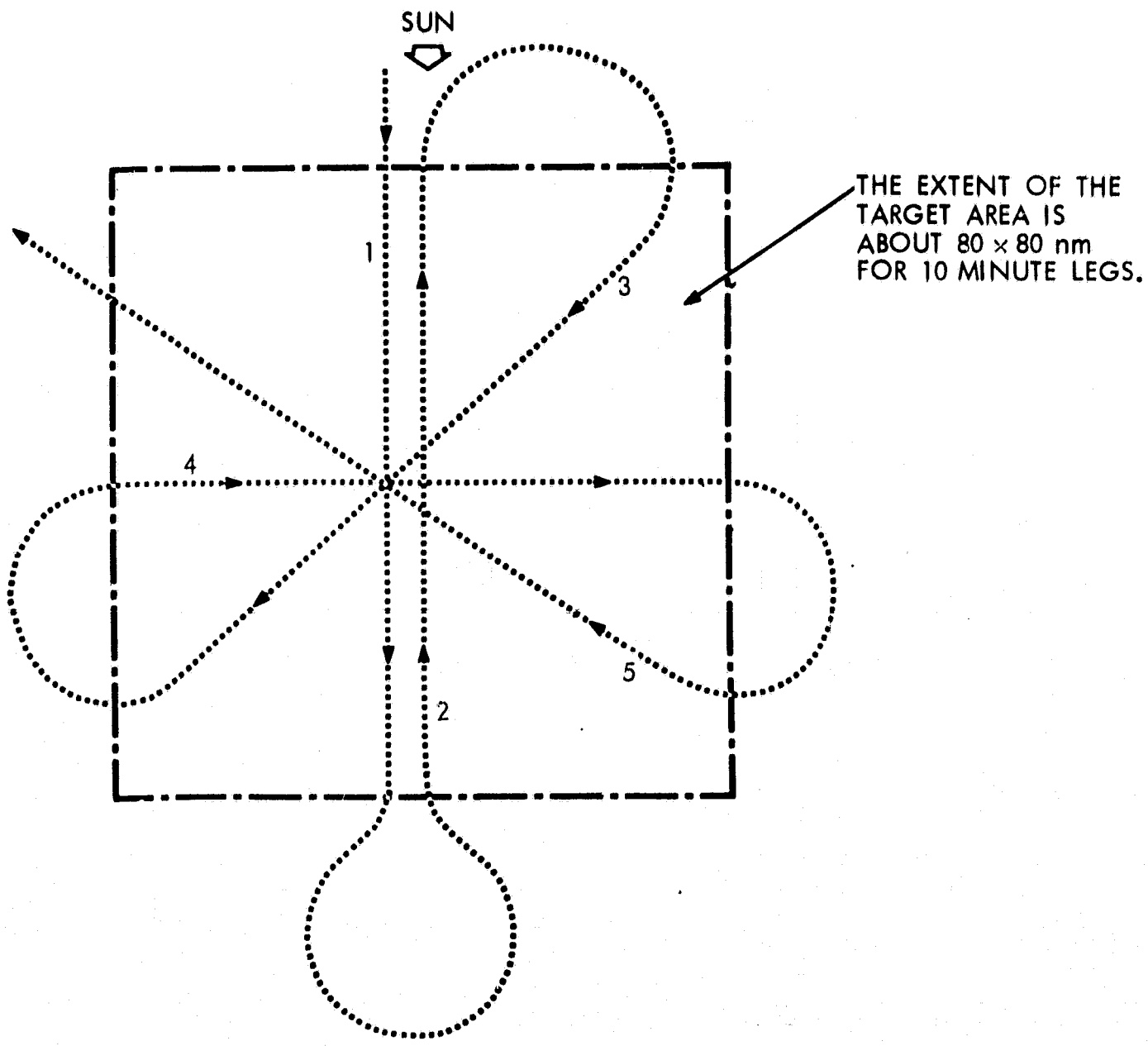

Figure 6–1966 rosette flight pattern.

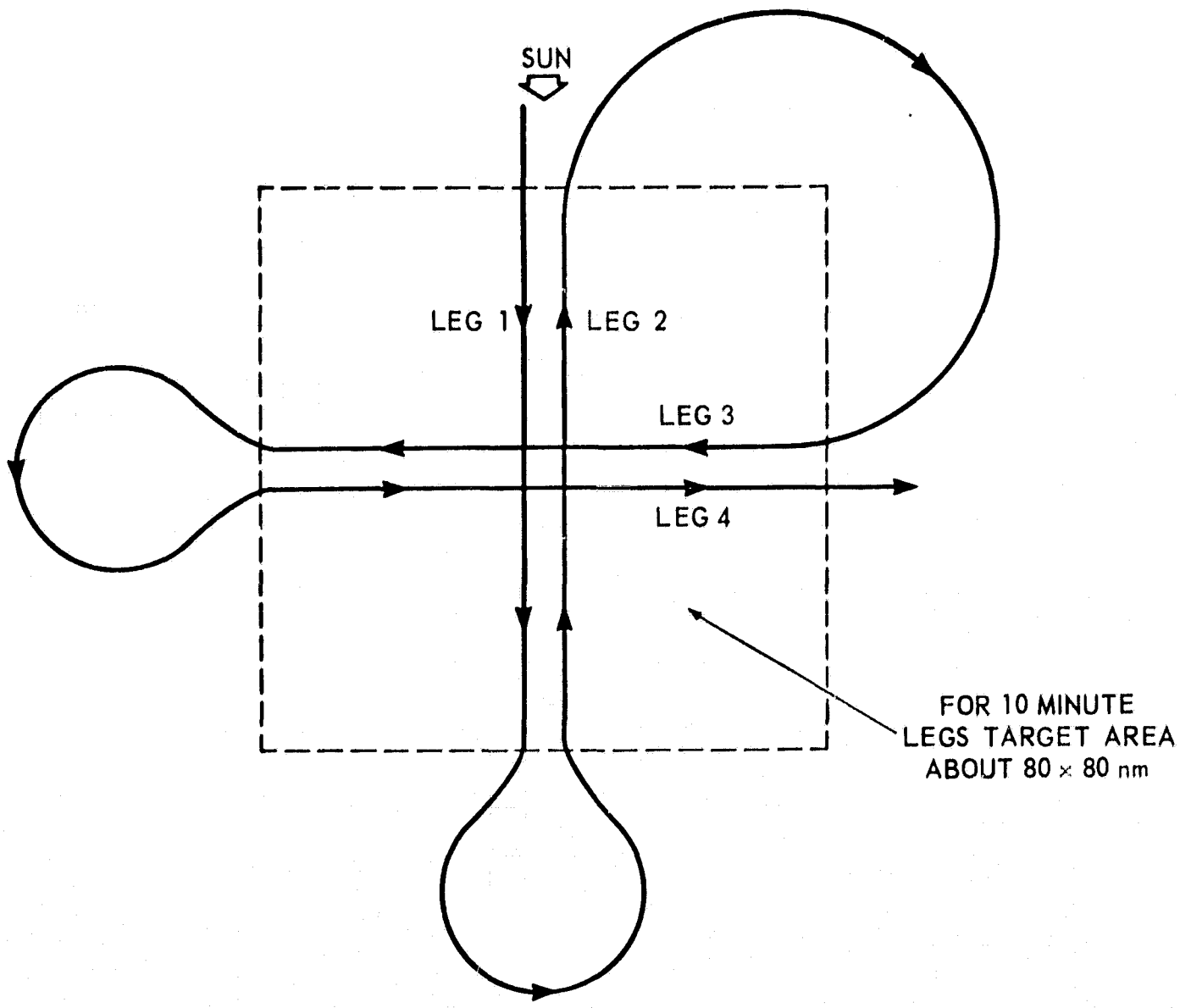

Figure 7–1967 rosette flight pattern.

TABLE I

Flt. No.	Type of Surface	Surface Alt.	Aircraft Alt. (MSL)	Range of Solar Zenith Angle (ζ_0) [degrees]		Directional Reflectance $\bar{R}(\zeta_0)$	
		10^3 ft.				%(.2–4μ)	%(.55–.85μ)
1966: 12	Desoto National Forest	0.2	37	51.6	68.6	18.0	18.6
14	Strato Cumulus Over Forest	6.3	41	54.9	72.4	51.5	61.9
34	Strato Cumulus Over Pacific Ocean	2.3	40	41.0	58.1	27.7	35.2
35	Pacific Ocean		35	44.6	50.5	7.2	9.2
36	Strato Cumulus Over Pacific Ocean		40	50.7	58.7	33.0	39.0
37	Strato Cumulus Over Pacific Ocean		25	68.4	75.7	32.0	45.6
1967: I	Strato Cumulus Over Pacific Ocean	4.5	25	61.2	69.2	48.2	57.3
I	Strato Cumulus Over Pacific Ocean	4.5	35.3	71.4	79.0	41.1	51.2
3	Strato Cumulus Over Pacific Ocean	10.0	25	22.0	24.0	34.5	41.5
II	Farmland and Wooded Areas with Patches of Stratus	0.5	33	11.6	13.3	13.7	11.4
II	Gulf of Mexico		28	29.5	35.5	6.1	8.0

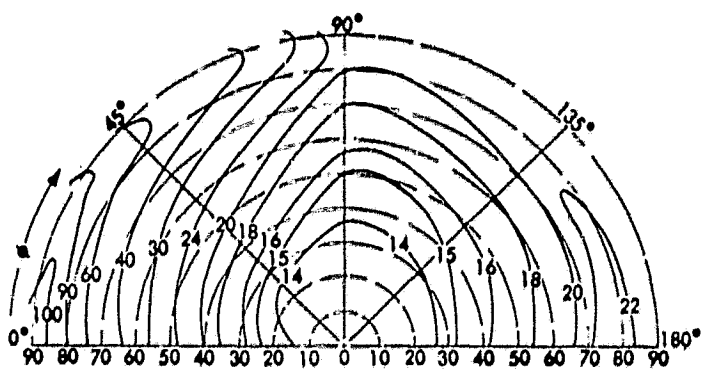

NADIR ANGLE (degrees)

0.55-0.85μ

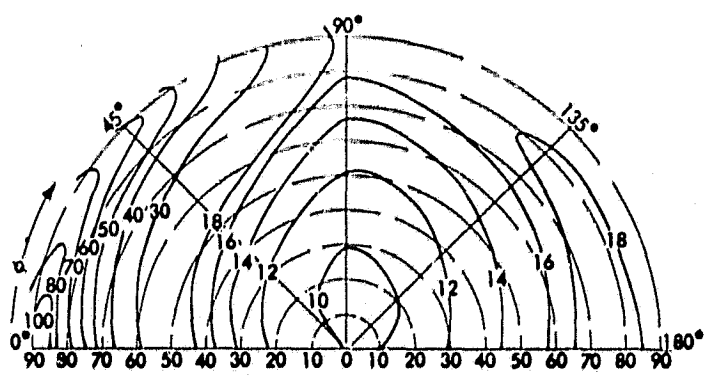

NADIR ANGLE (degrees)

0.2-4.0μ

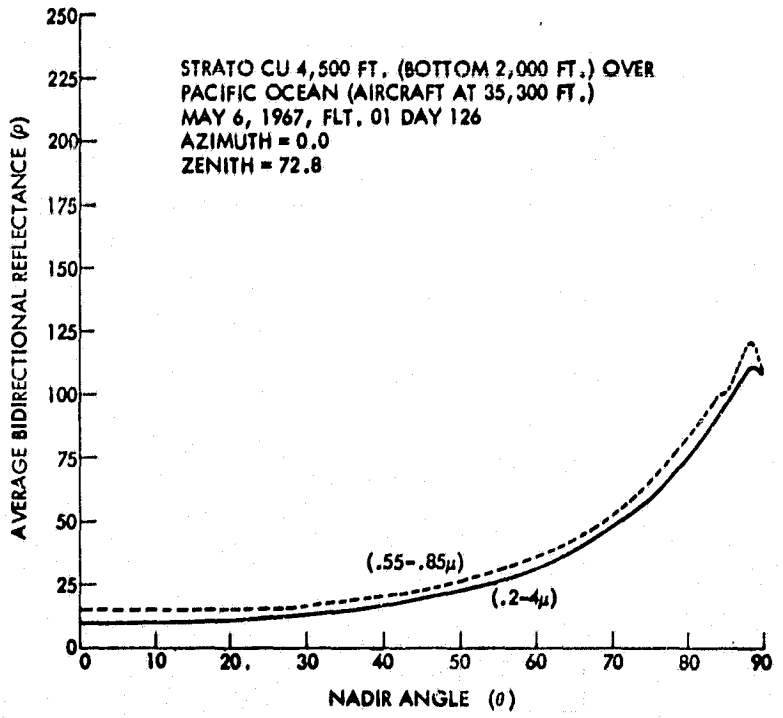

Figure 8–Bidirectional reflectances of strato cumulus tops at 4,500 ft., bases at 2,000 ft.

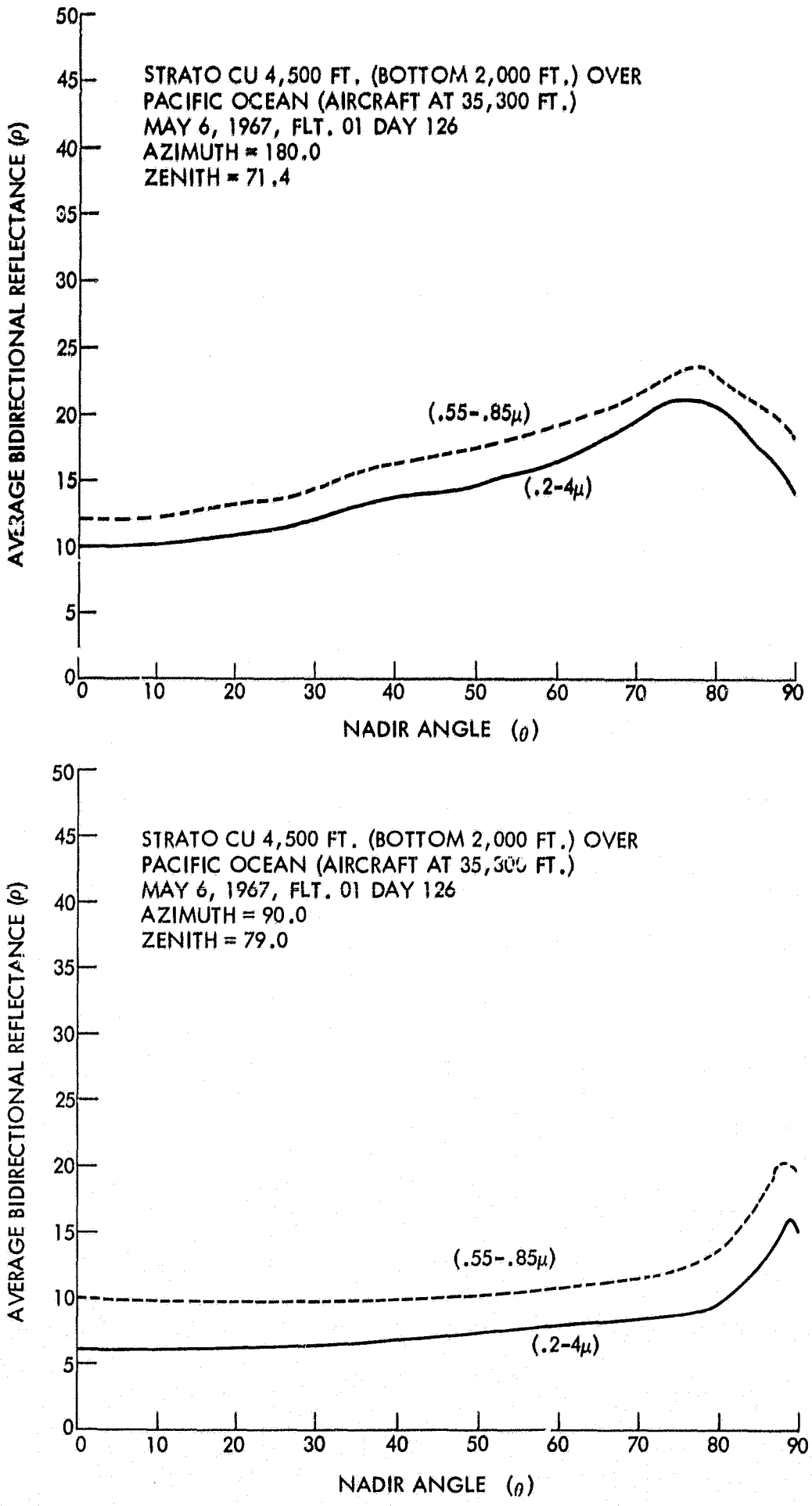

Figure 9–Bidirectional reflectances of strato cumulus tops at 4,500 ft., bases at 2,000 ft.

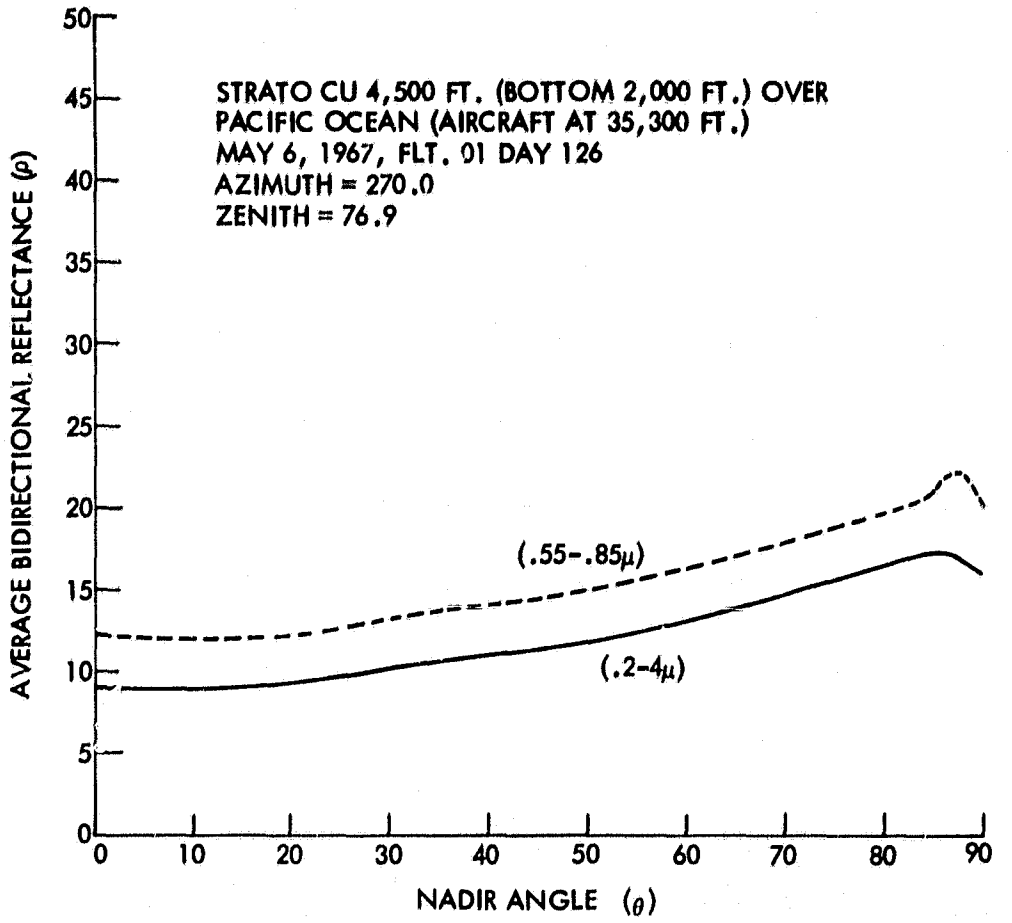

Figure 10–Bidirectional reflectances of strato cumulus tops at 4,500 ft. bases at 2,000 ft.

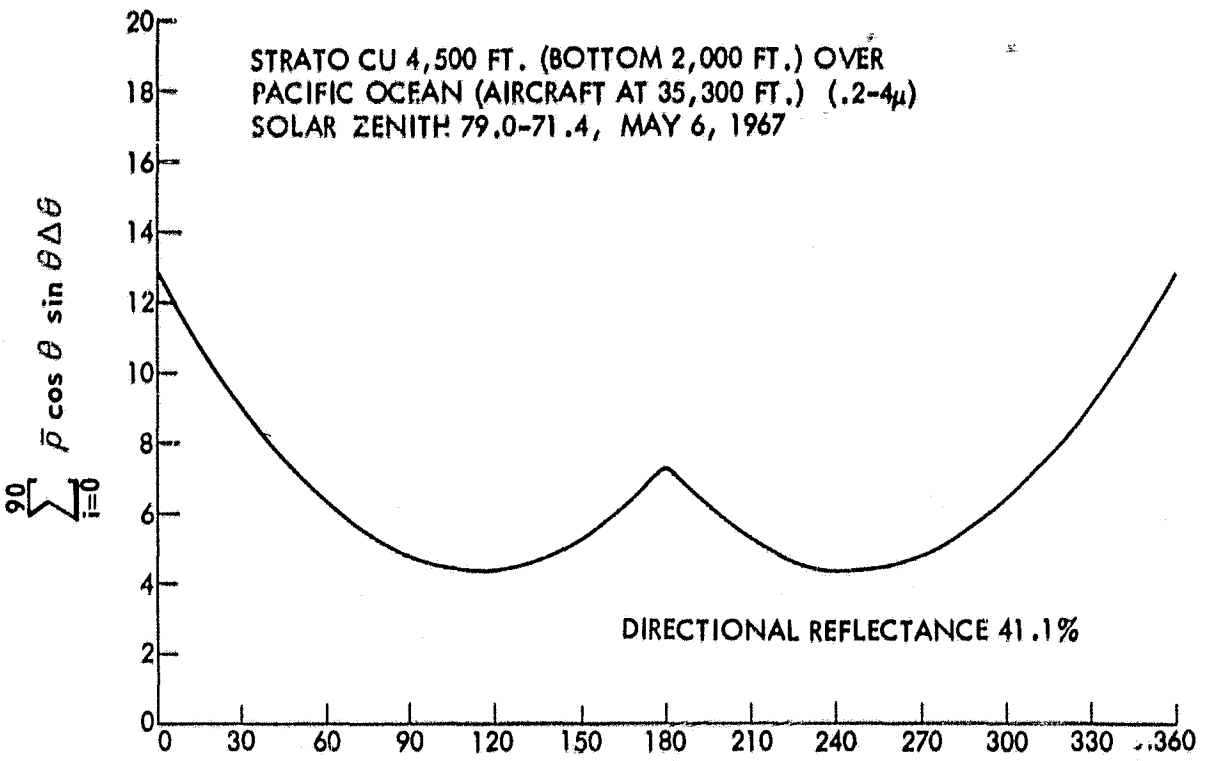

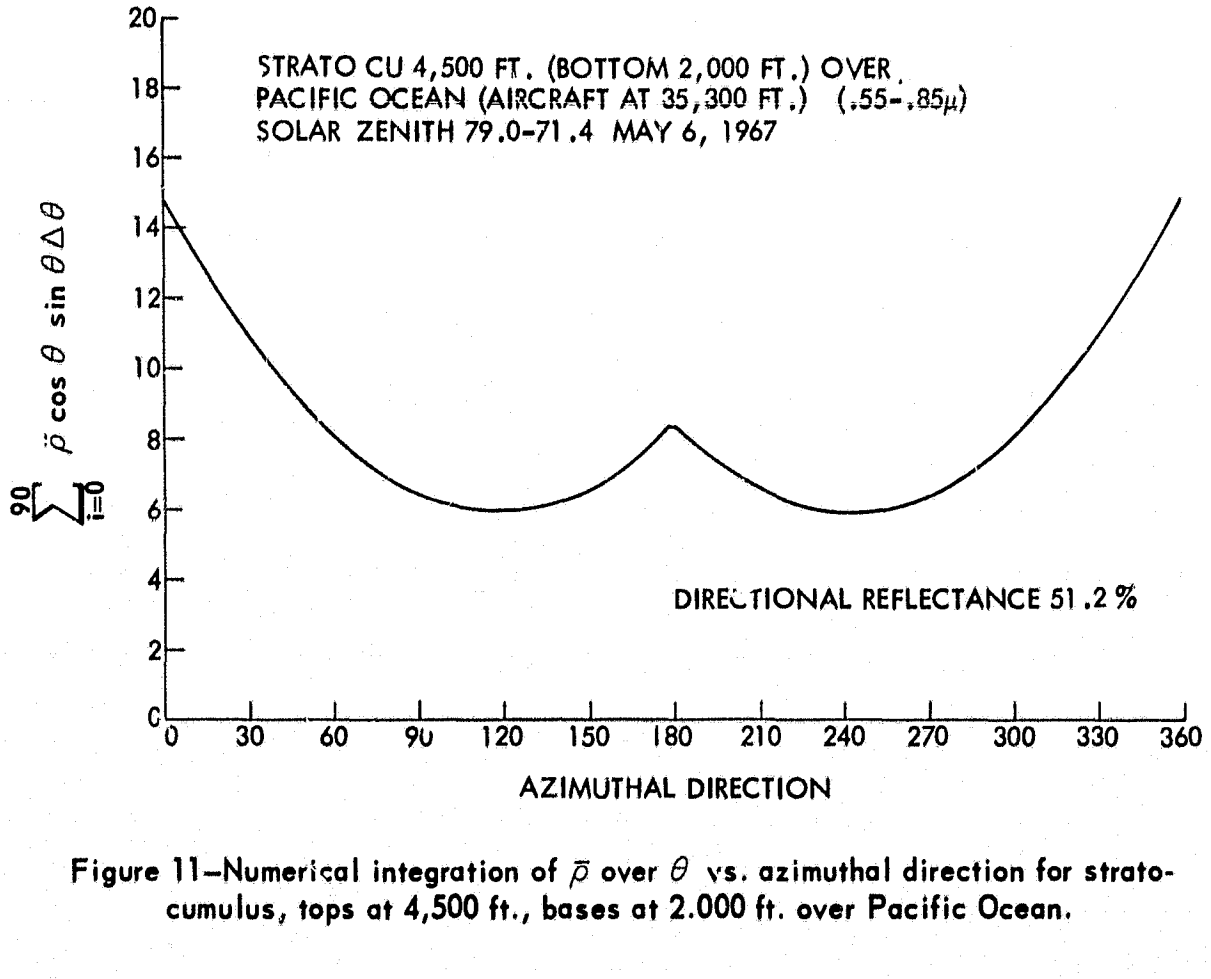

Figure 11–Numerical integration of $\bar{\rho}$ over θ vs. azimuthal direction for stratocumulus, tops at 4,500 ft., bases at 2.000 ft. over Pacific Ocean.

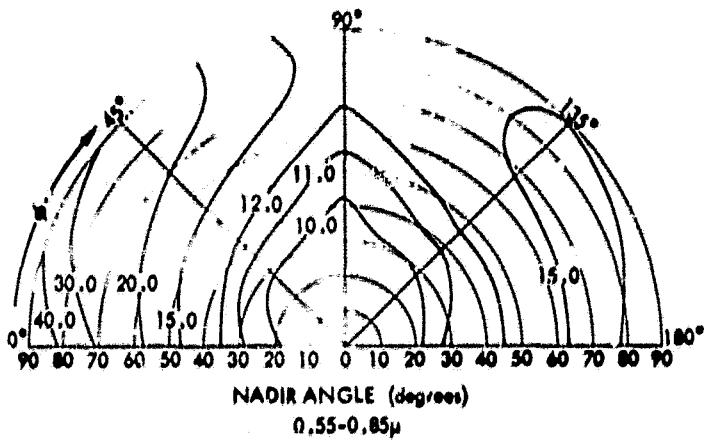

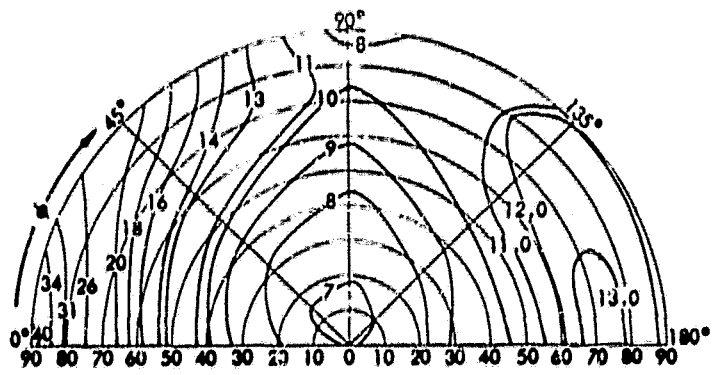

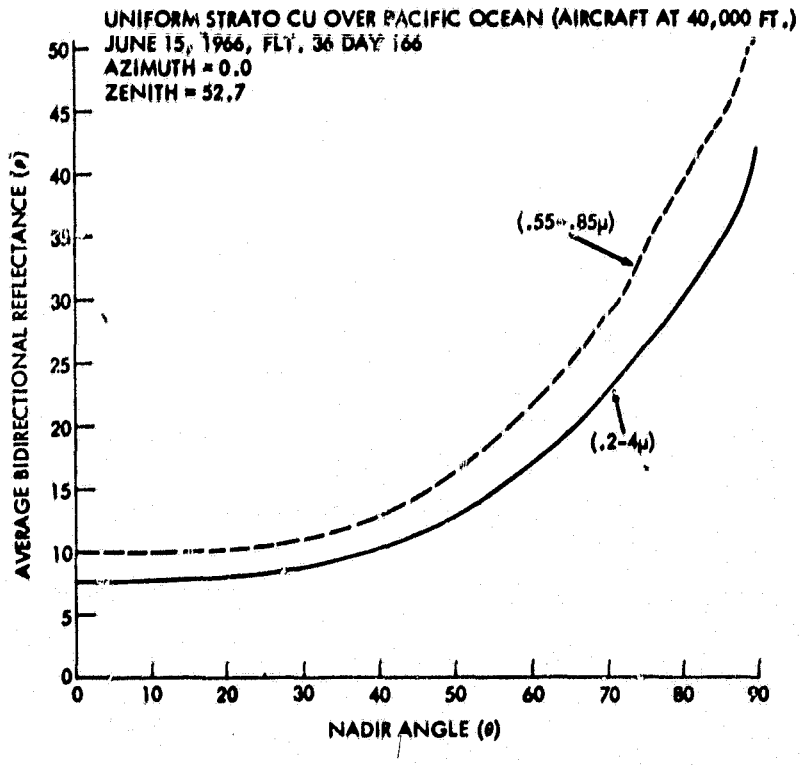

Figure 12–Bidirectional reflectances of uniform strato cumulus over Pacific Ocean.

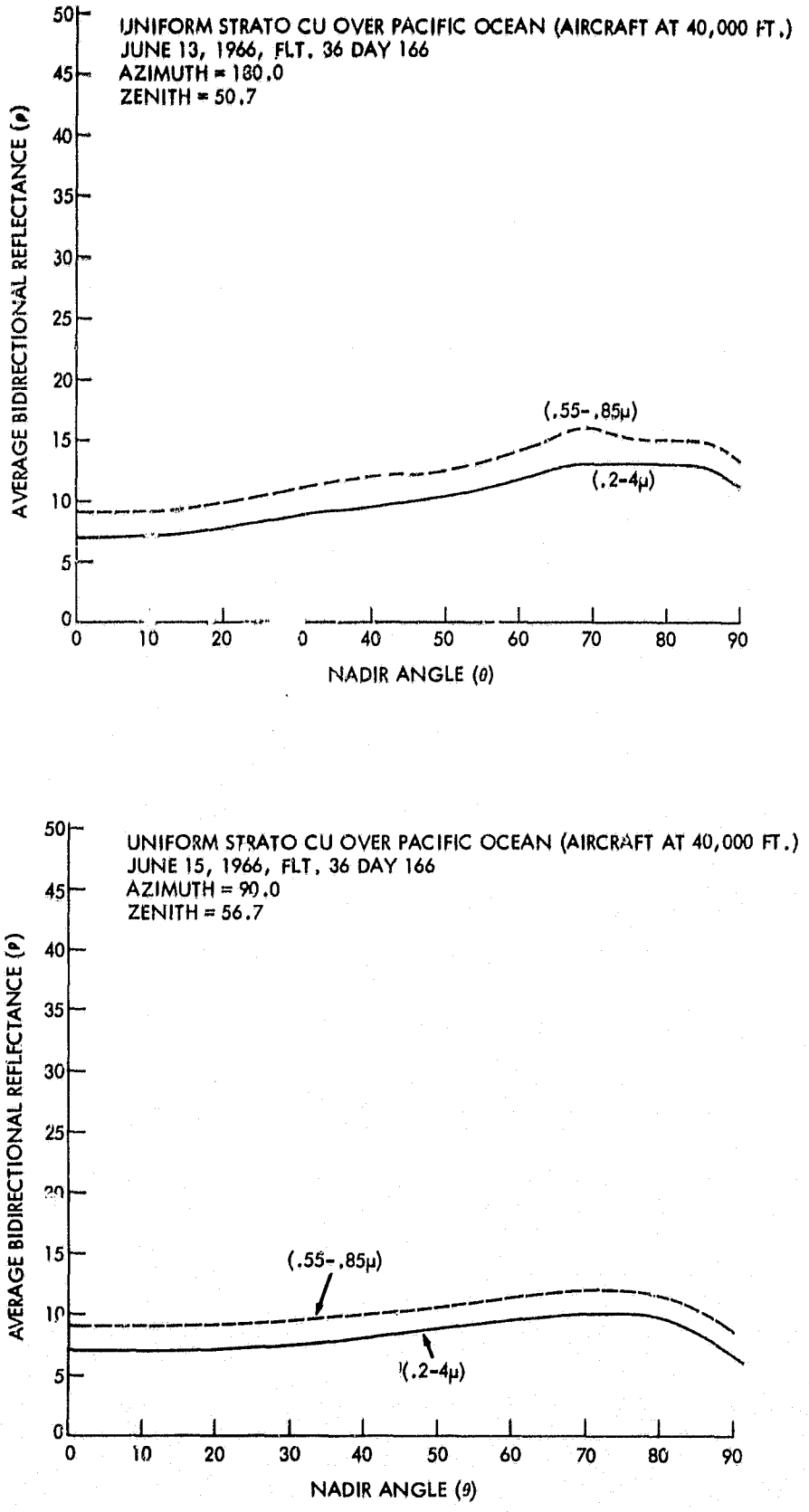

Figure 13–Bidirectional reflectances of uniform strato cumulus over Pacific Ocean.

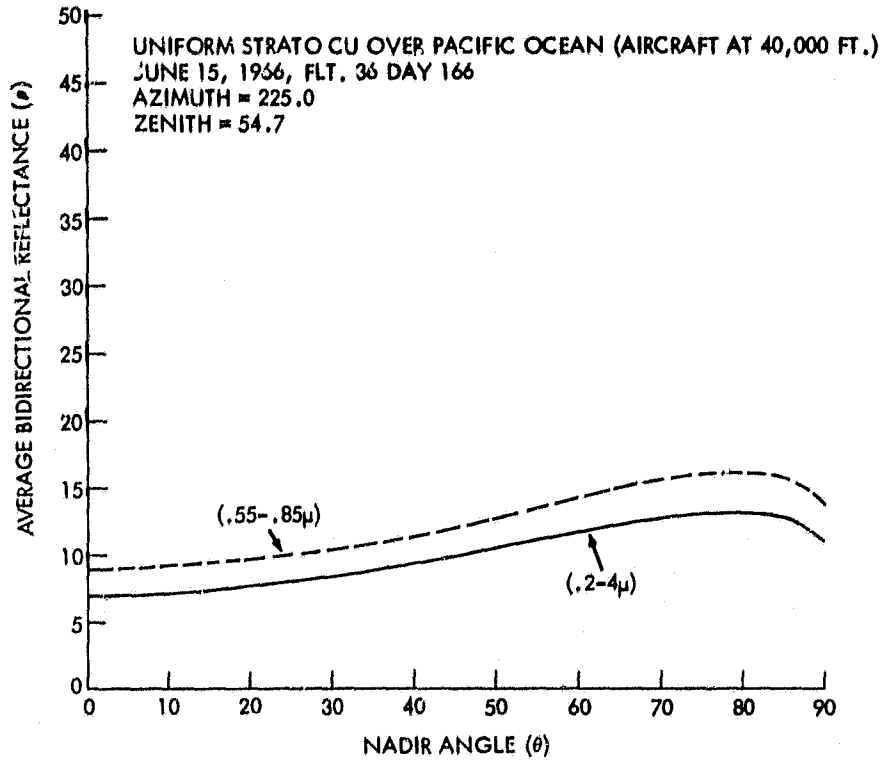

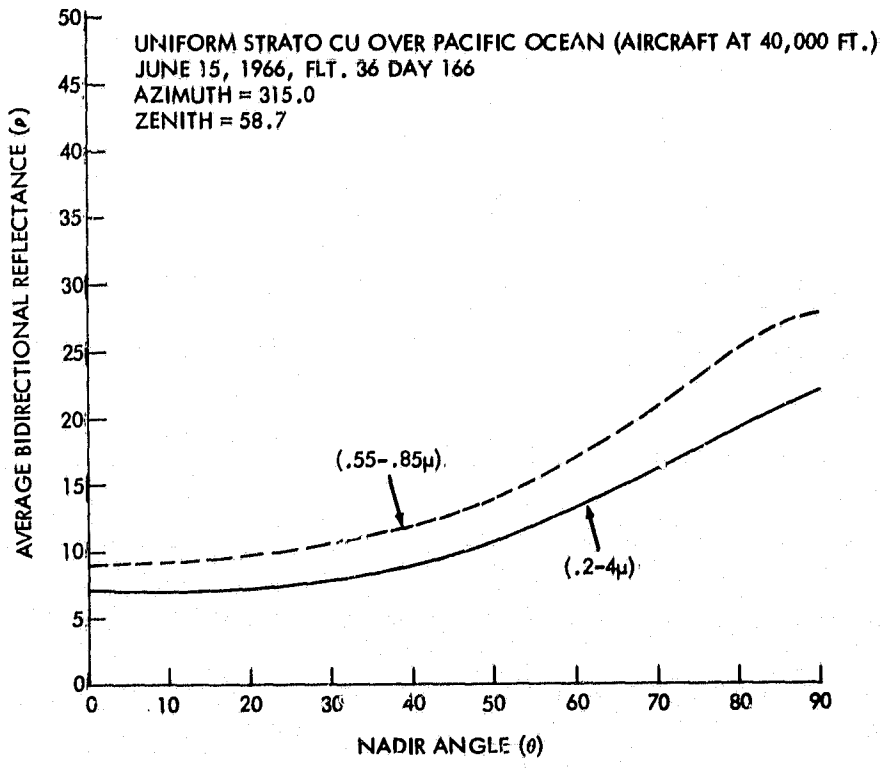

Figure 14–Bidirectional reflectances of uniform strato cumulus over Pacific Ocean.

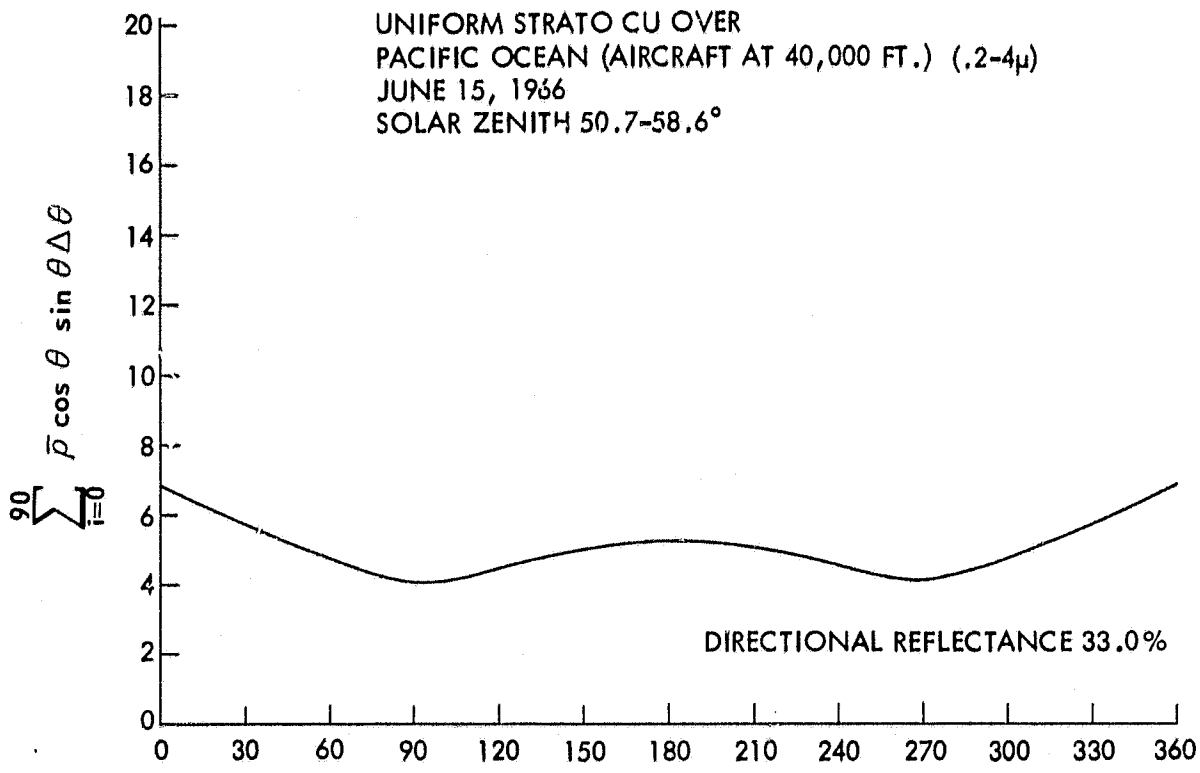

Figure 15–Numerical integration of $\bar{\rho}$ over θ vs. azimuthal direction for uniform strato cumulus over Pacific Ocean.

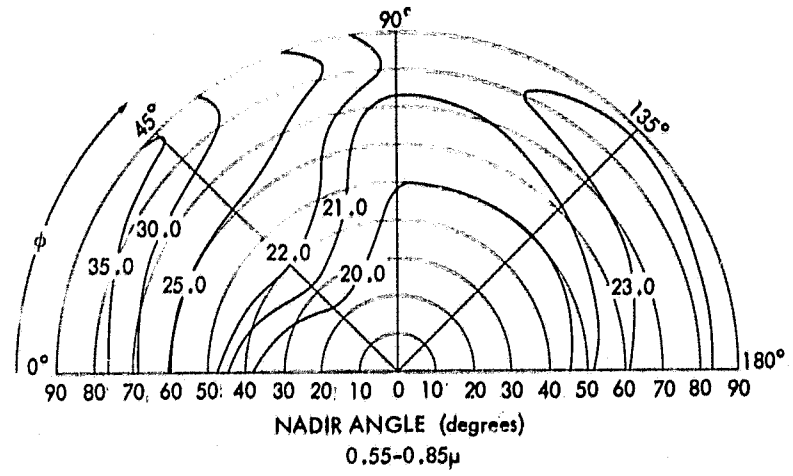

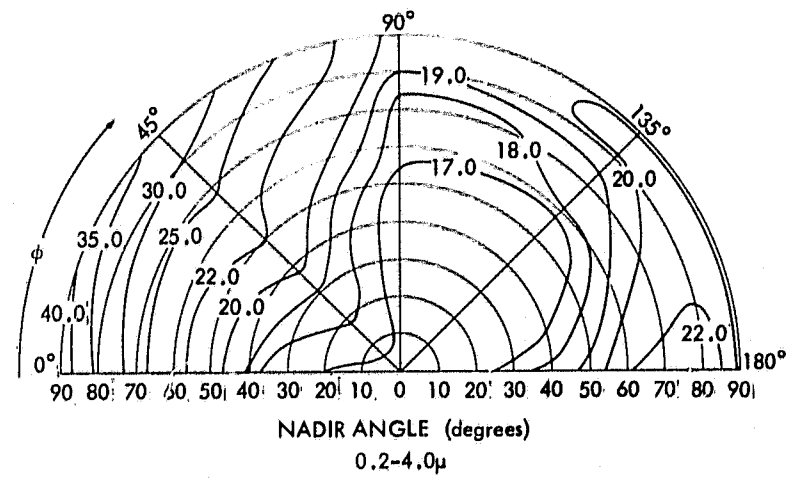

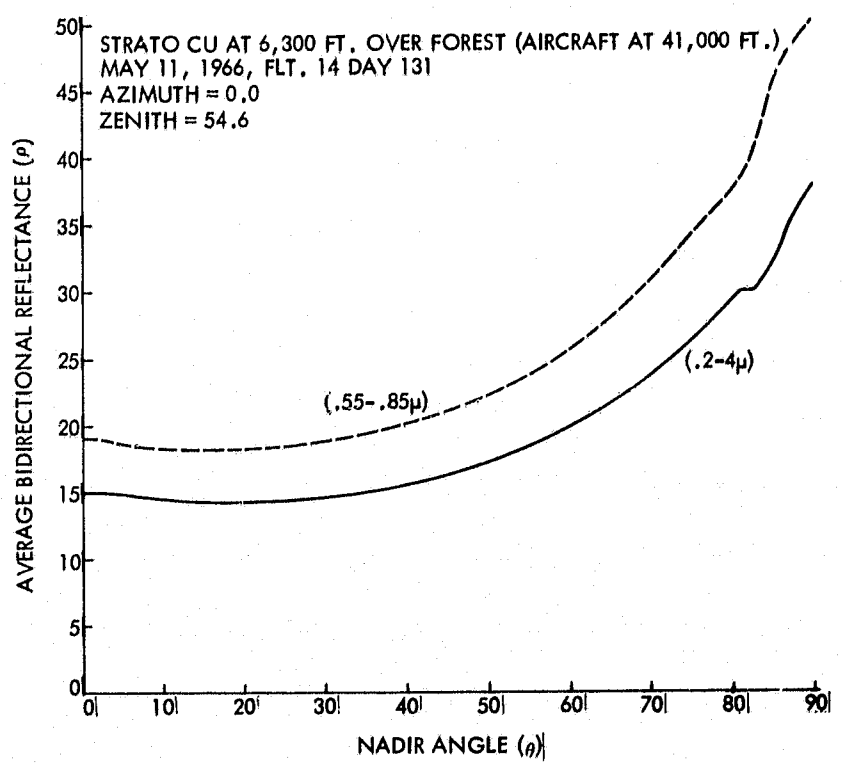

Figure 16–Bidirectional reflectances of strato cumulus over forest.

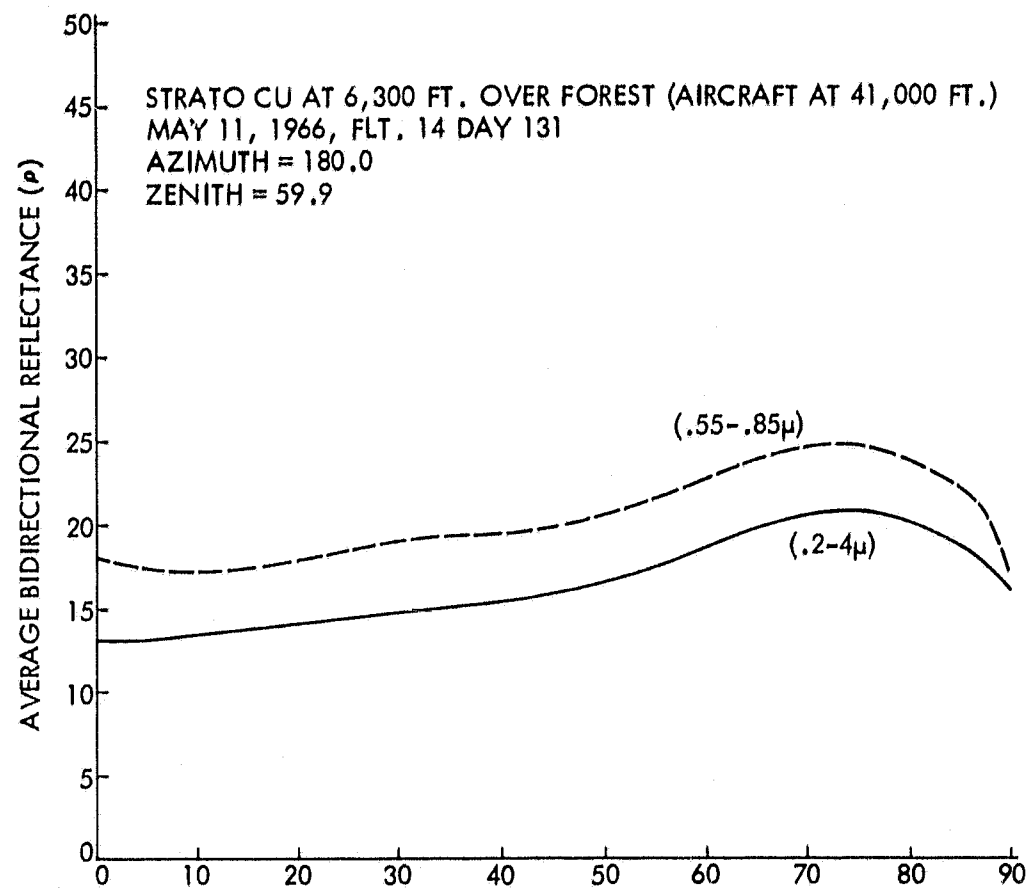

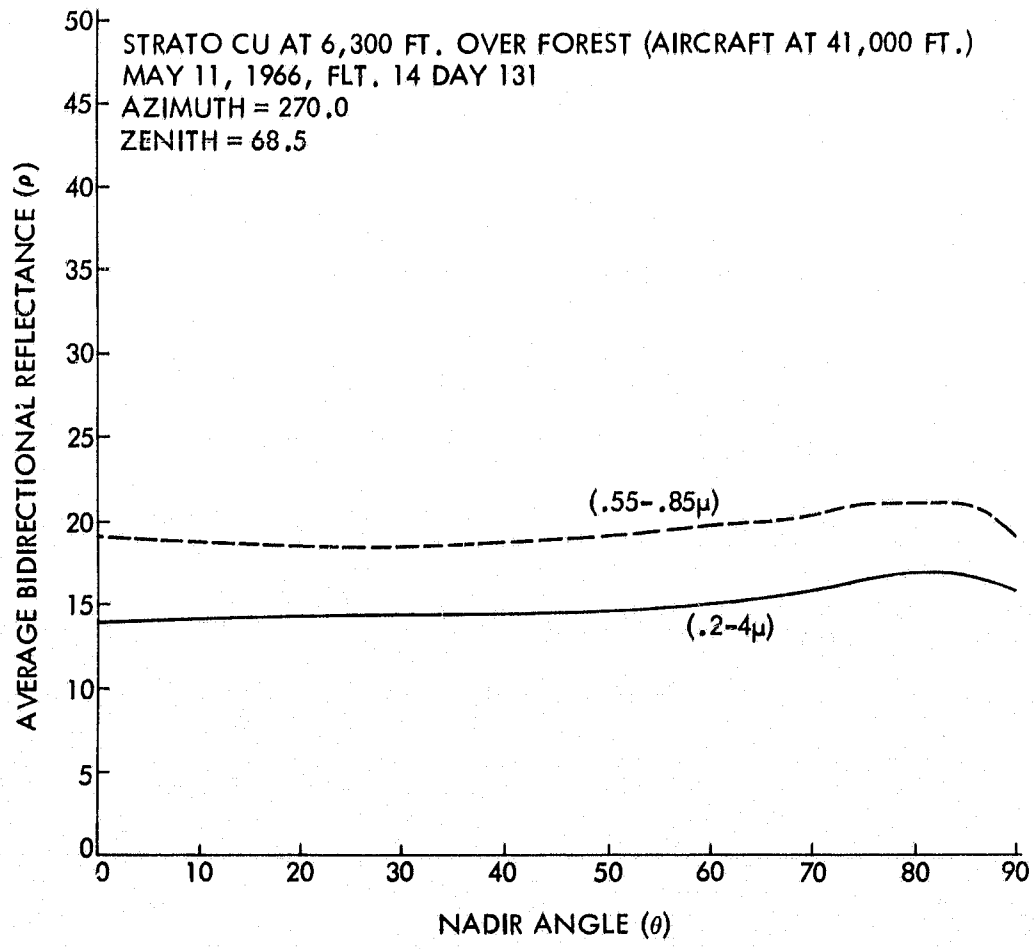

Figure 17–Bidirectional reflectances of strato cumulus over forest.

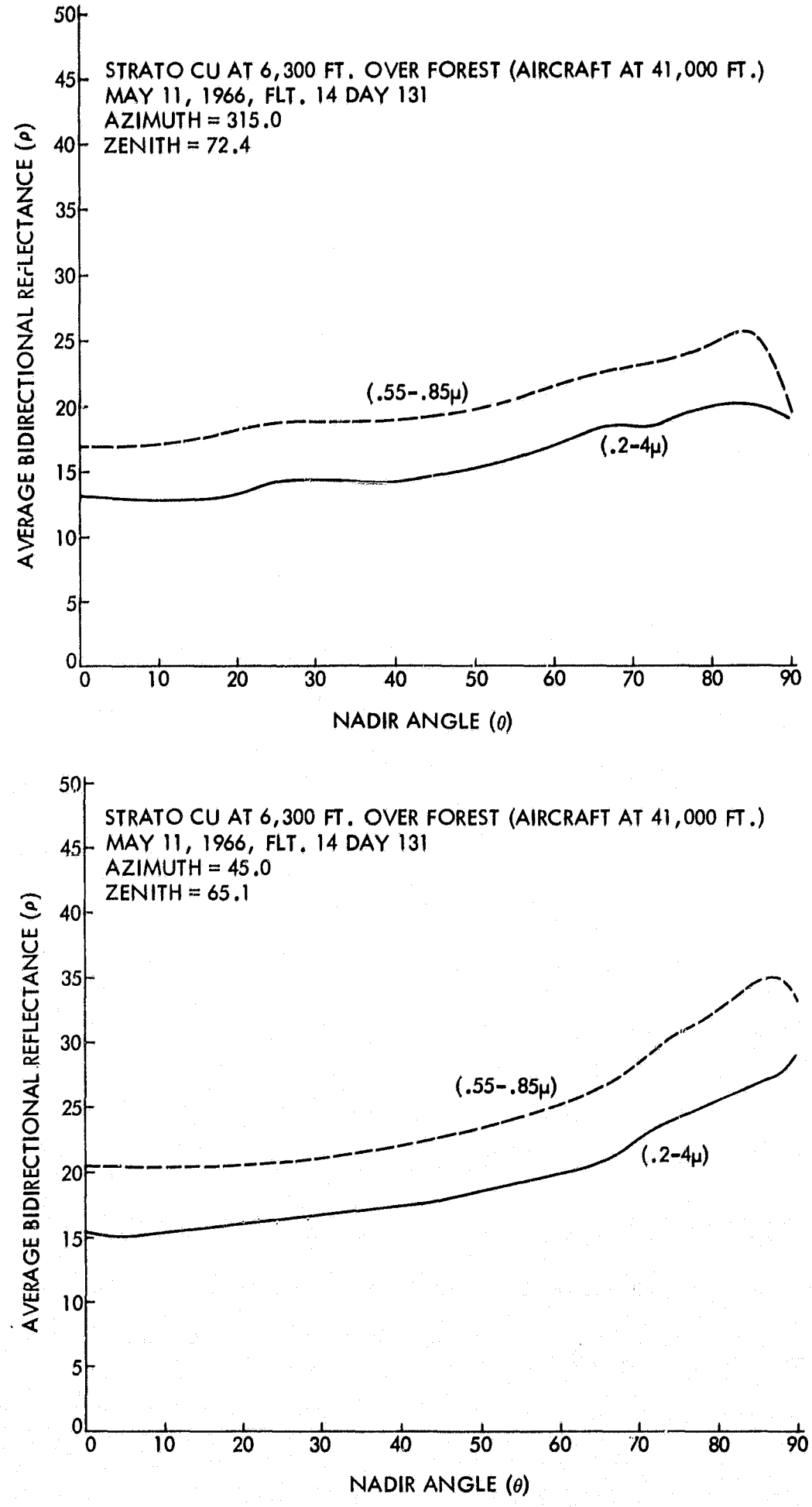

Figure 18–Bidirectional reflectances of strato cumulus over forest.

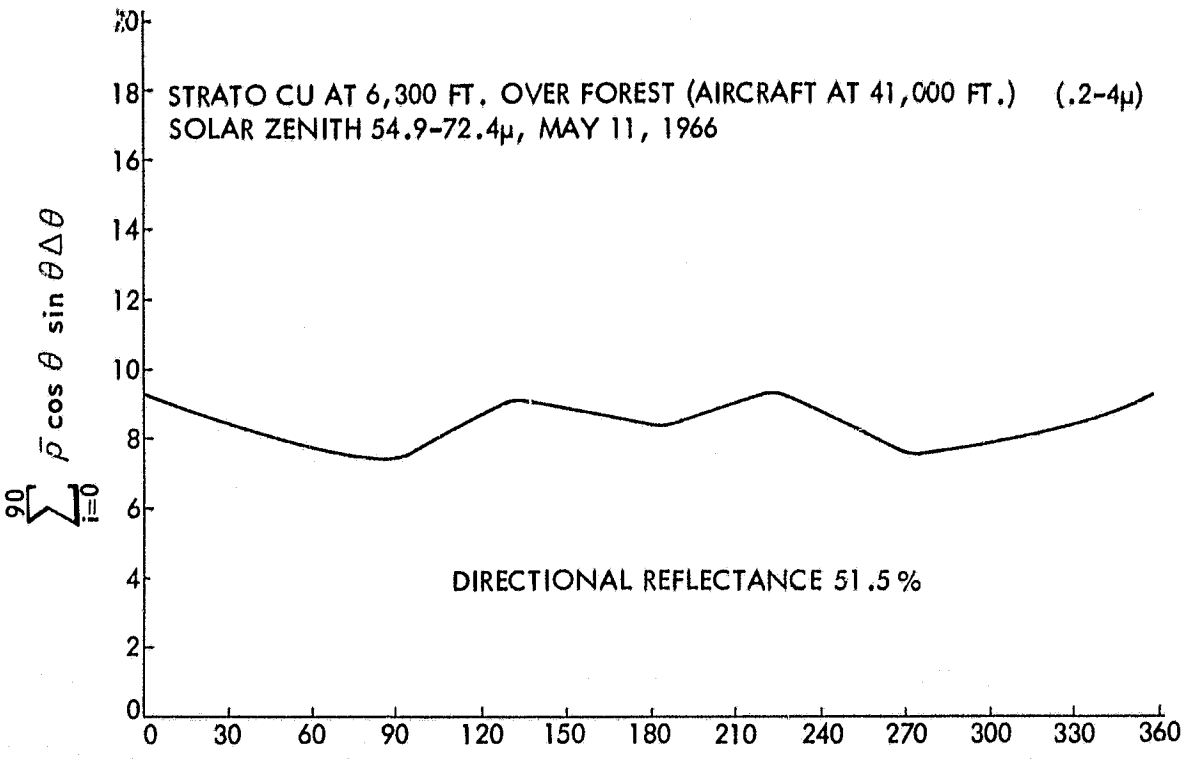

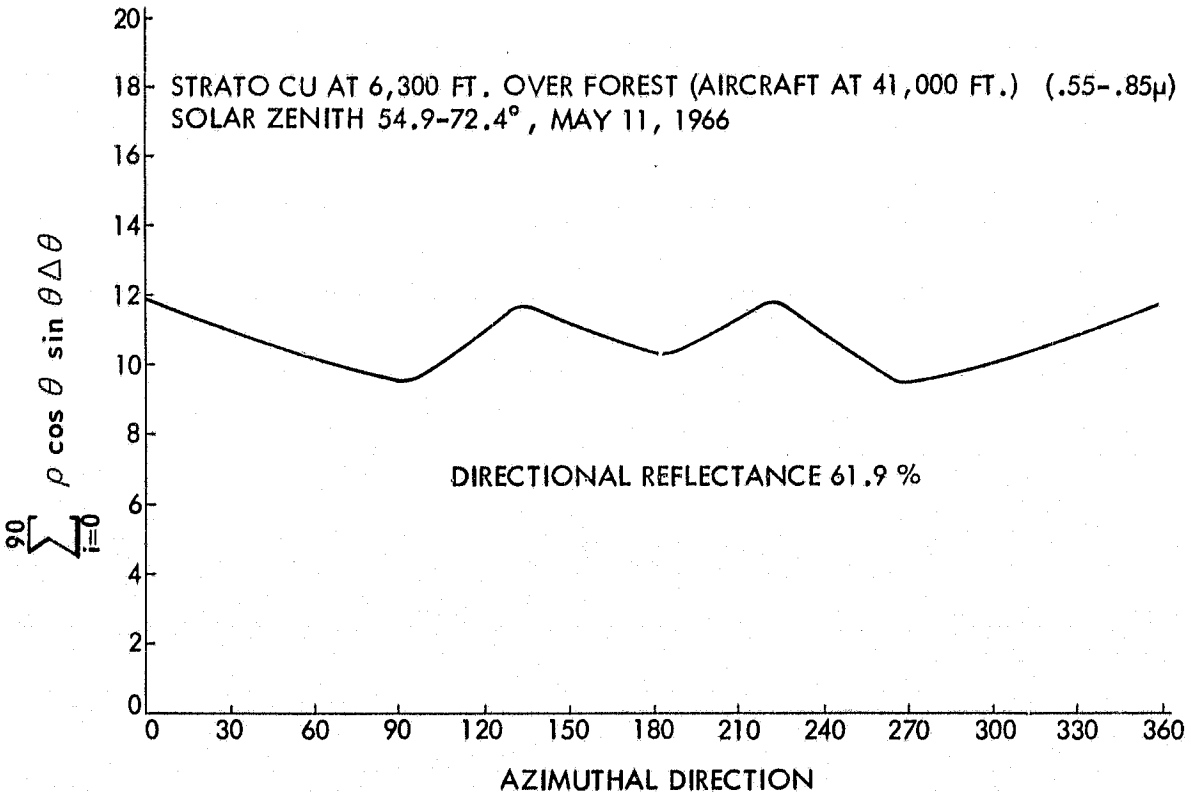

Figure 19–Numerical integration of $\bar{\rho}$ over θ vs. azimuthal direction for strato cumulus over forest plotted.

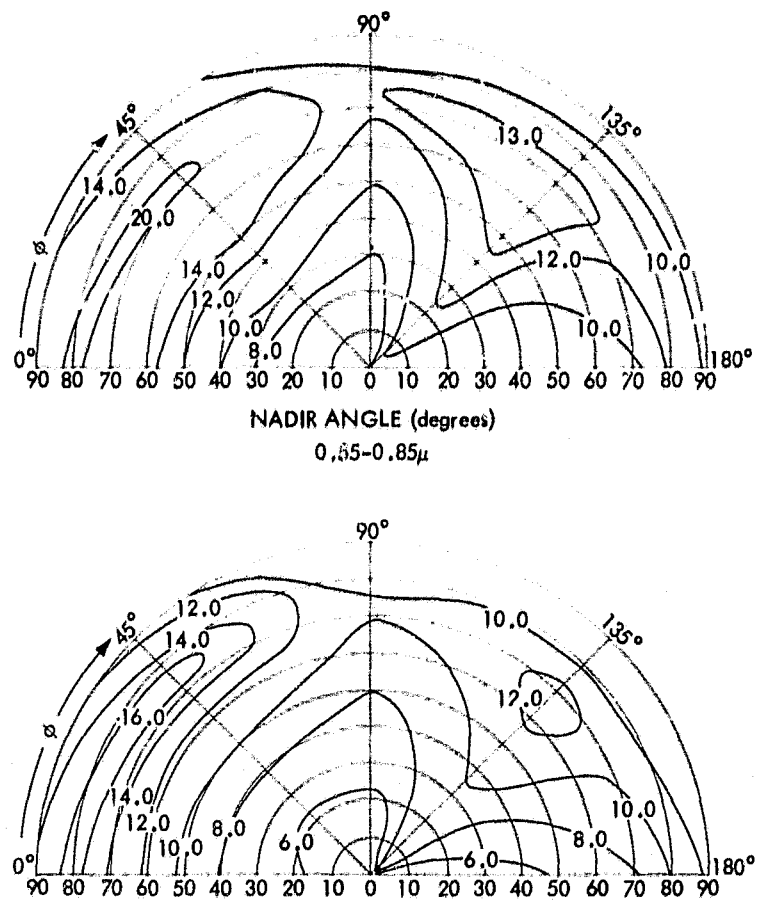

NADIR ANGLE (degrees)

0.55-0.85μ

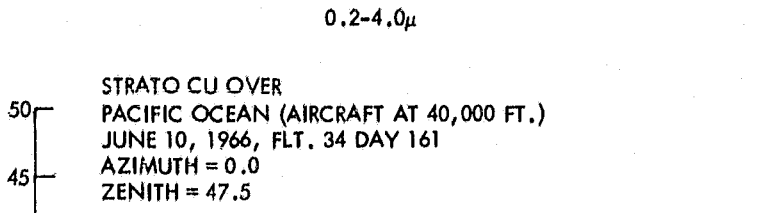

NADIR ANGLE (degrees)

0.2-4.0μ

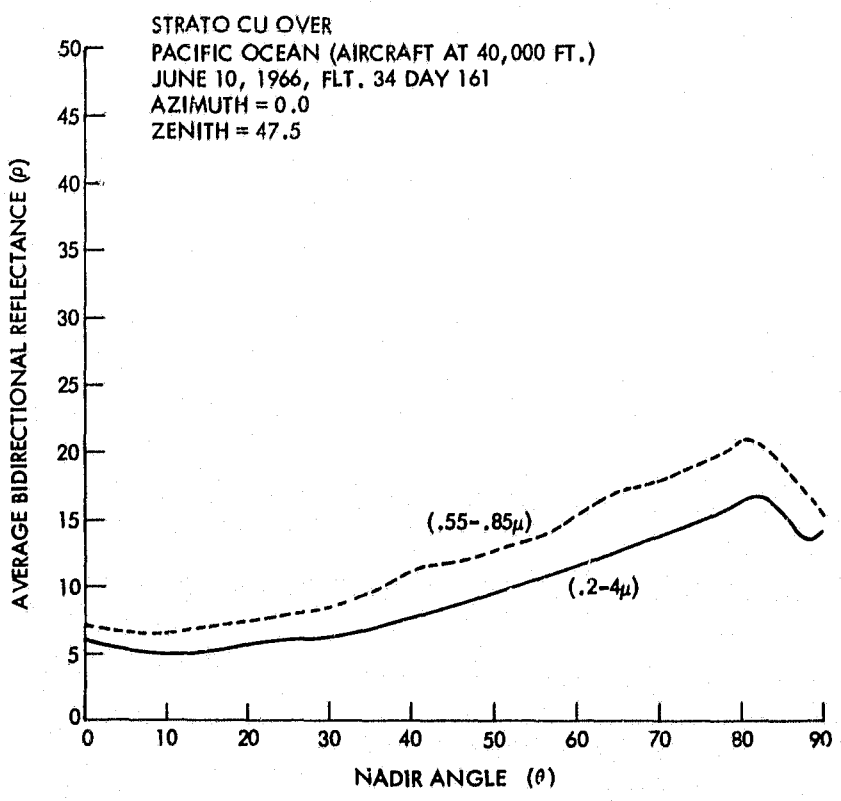

Figure 20–Bidirectional reflectances of strato cumulus at 2,300 ft. over Pacific Ocean.

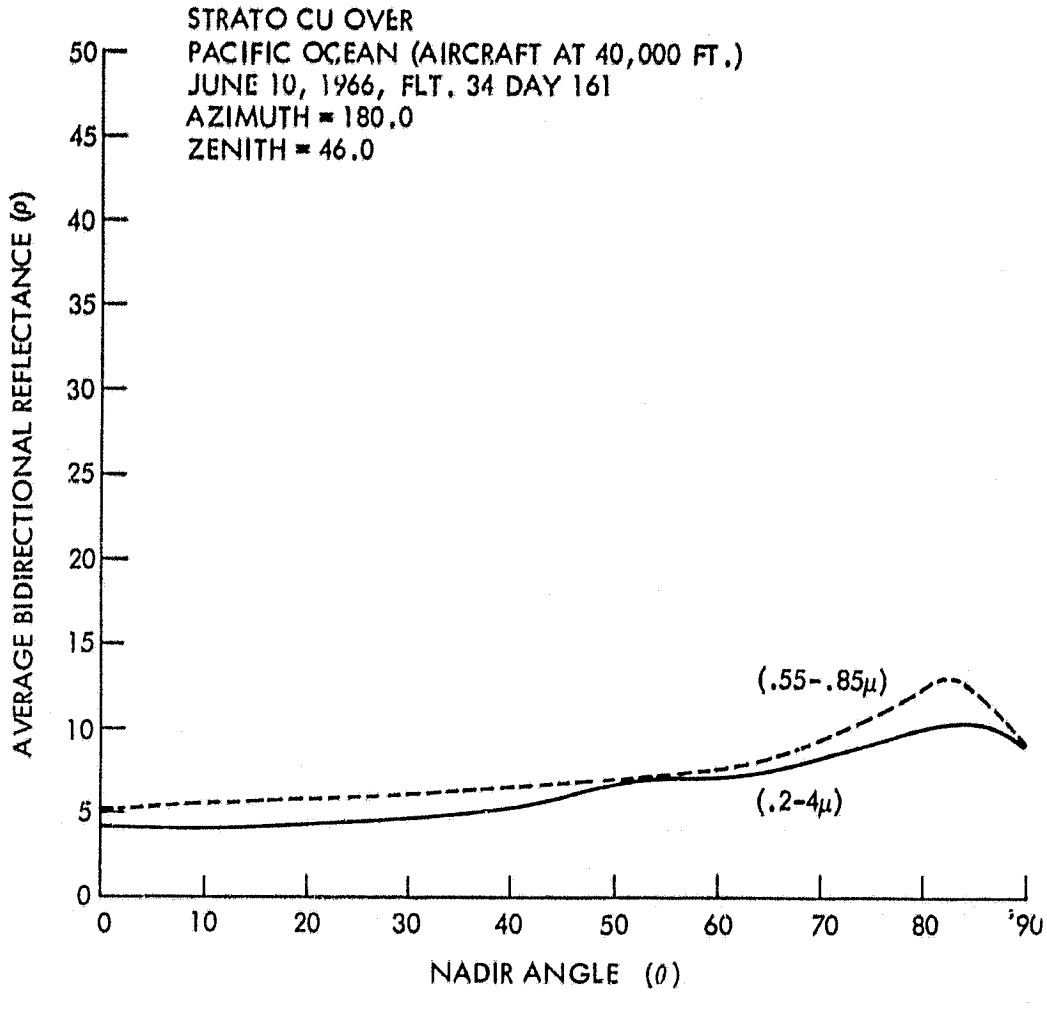

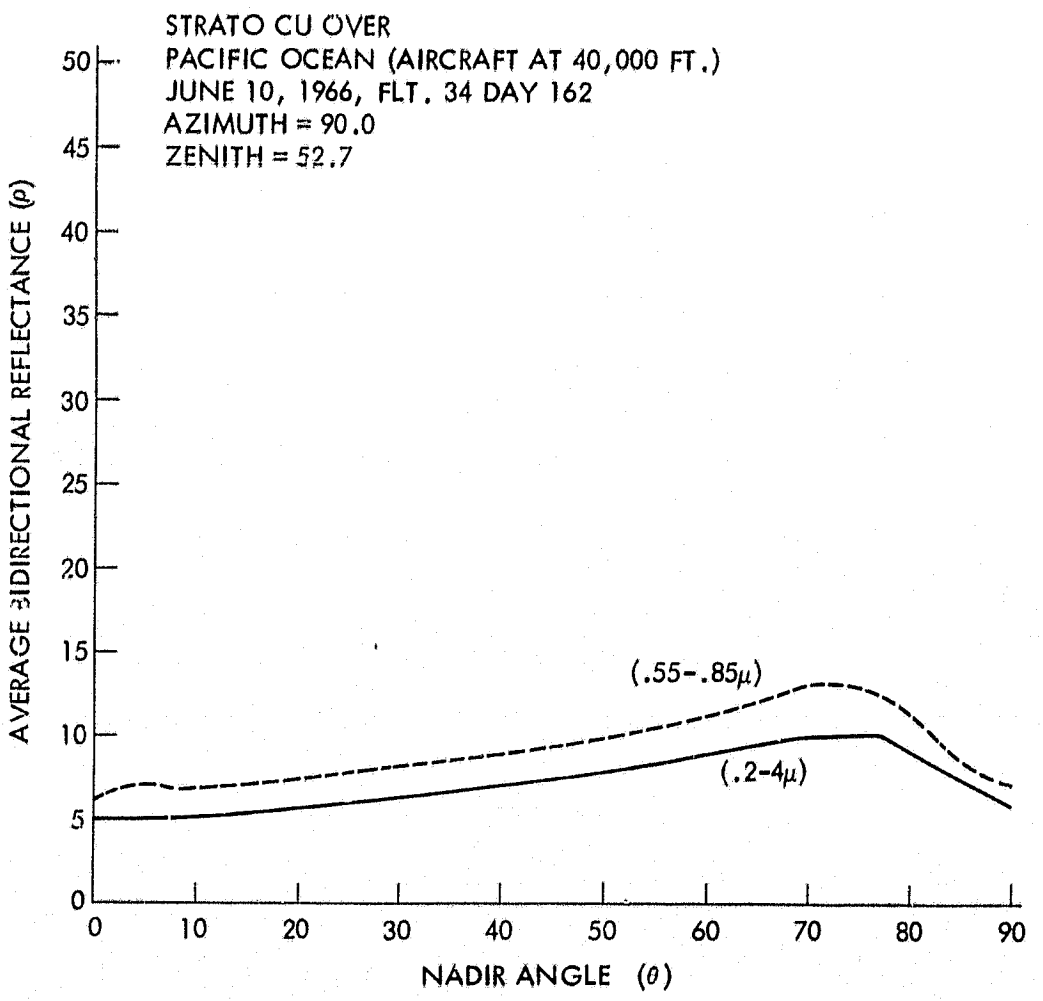

Figure 21–Bidirectional reflectances of strato cumulus at 2,300 ft. over Pacific Ocean.

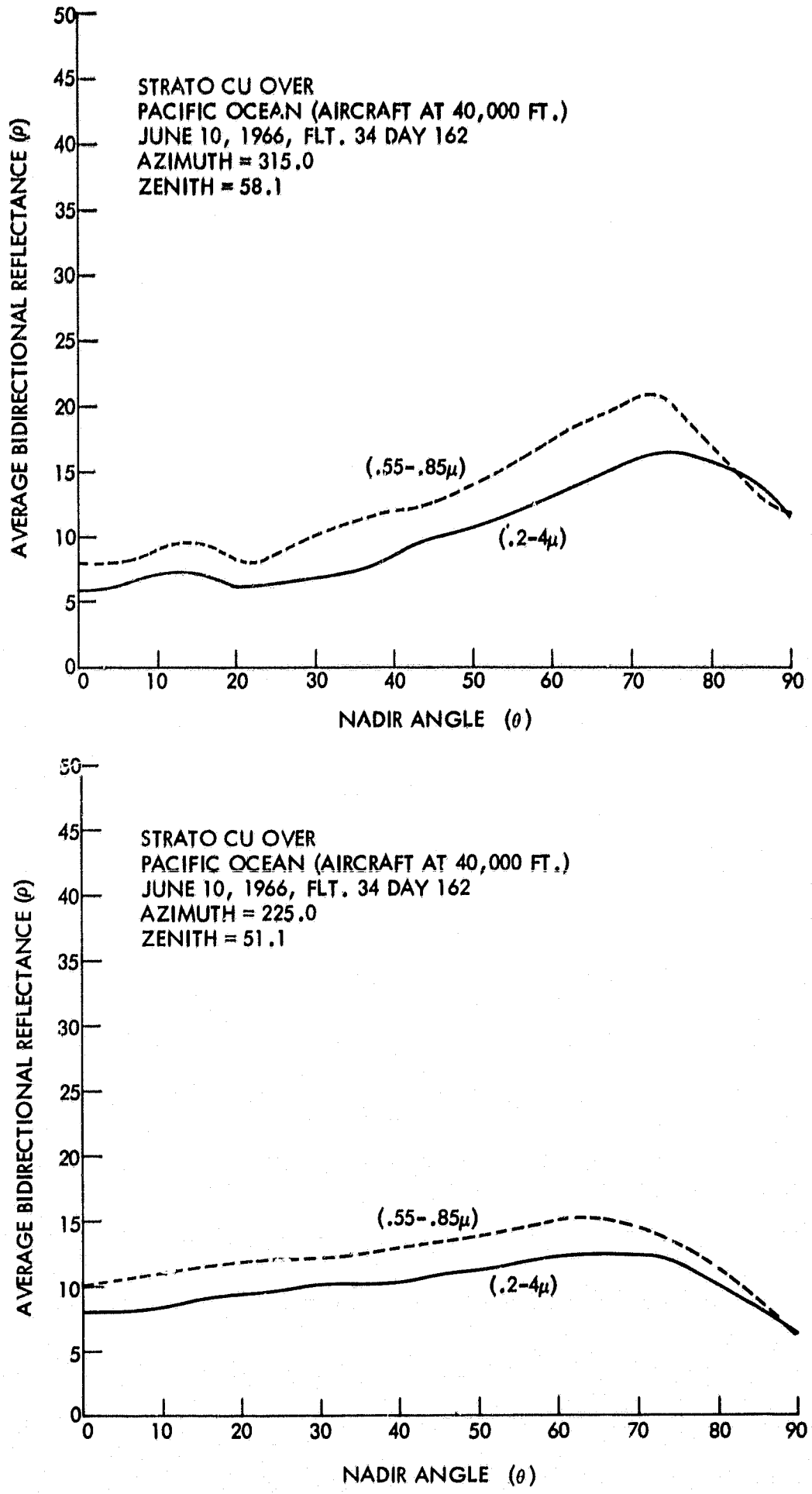

Figure 22–Bidirectional reflectances of strato cumulus at 2,300 ft. over Pacific Ocean.

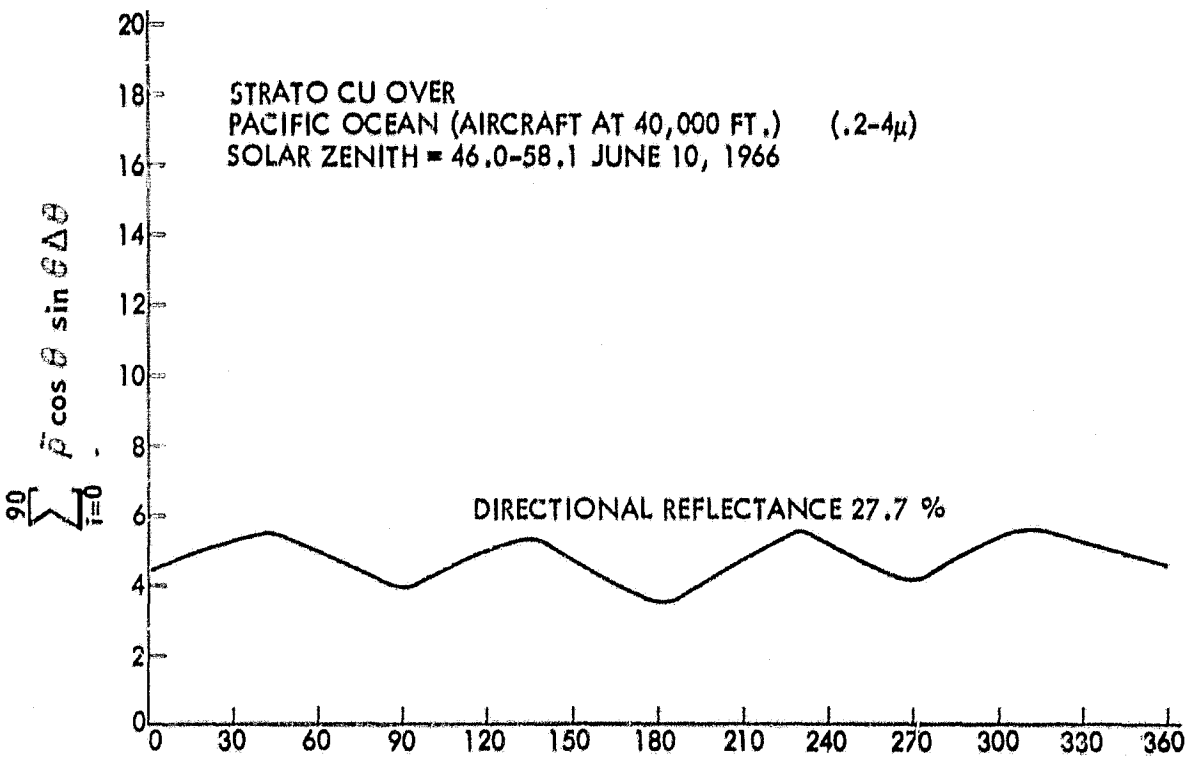

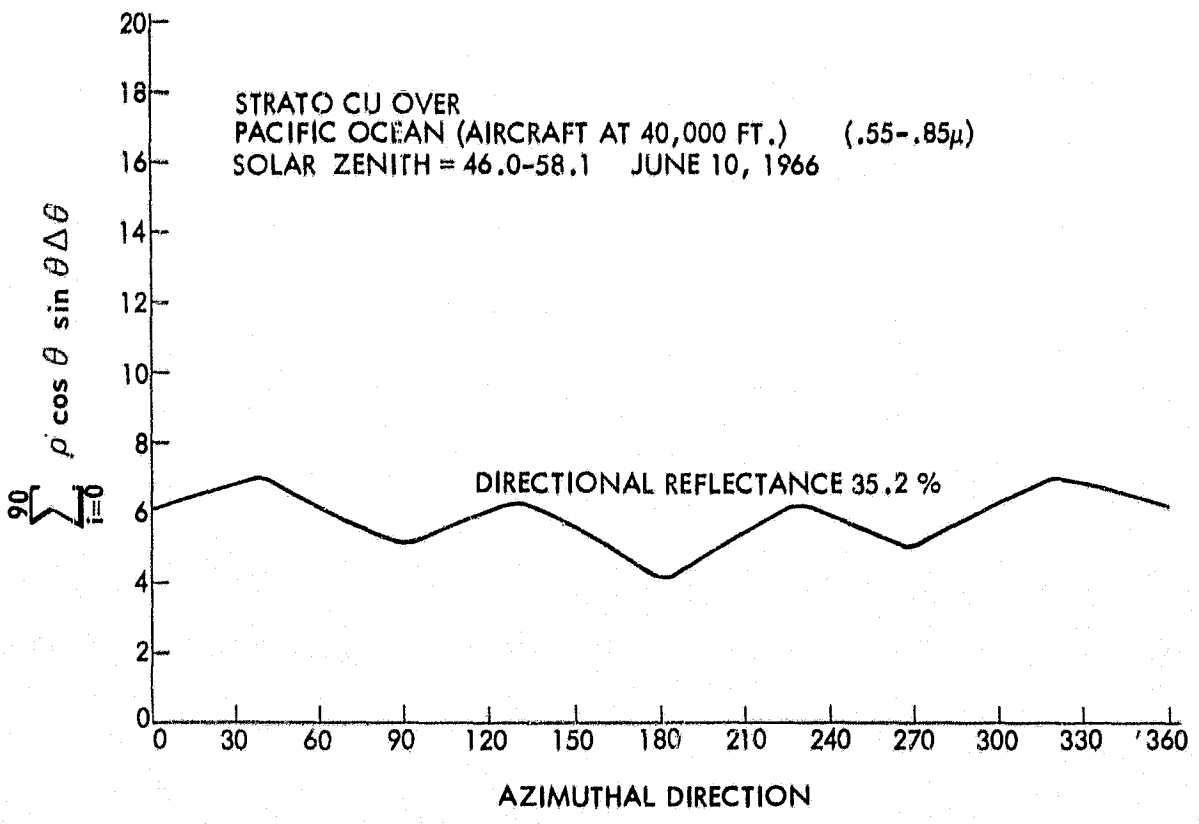

Figure 23–Numerical integration of ρ over θ vs. azimuthal direction for strato cumulus tops at 2,300 ft. over Pacific Ocean.

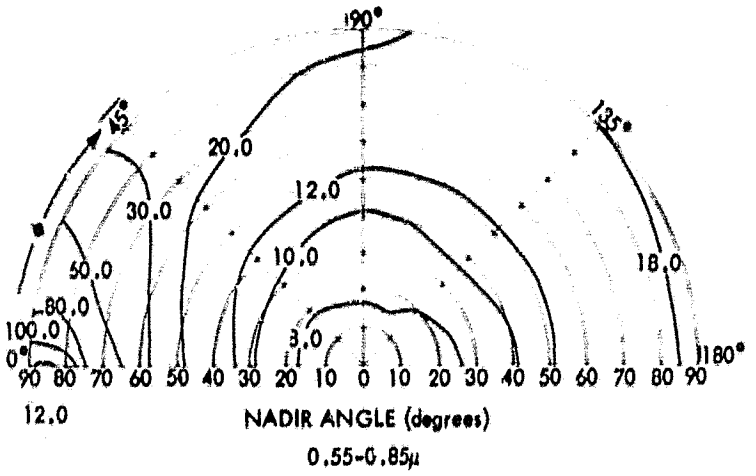

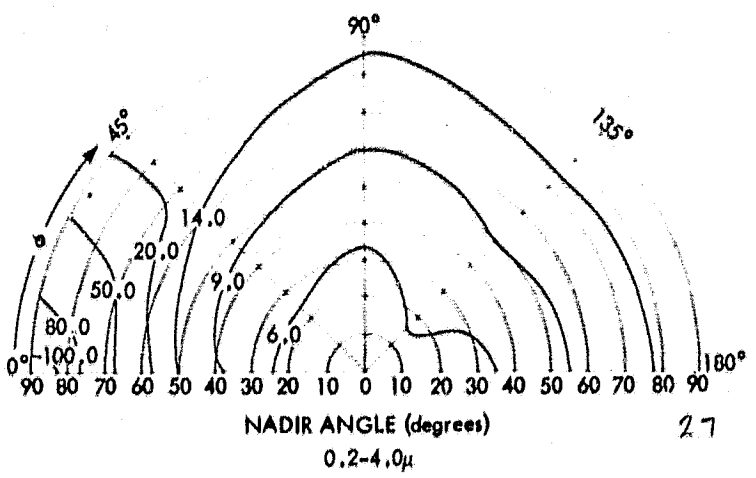

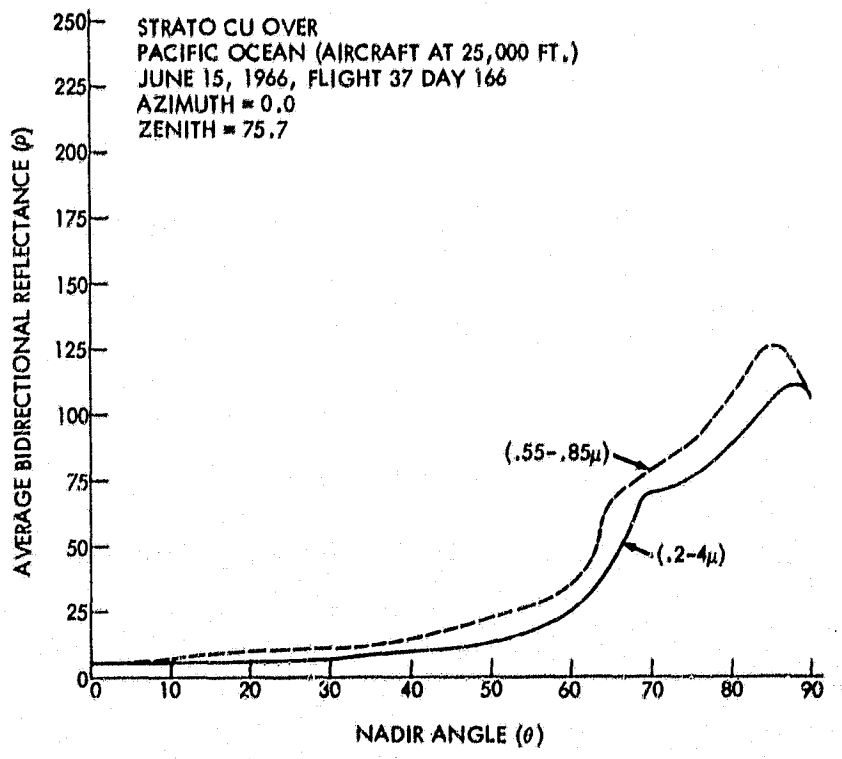

Figure 24--Bidirectional reflectances of strato cumulus over the Pacific Ocean.

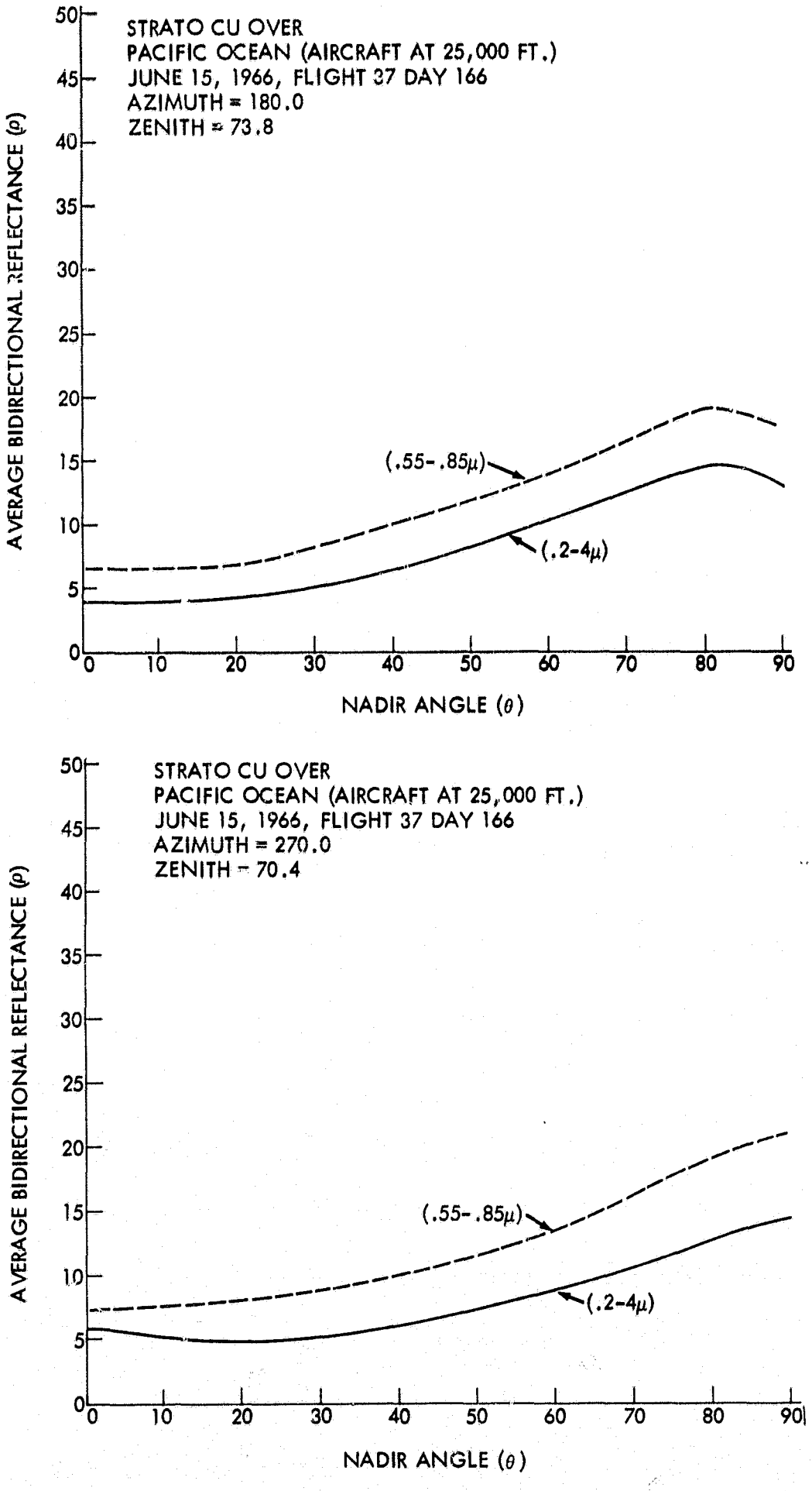

Figure 25–Bidirectional reflectances of strato cumulus over the Pacific Ocean.

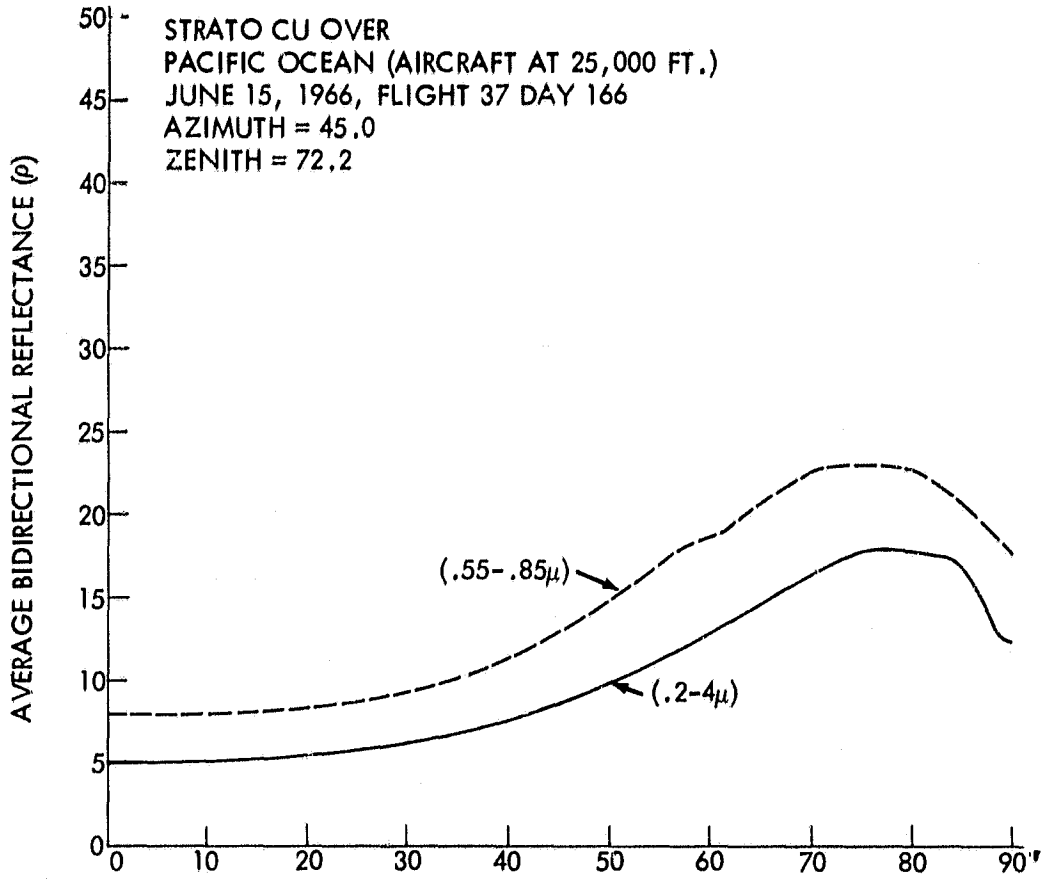

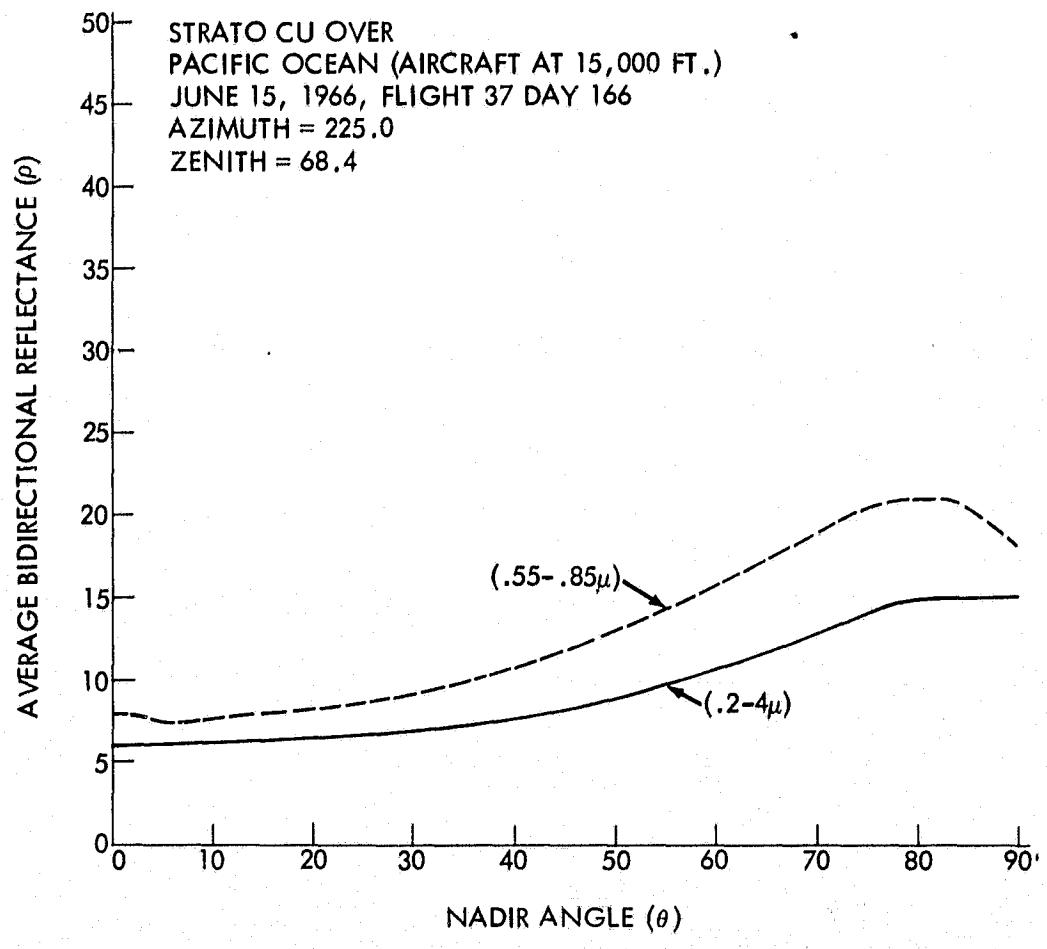

Figure 26–Bidirectional reflectances of strato cumulus over the Pacific Ocean.

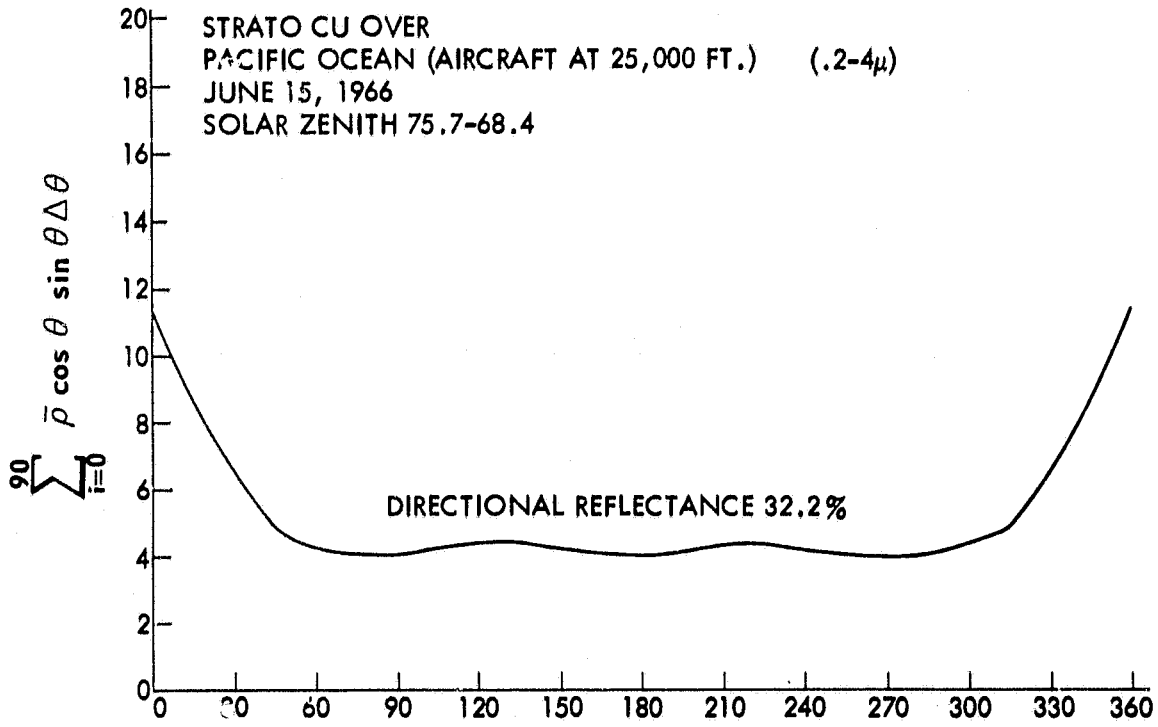

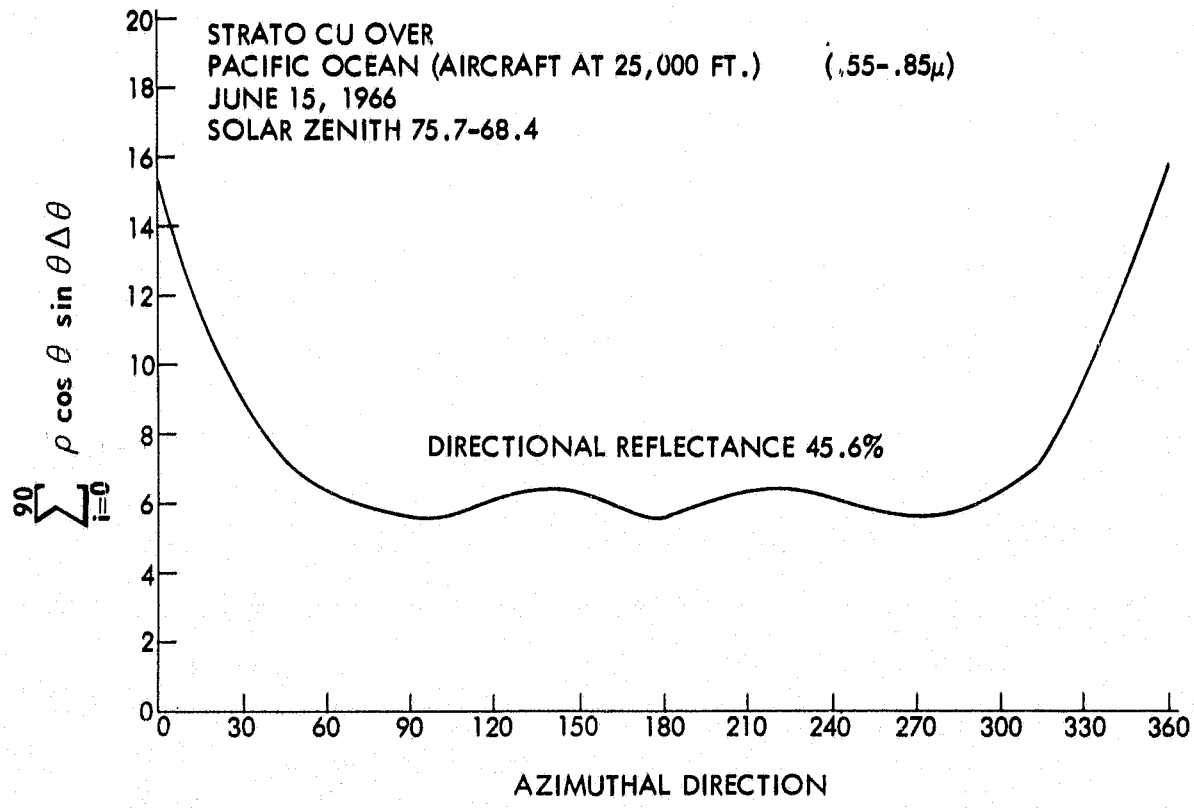

Figure 27–Numerical integration of $\bar{\rho}$ over θ vs. azimuthal direction for strato cumulus over the Pacific Ocean.

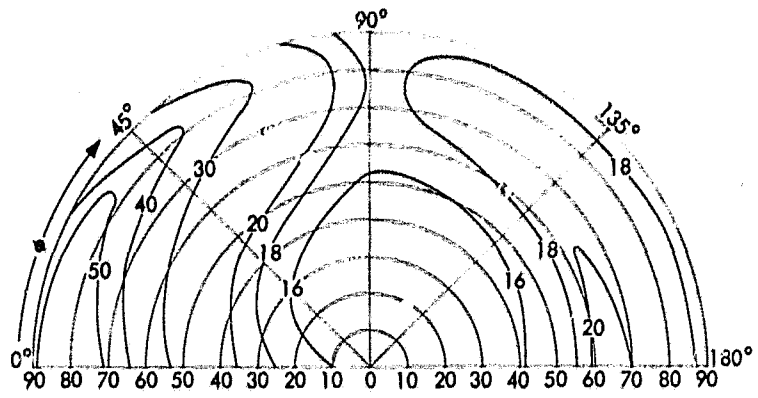

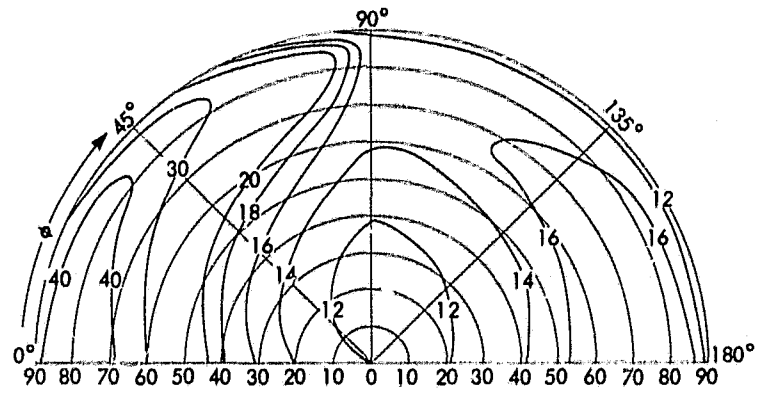

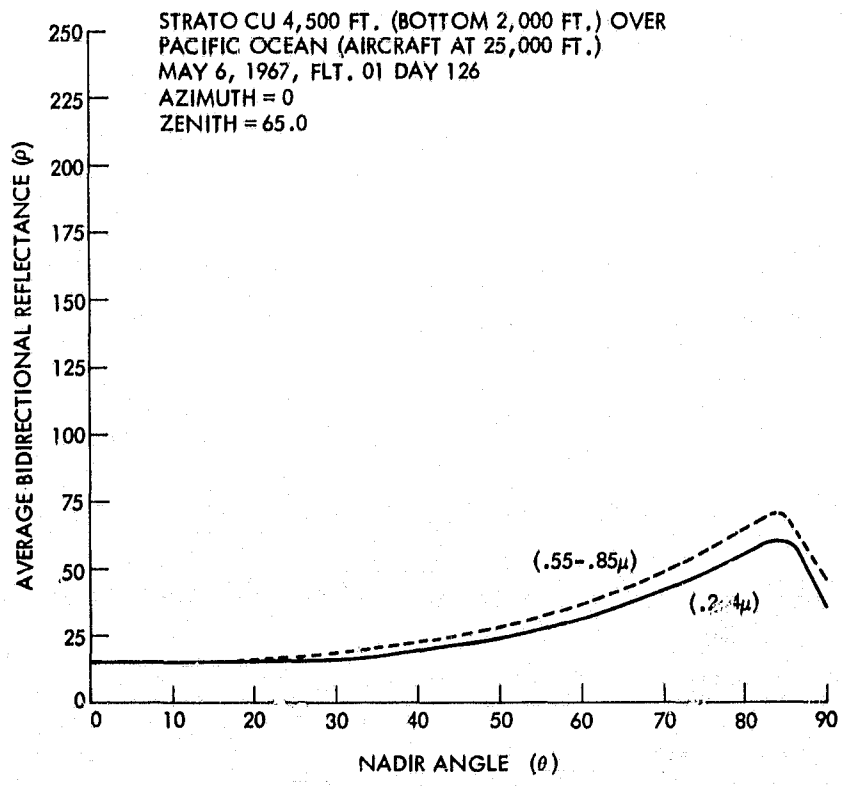

Figure 28–Bidirectional reflectances of strato cumulus at 4,500 ft., bottom at 2,000 ft., over the Pacific Ocean.

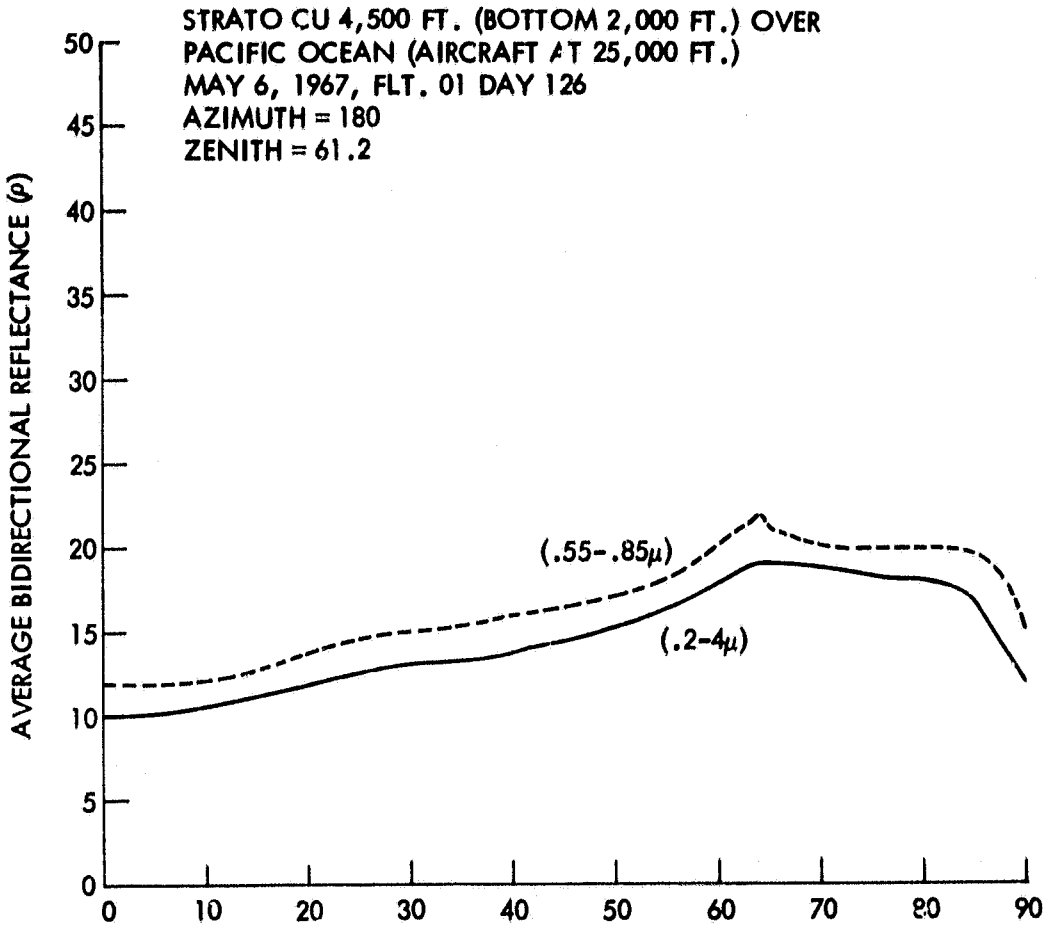

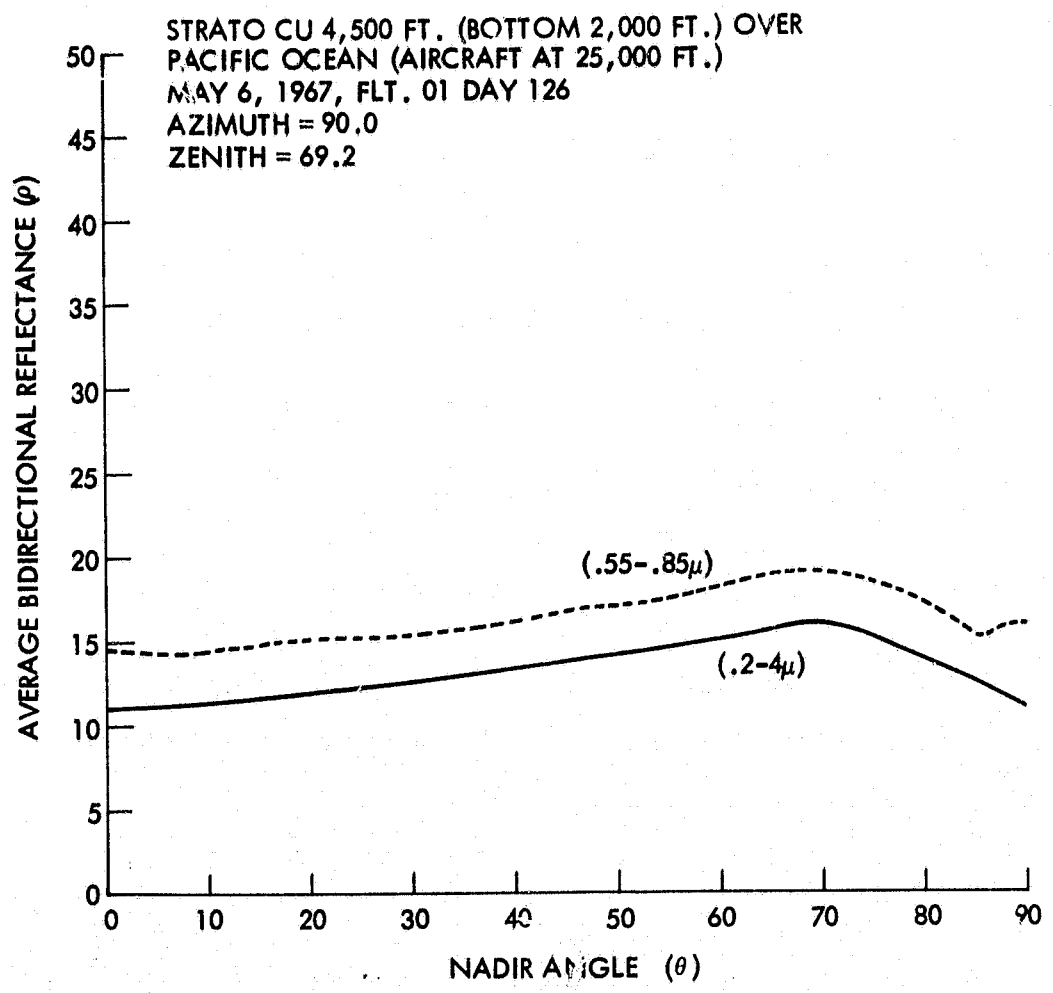

Figure 29–Bidirectional reflectances of strato cumulus at 4,500 ft., bottom at 2,000 ft., over the Pacific Ocean.

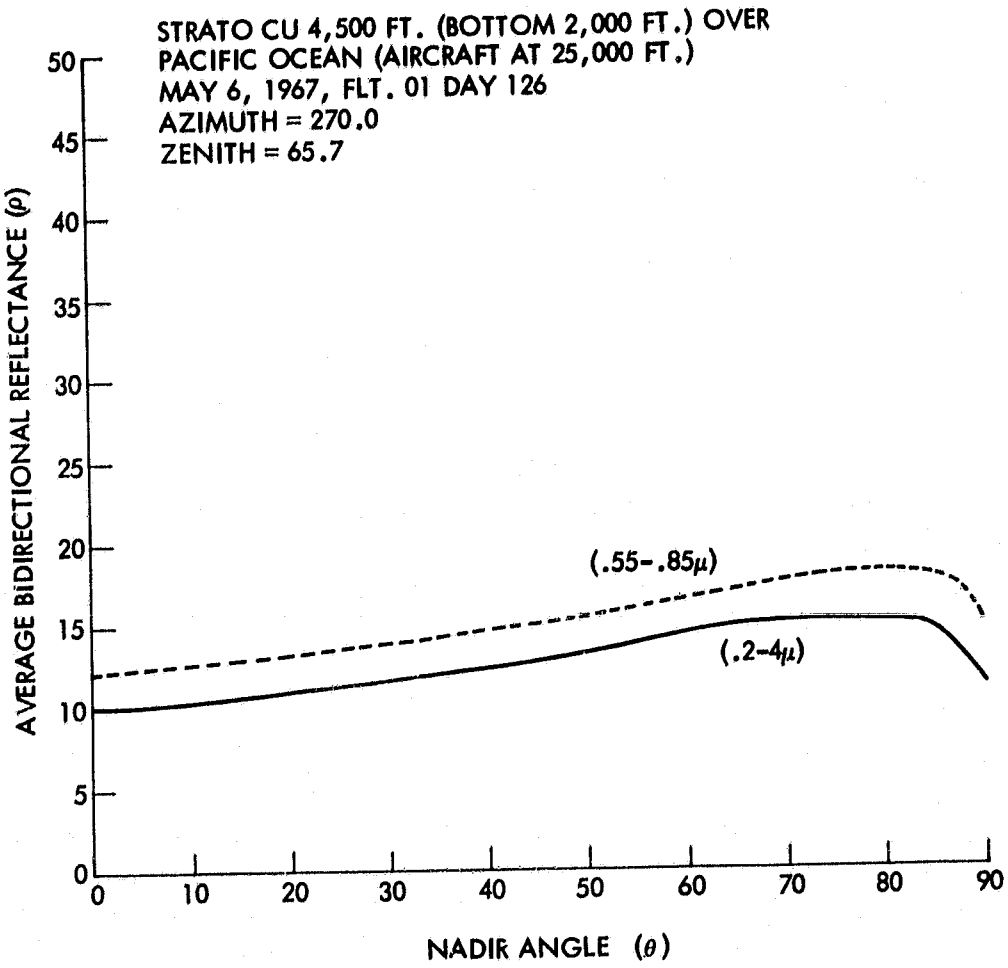

Figure 30–Bidirectional reflectances of strato cumulus at 4,500 ft., bottom at 2,000 ft., over the Pacific Ocean.

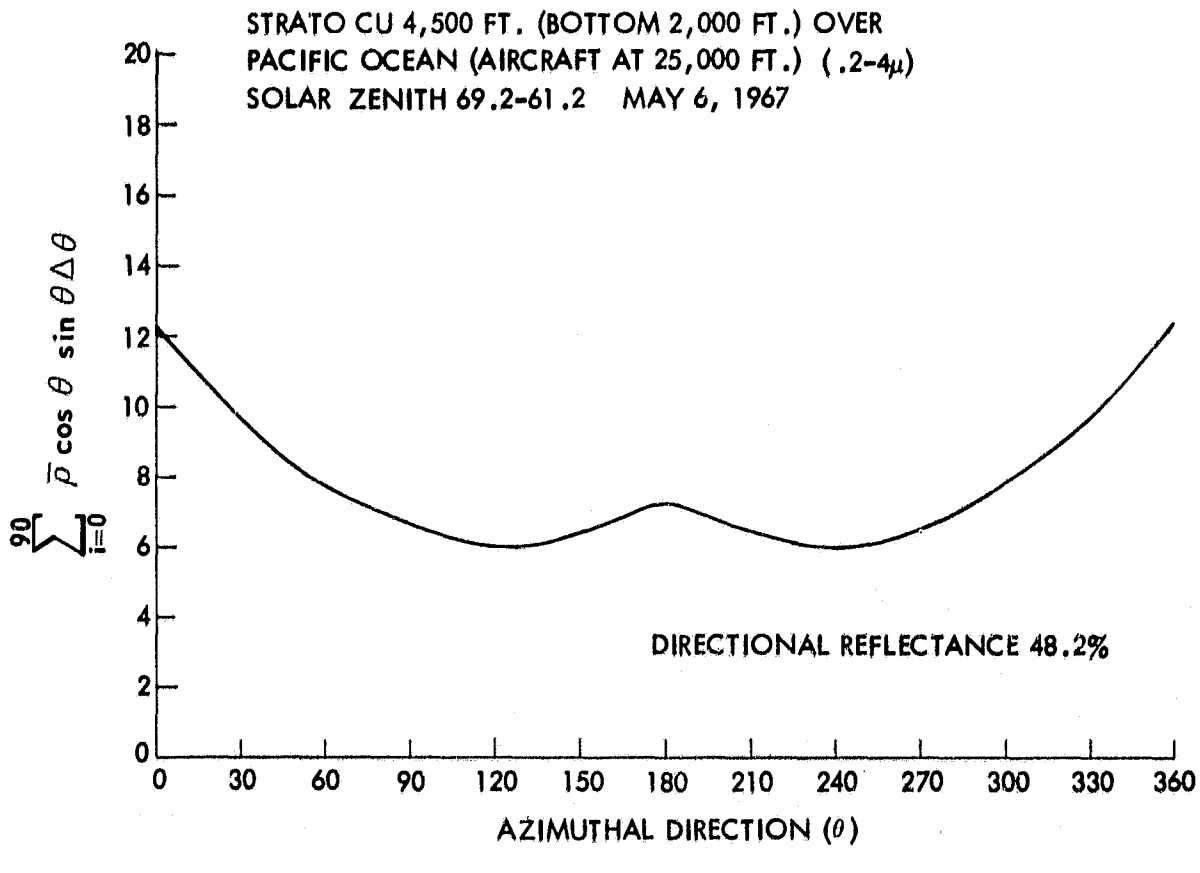

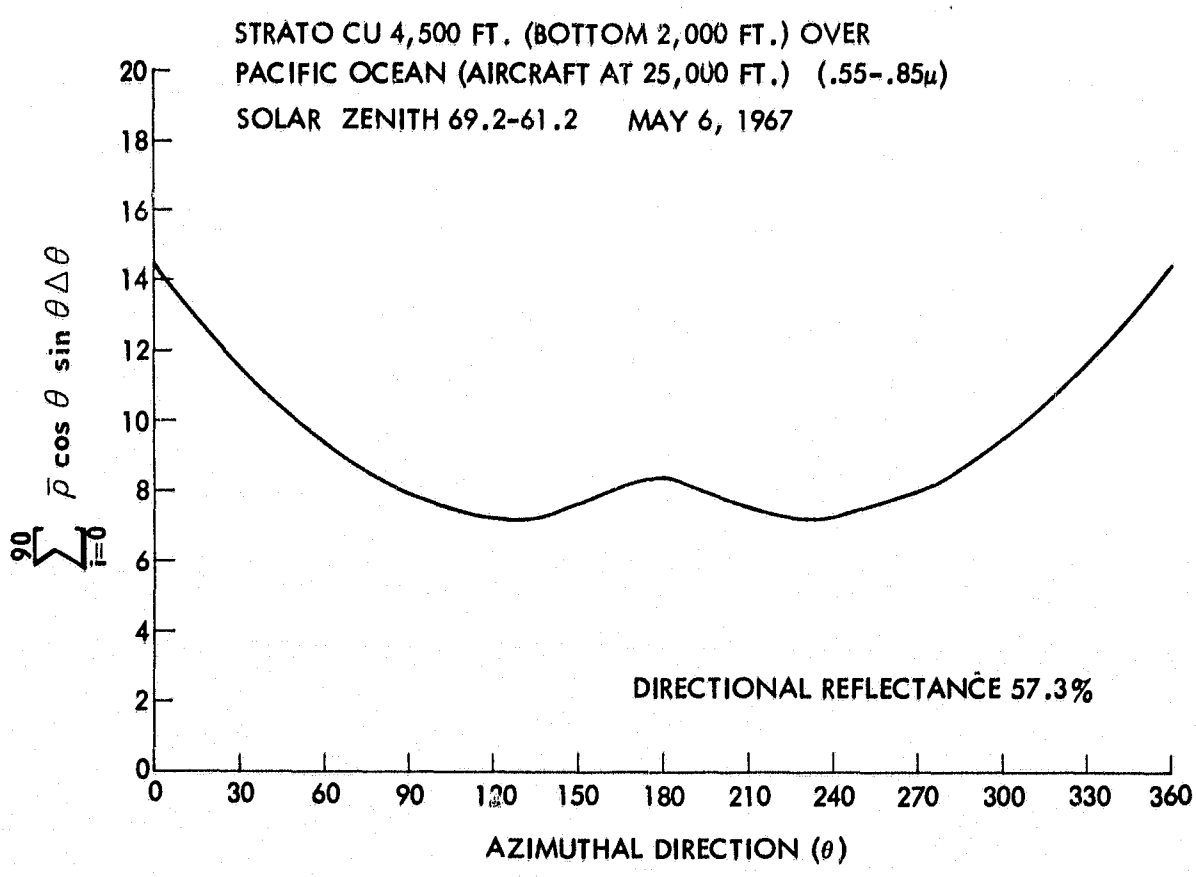

Figure 31–Numerical integration of $\bar{\rho}$ over θ vs. azimuthal direction for strato cumulus tops at 4,500 ft., bases at 2,000 ft. over the Pacific Ocean.

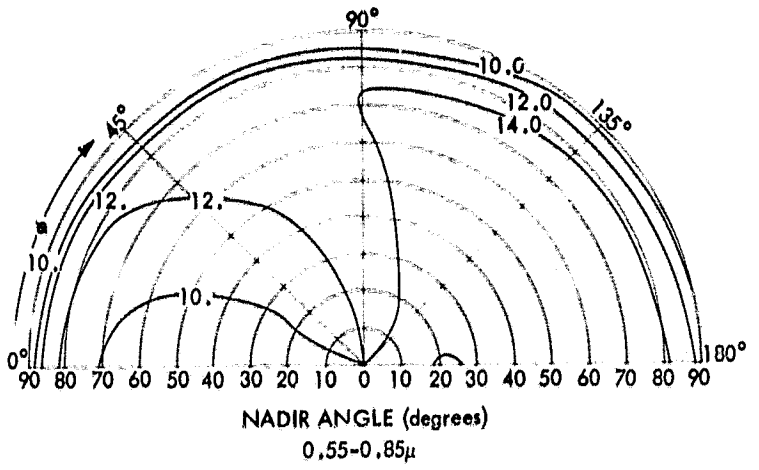

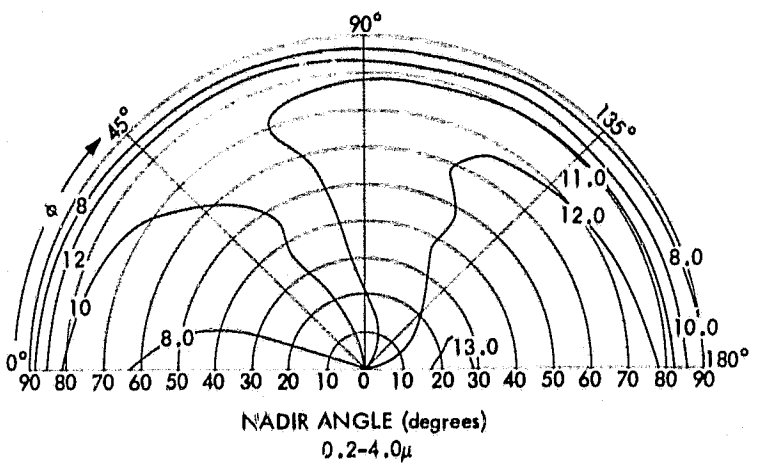

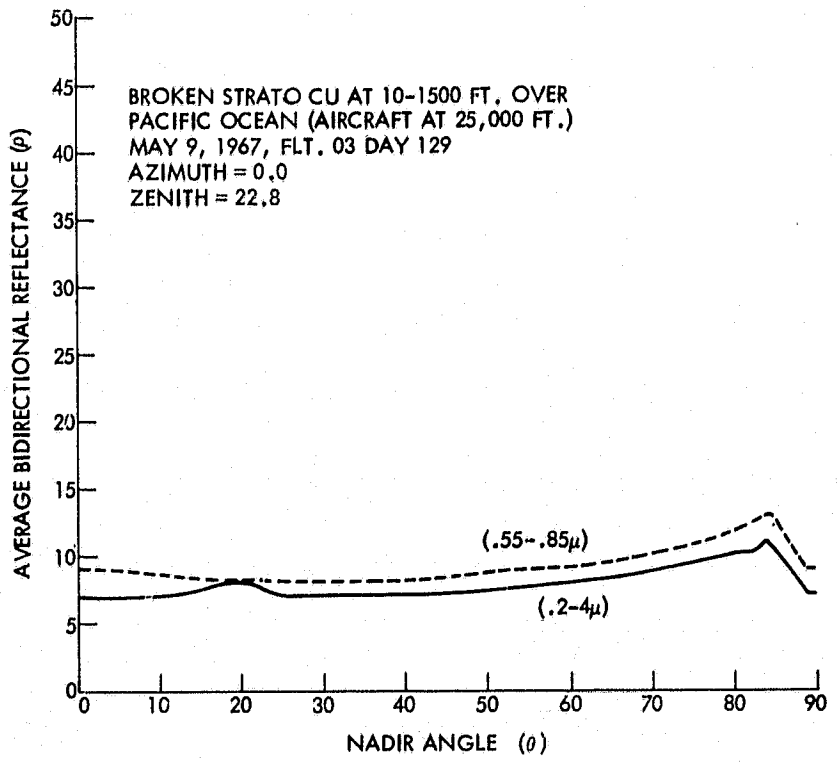

Figure 32–Bidirectional reflectances of broken strato cumulus at 15,000 ft. over Pacific Ocean.

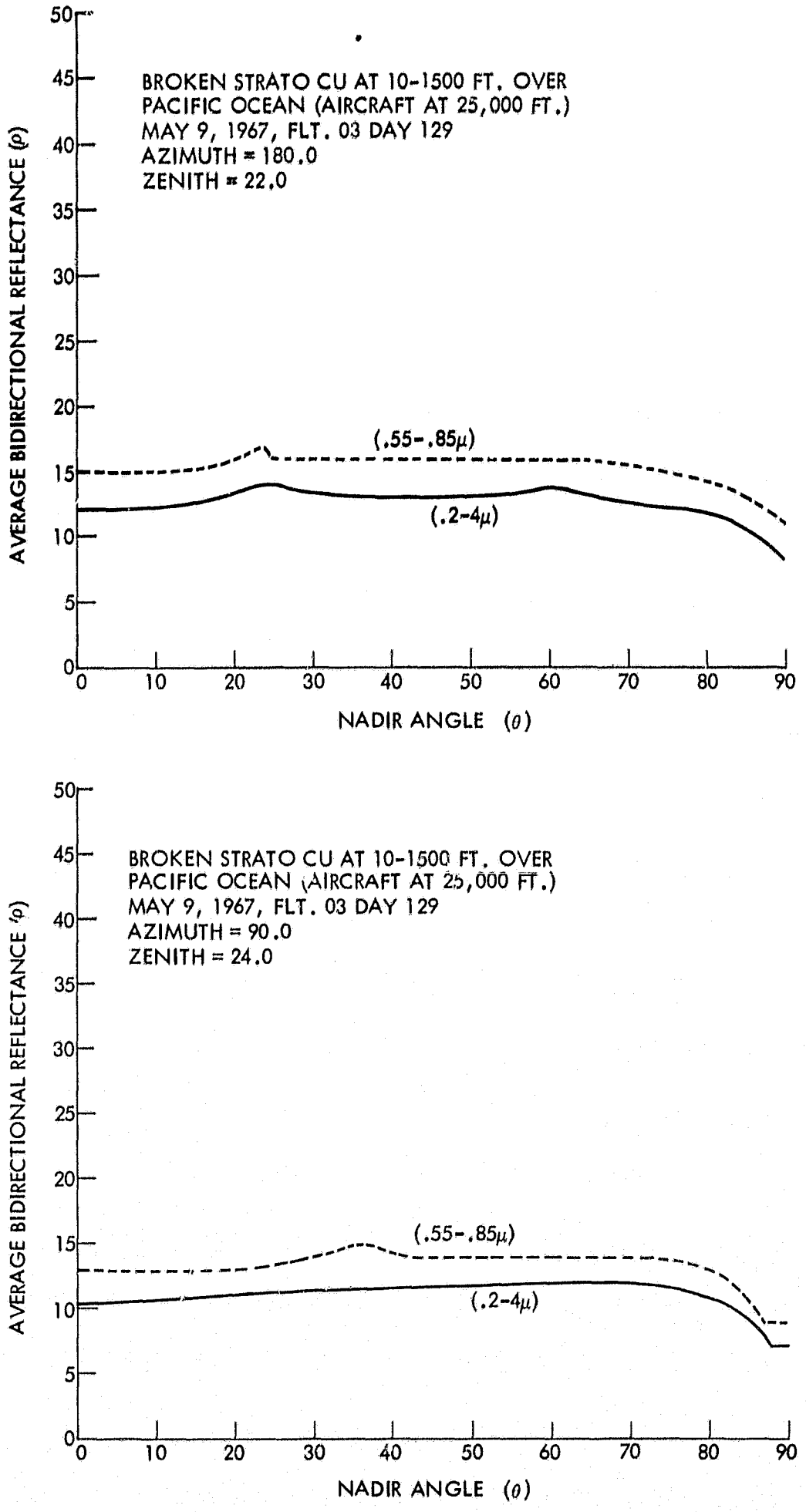

Figure 33–Bidirectional reflectances of broken strato cumulus at 15,000 ft. over Pacific Ocean.

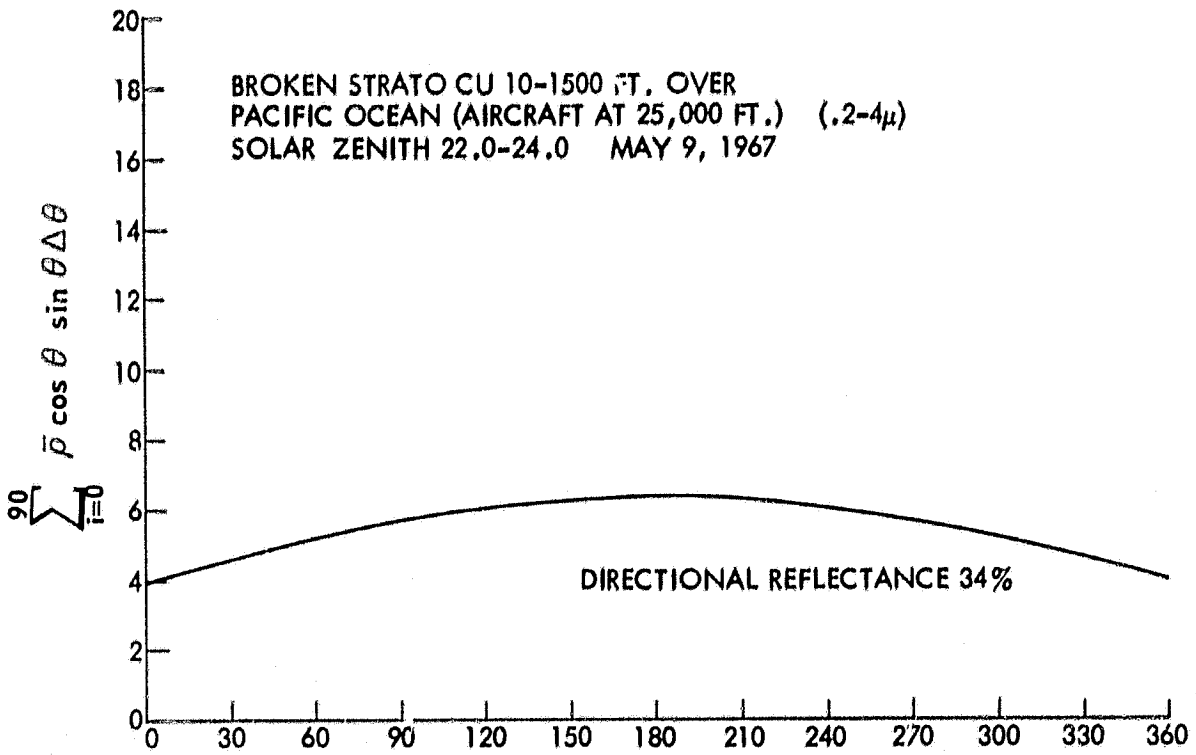

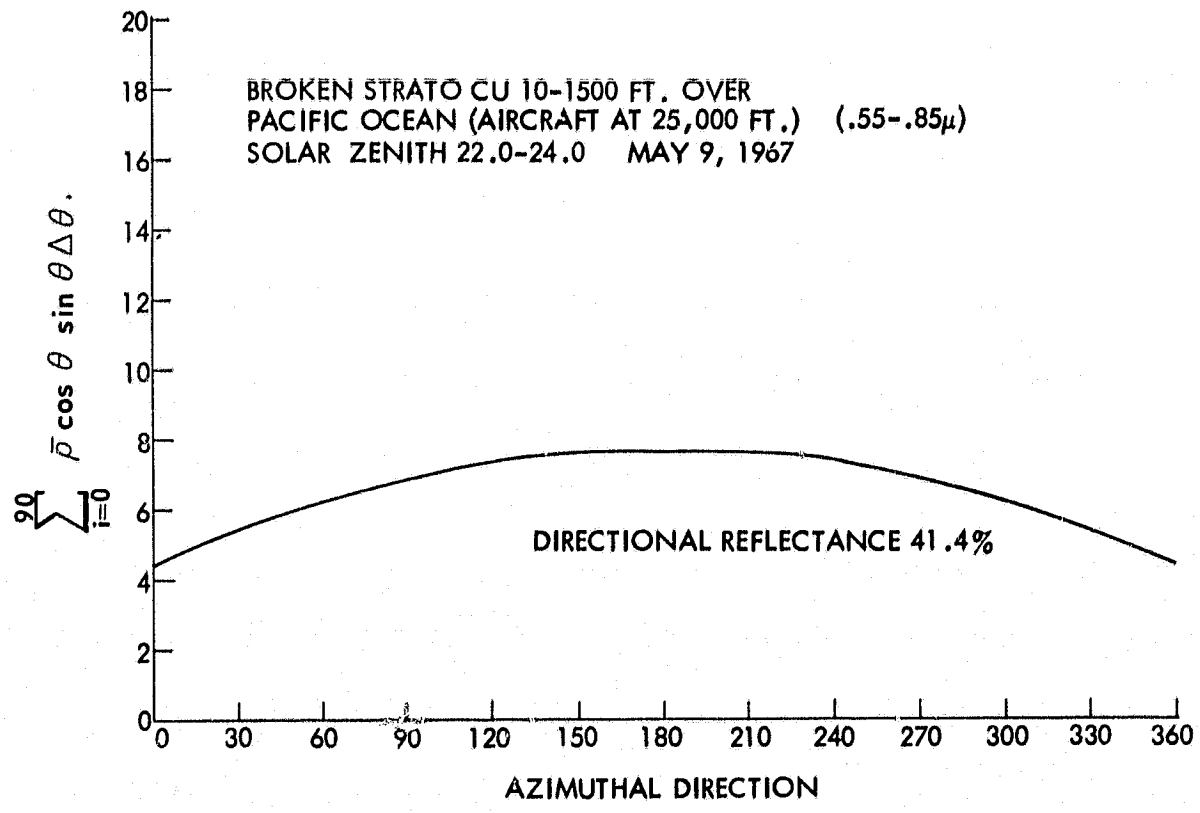

Figure 34–Numerical integration of $\bar{\rho}$ over θ vs. azimuthal direction for broken strato cumulus tops at 10,000 ft. over Pacific Ocean.

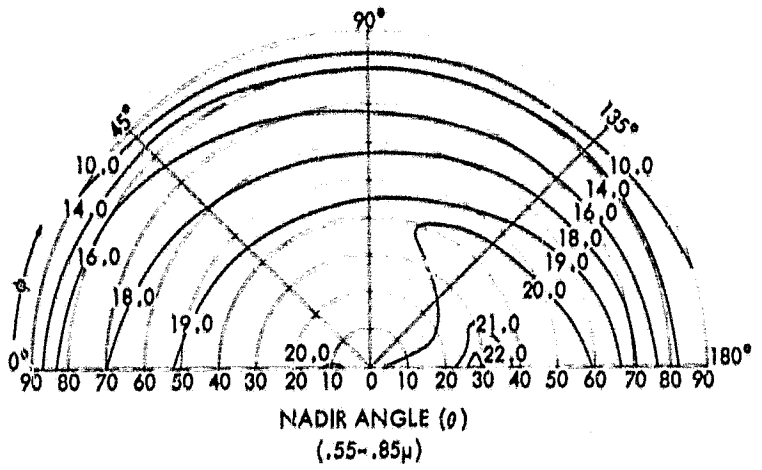

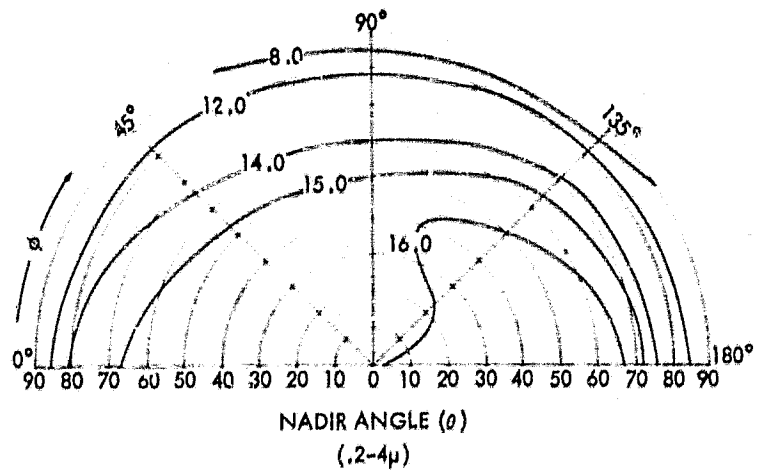

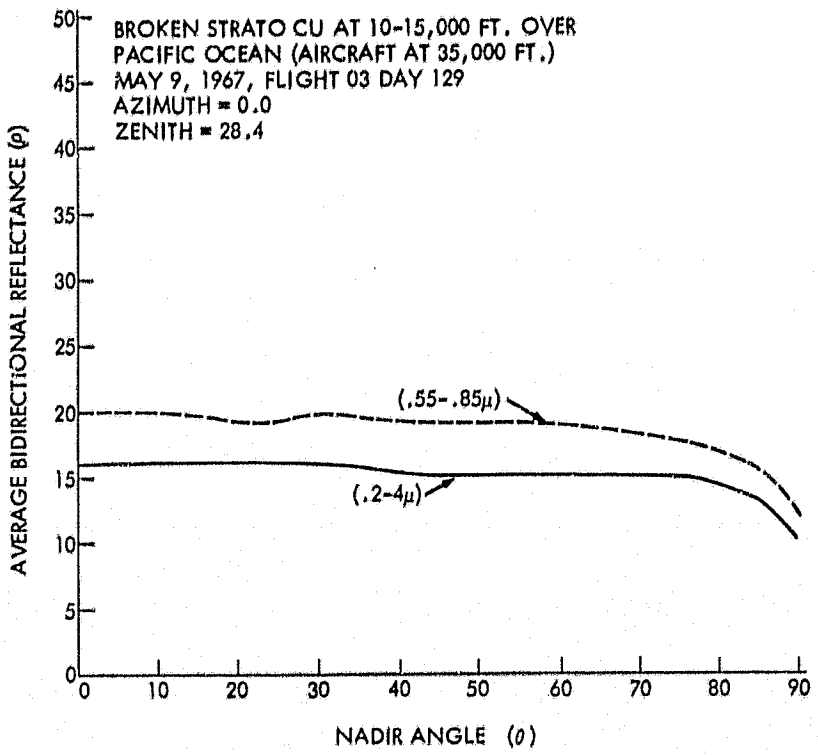

Figure 35–Bidirectional reflectances of strato cumulus at 10,000 ft. over Pacific Ocean.

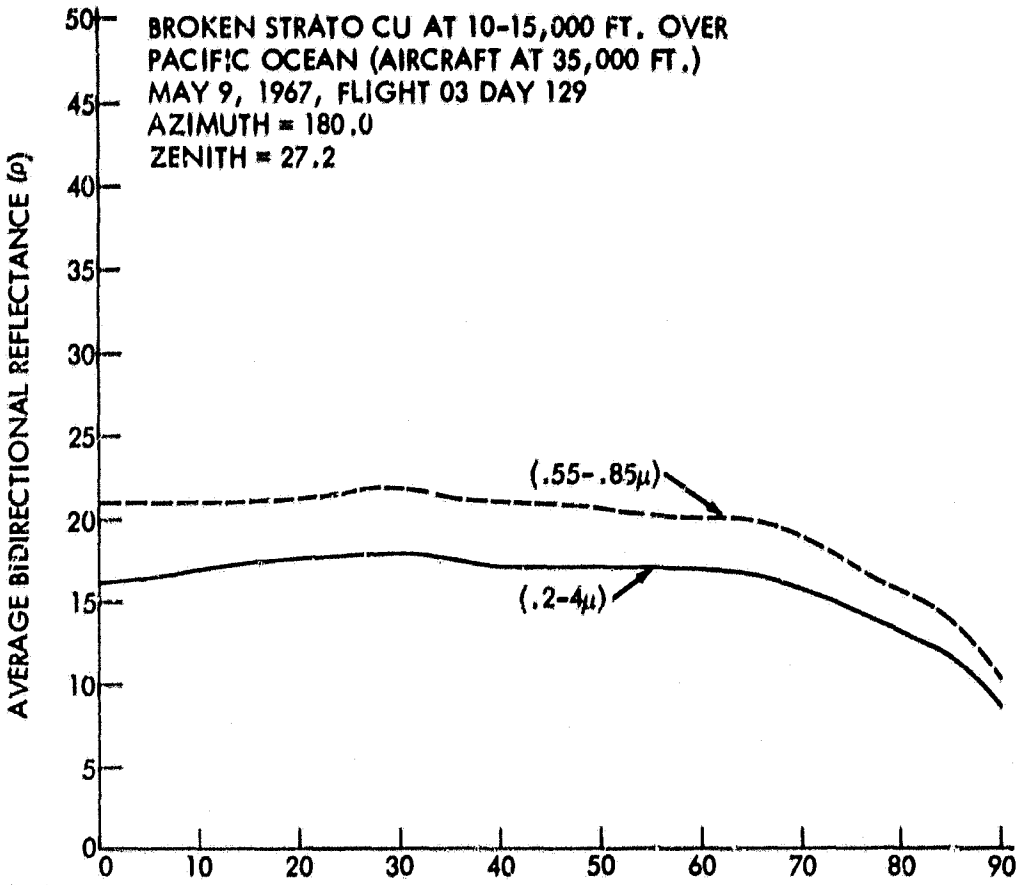

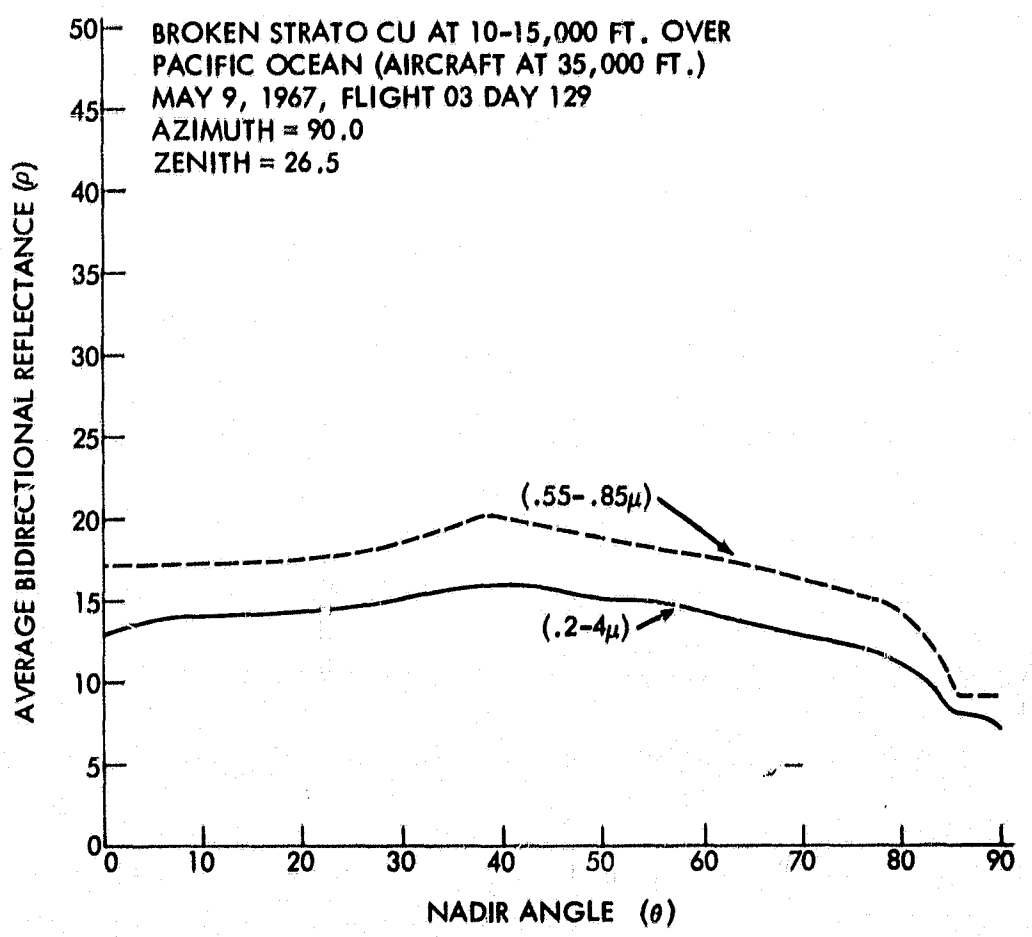

Figure 36–Bidirectional reflectances of strato cumulus at 10,000 ft. over Pacific Ocean.

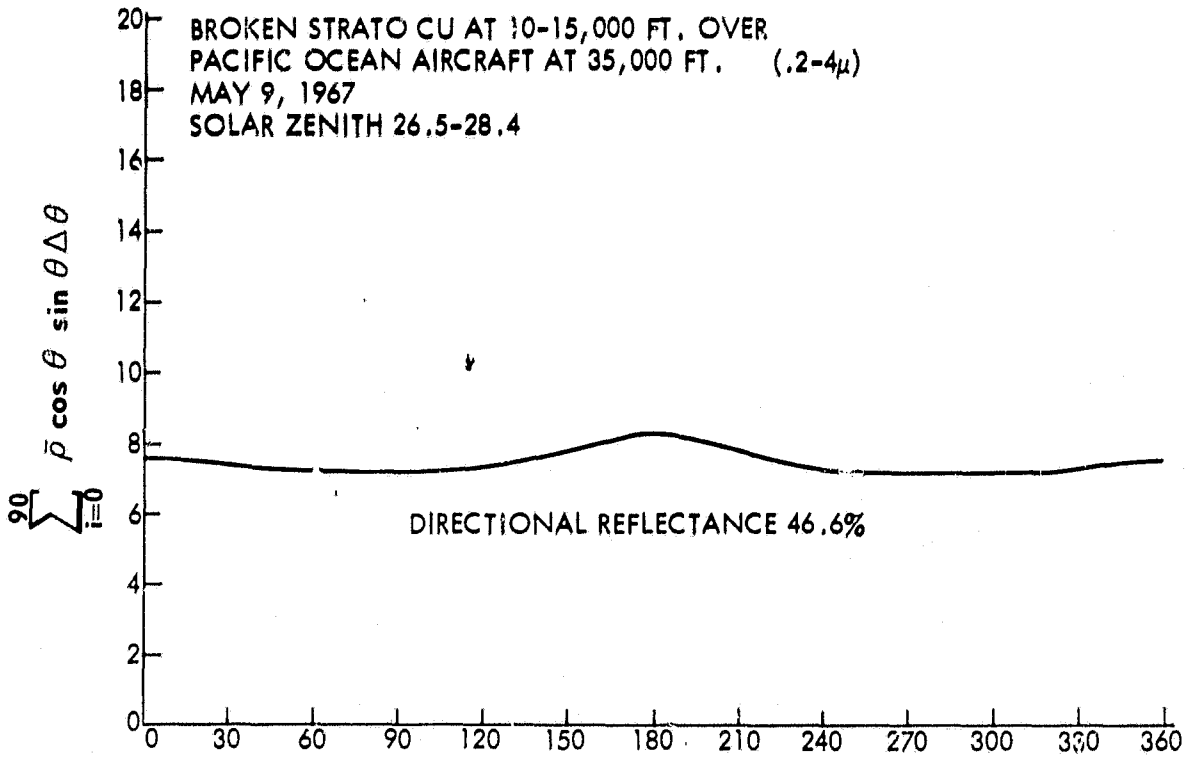

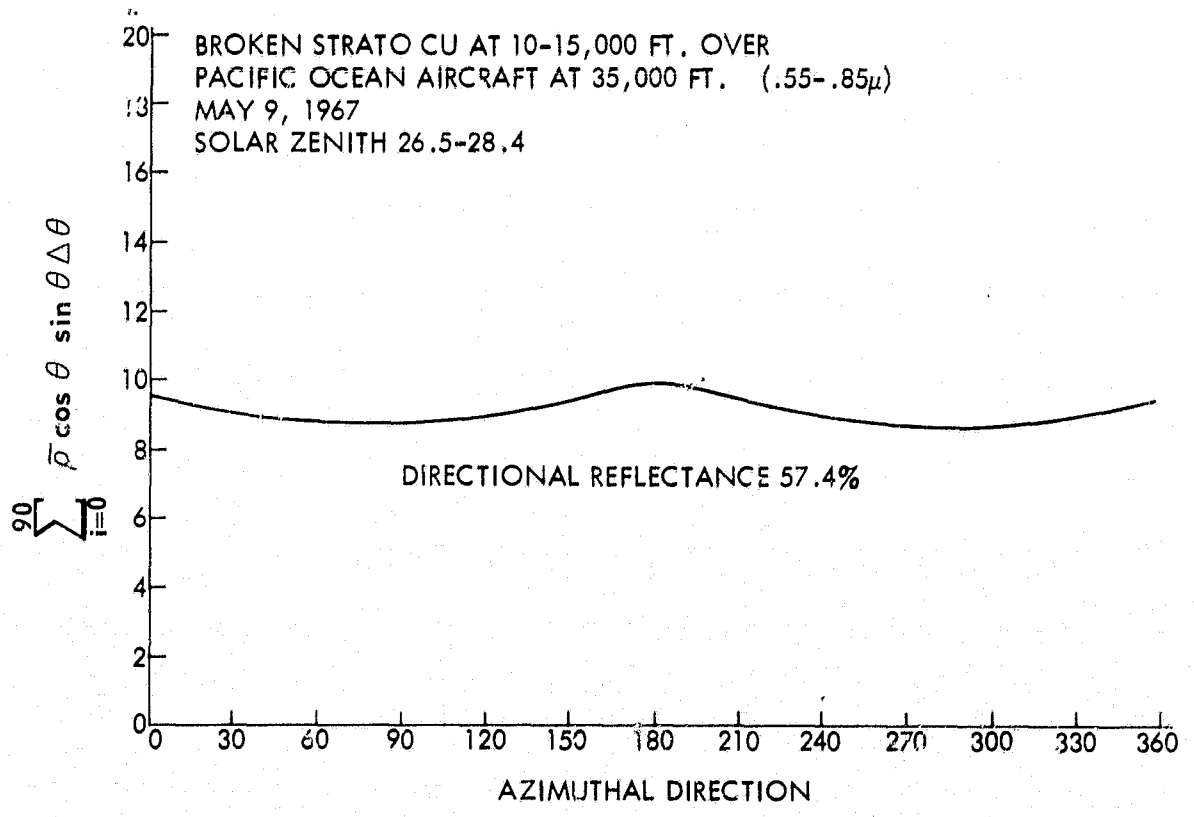

Figure 37--Numerical integration of $\bar{\rho}$ over θ vs. azimuthal direction for broken strato cumulus tops at 10-15,000 ft.

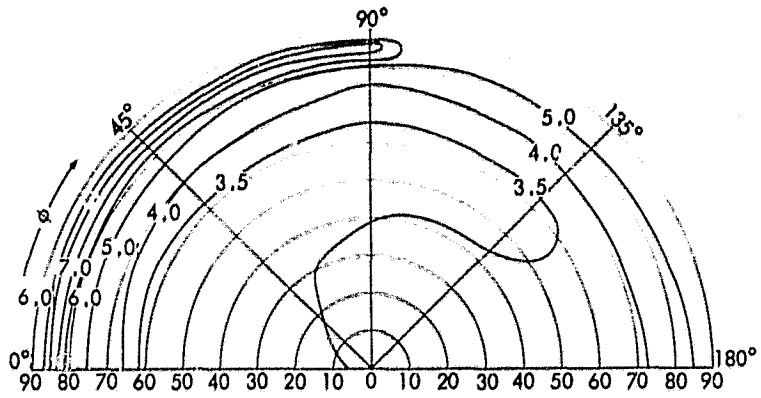

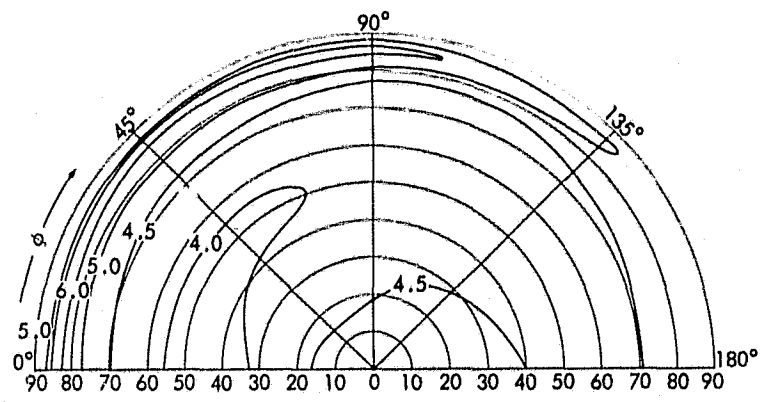

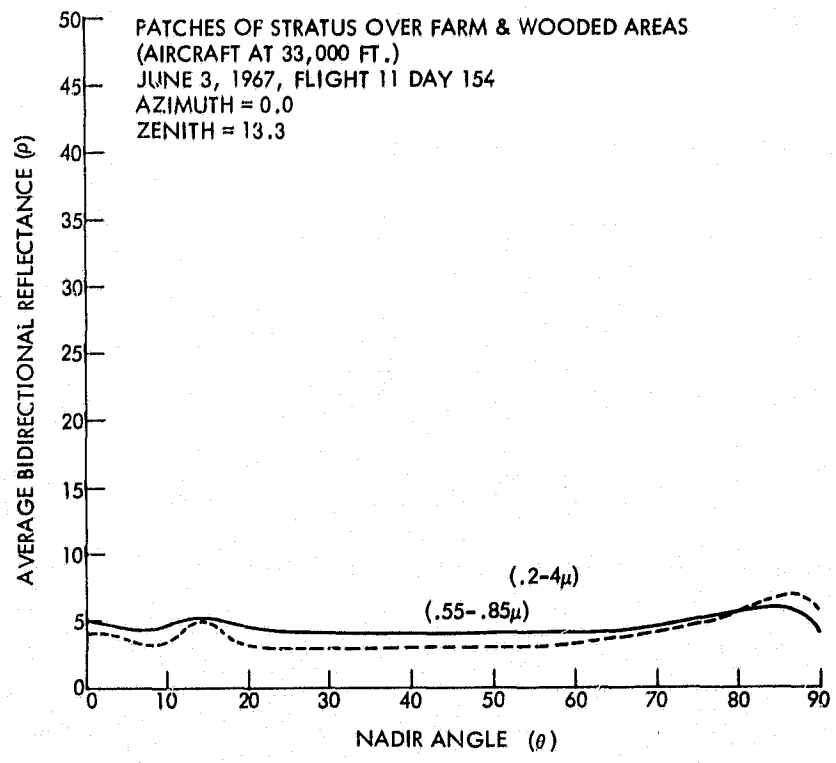

Figure 38–Bidirectional reflectances of farmland and wooded areas with patches of stratus.

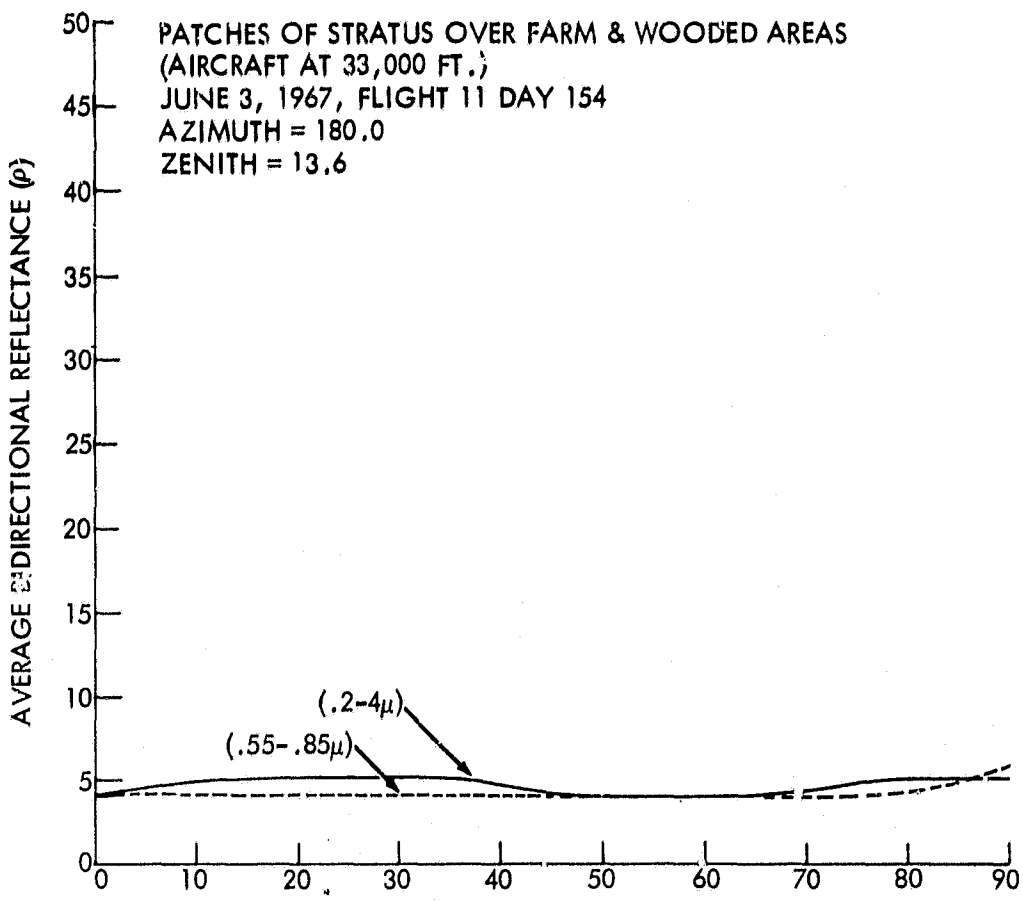

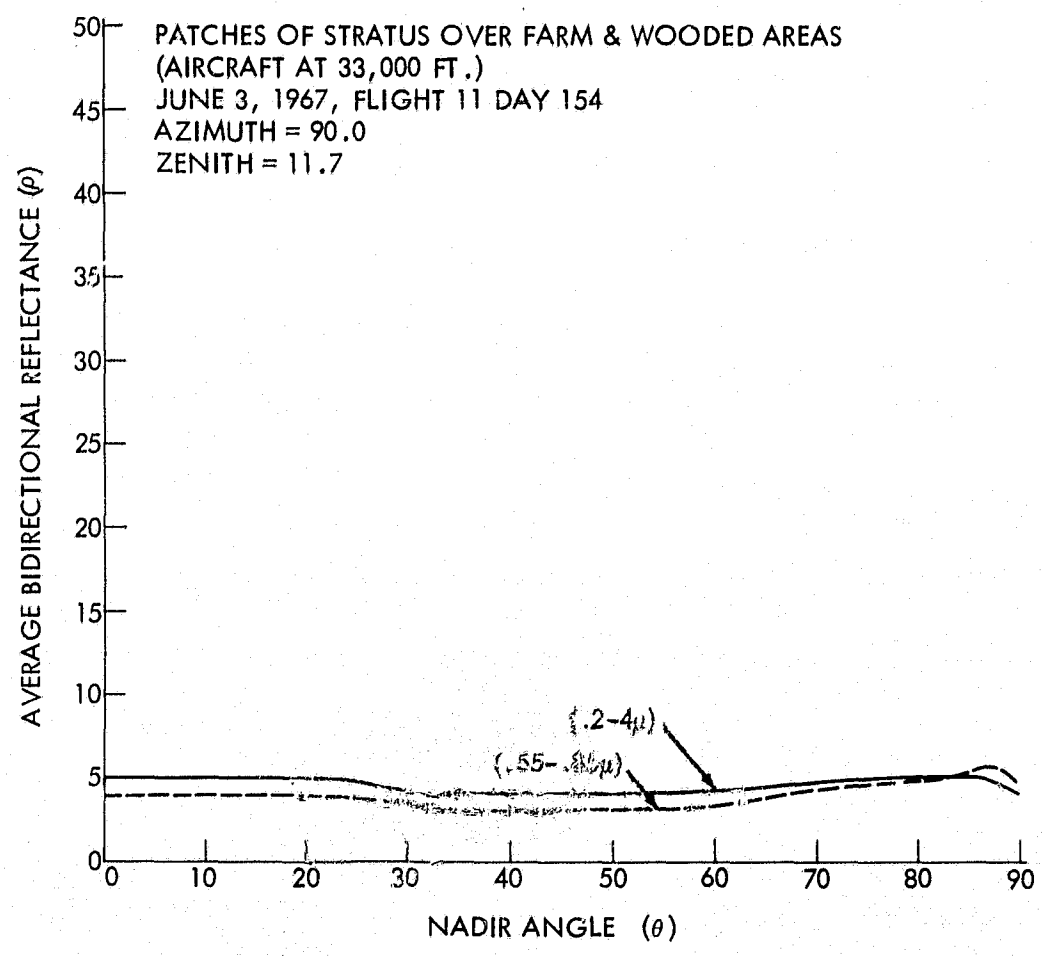

Figure 39–Bidirectional reflectances of farmland and wooded areas with patches of stratus.

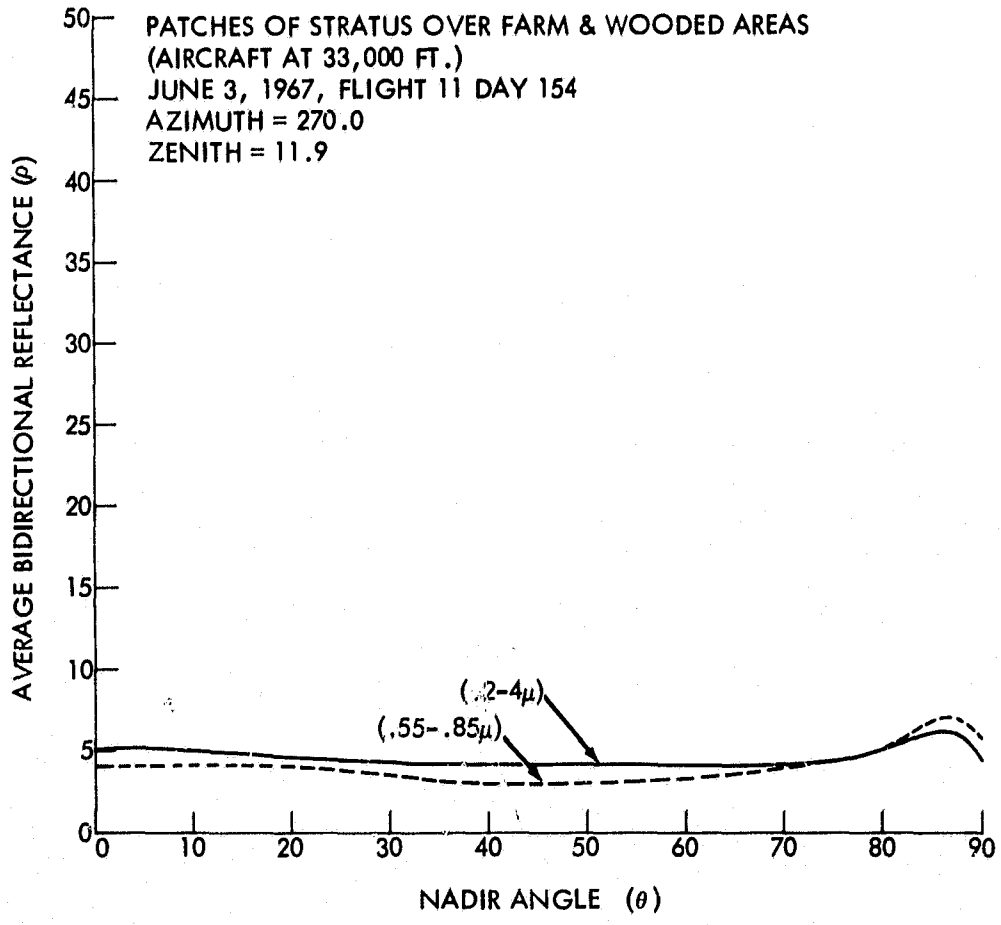

Figure 40–Bidirectional reflectances of farmland and wooded areas with patches of stratus.

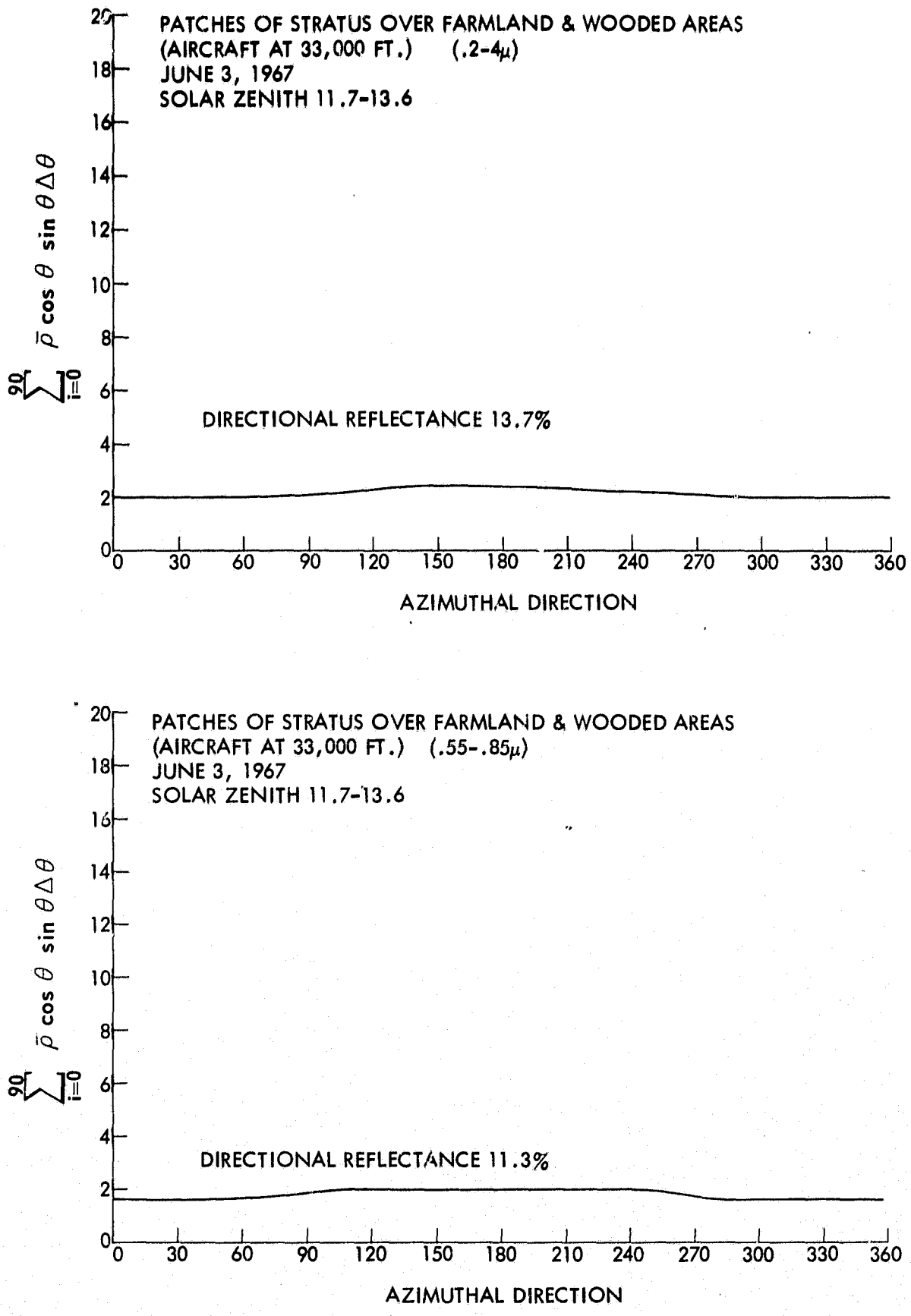

Figure 41–Numerical integration of $\bar{\rho}$ over θ vs. azimuthal direction of farmland and wooded areas with patches of stratus.

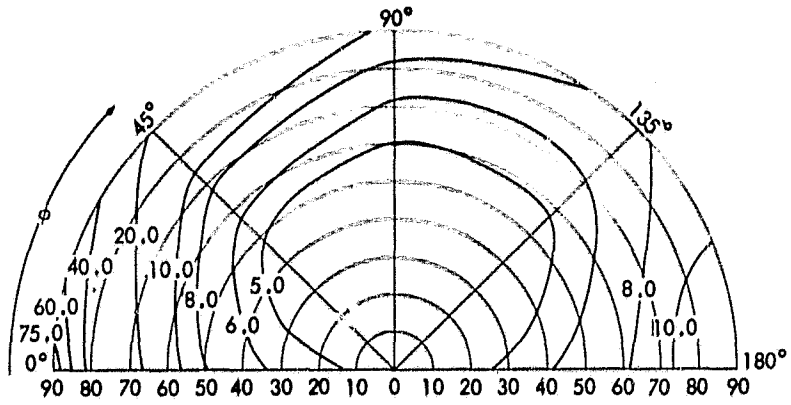

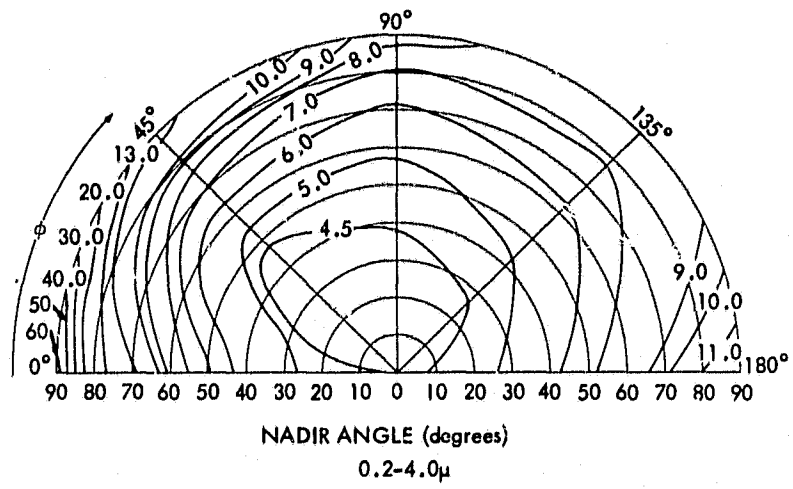

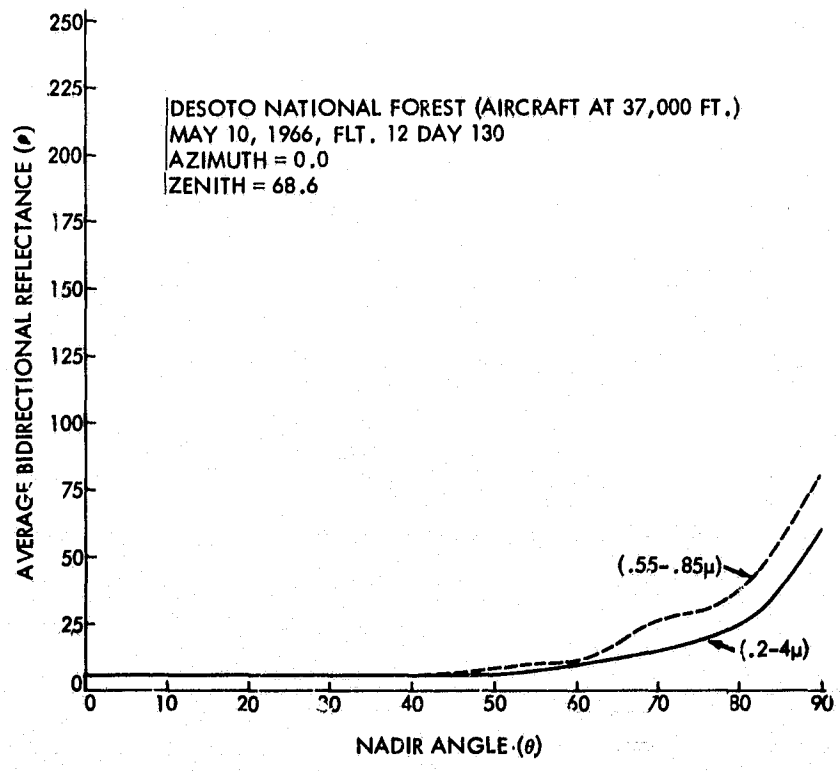

Figure 42–Bidirectional reflectances of the Desoto National Forest.

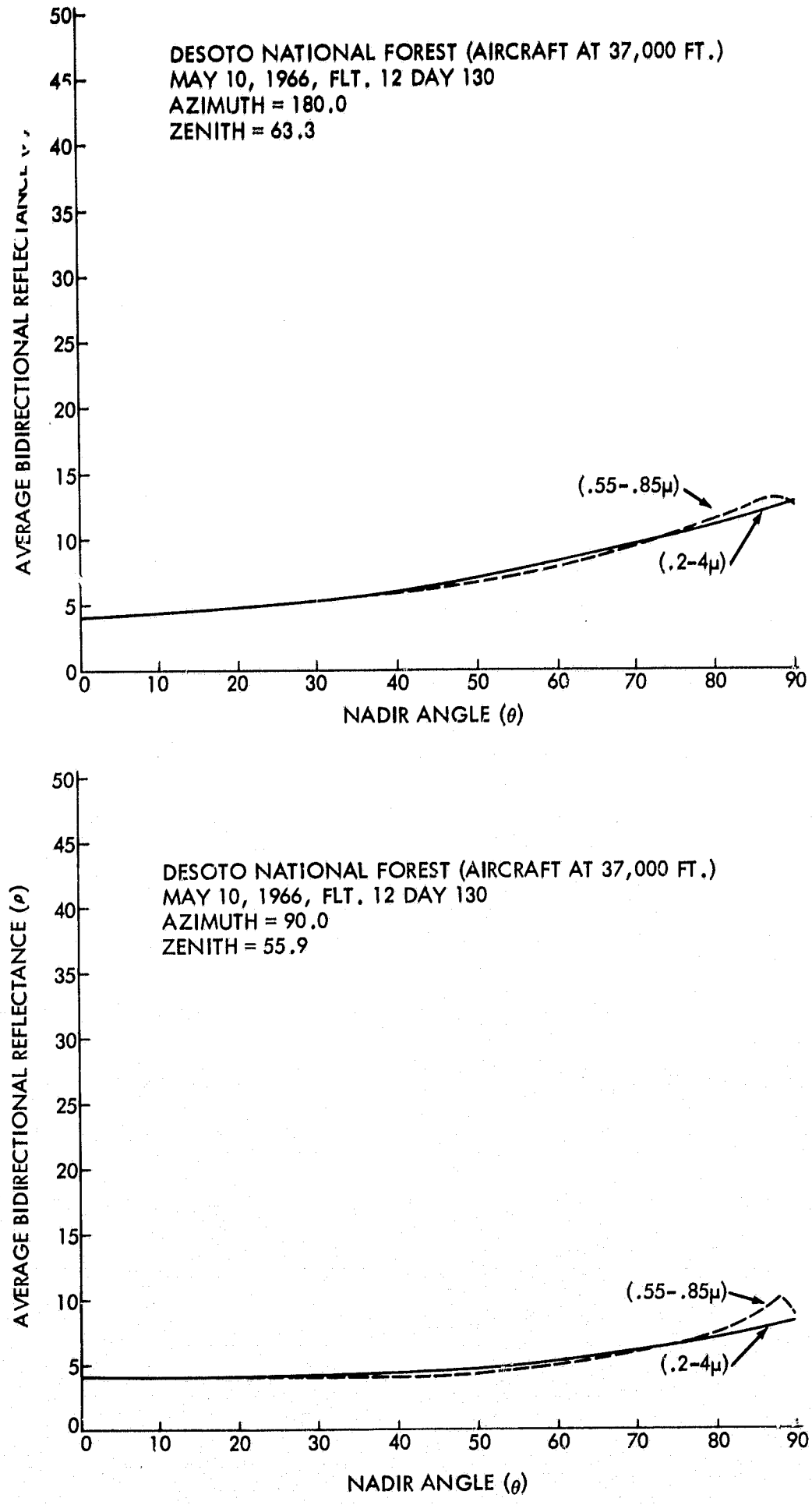

Figure 43–Bidirectional reflectances of the Desoto National Forest.

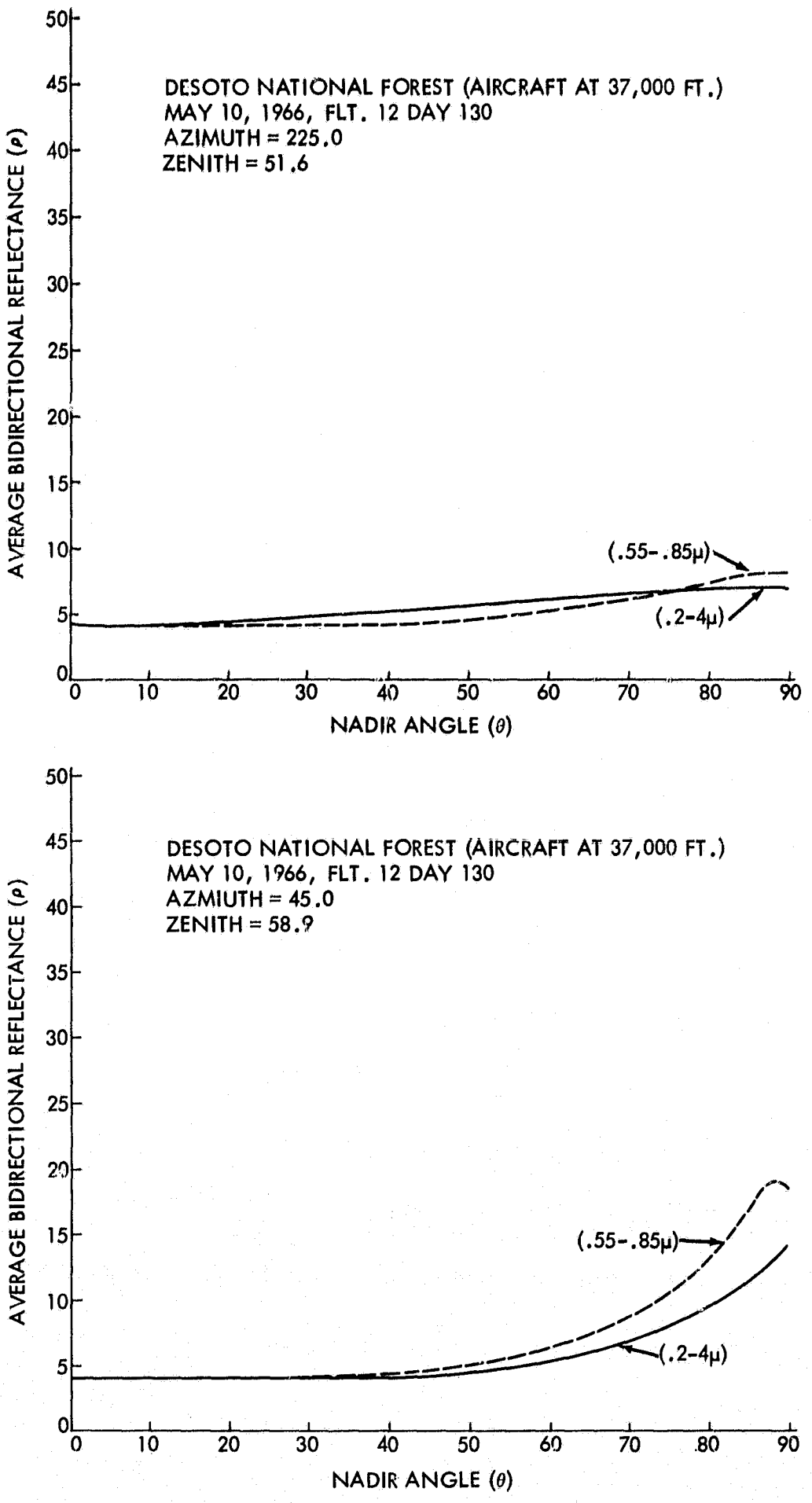

Figure 44–Bidirectional reflectances of the Desoto National Forest.

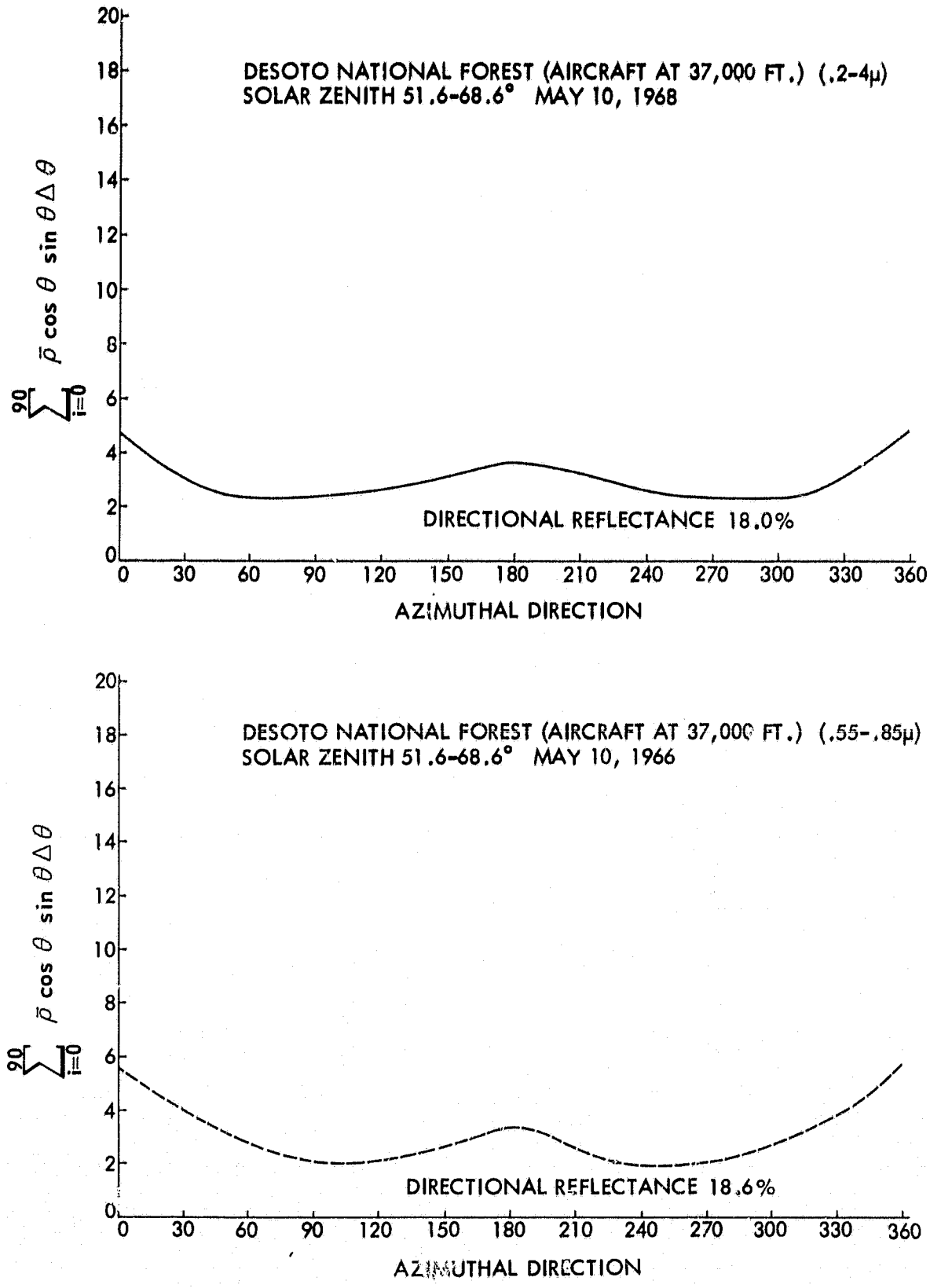

Figure 45–Numerical integration of $\bar{\rho}$ over θ vs. azimuthal direction for the Desoto National Forest.

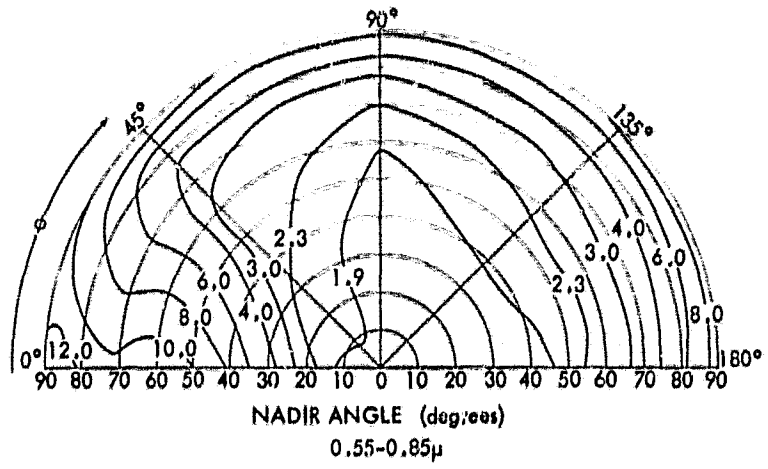

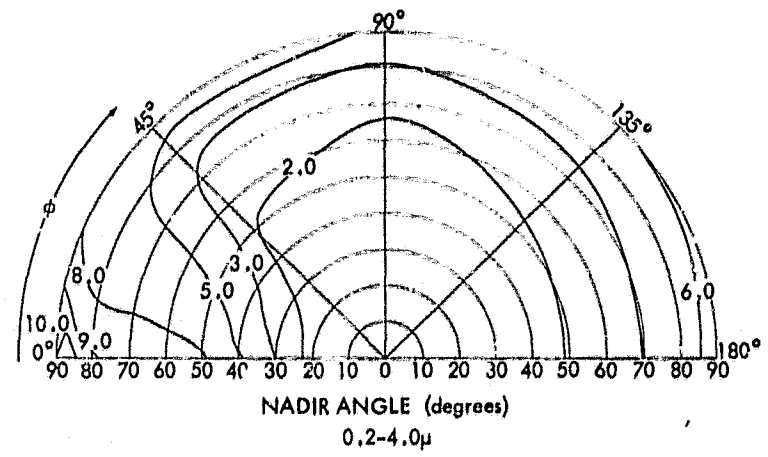

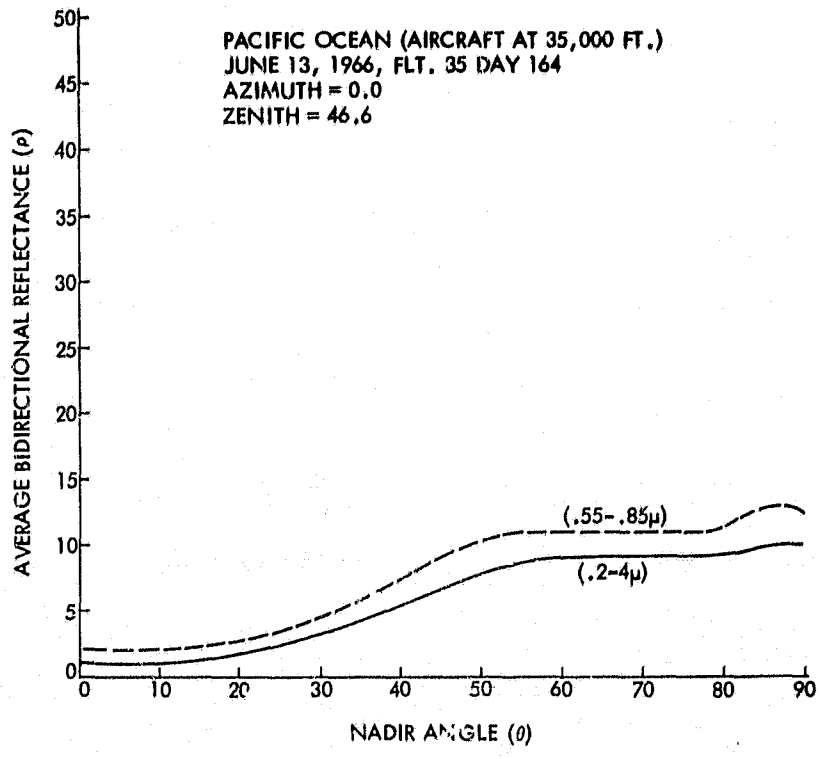

Figure 46--Bidirectional reflectances of the Pacific Ocean at 37° 40′ N 122° 48′ W.

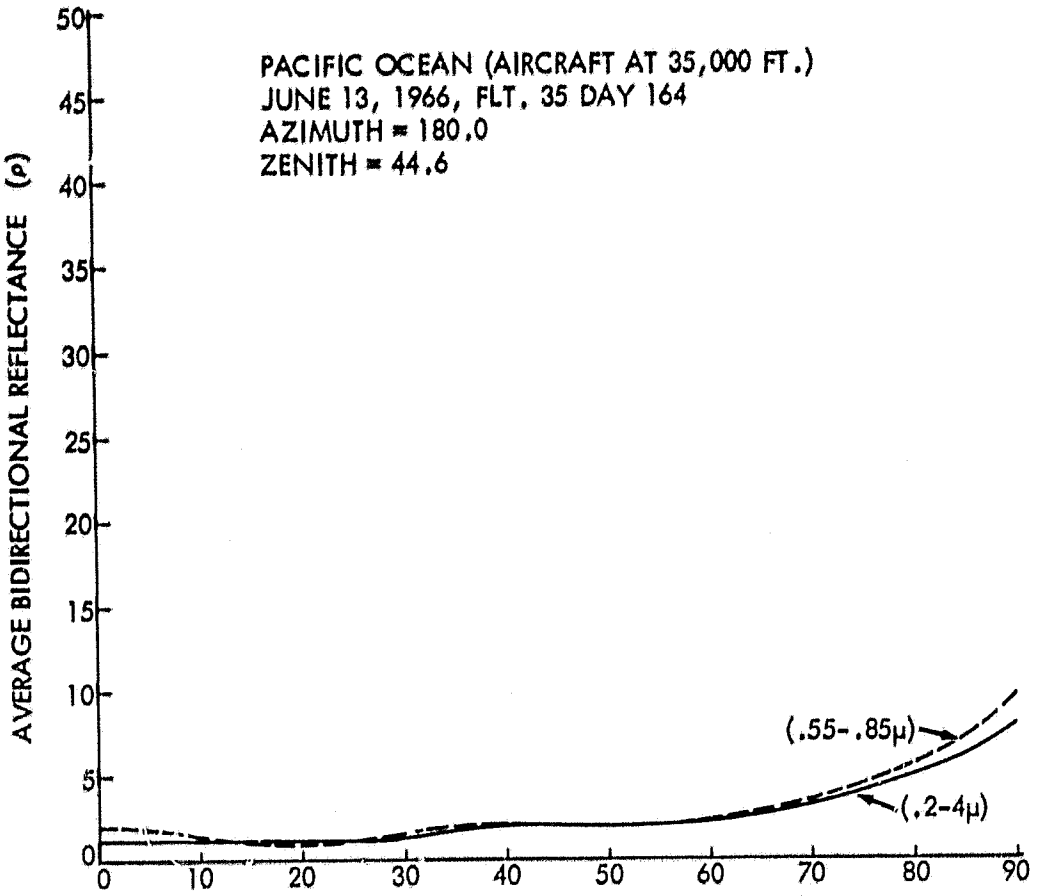

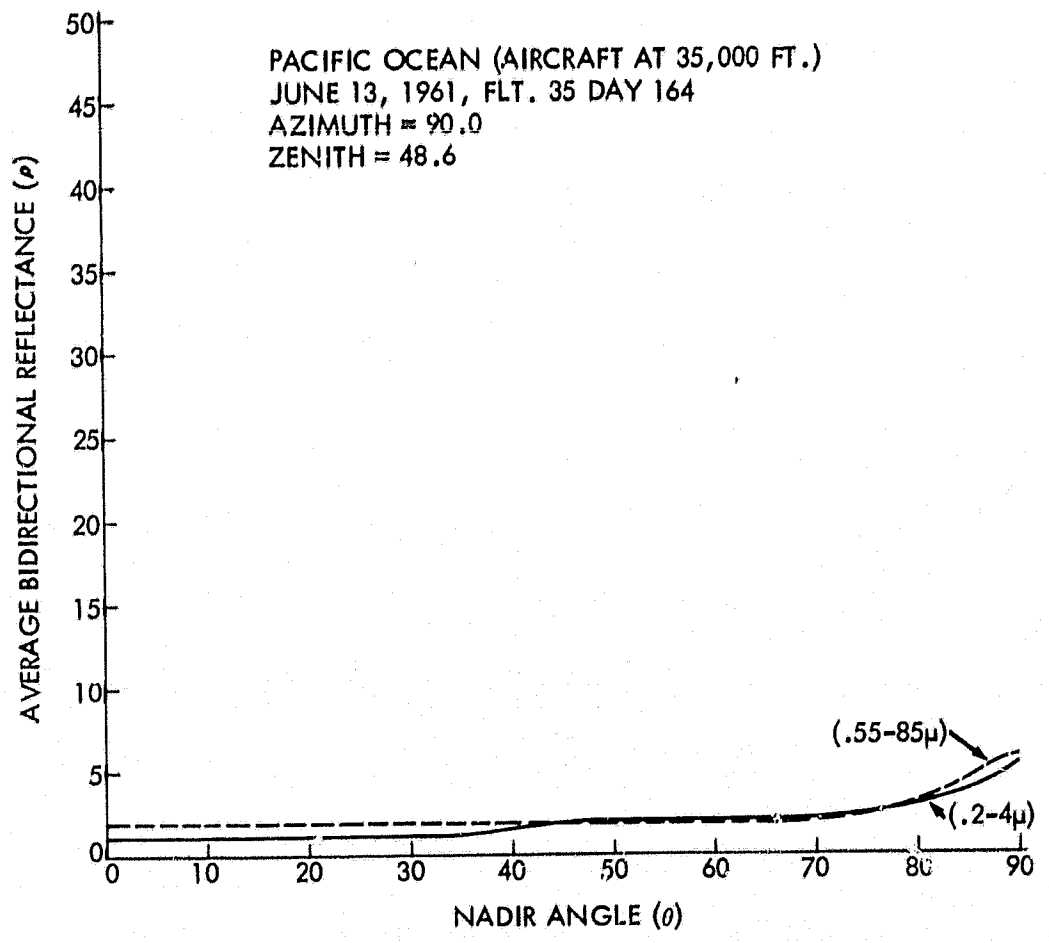

Figure 47–Bidirectional reflectances of the Pacific Ocean at 37° 40′ N 122° 48′ W.

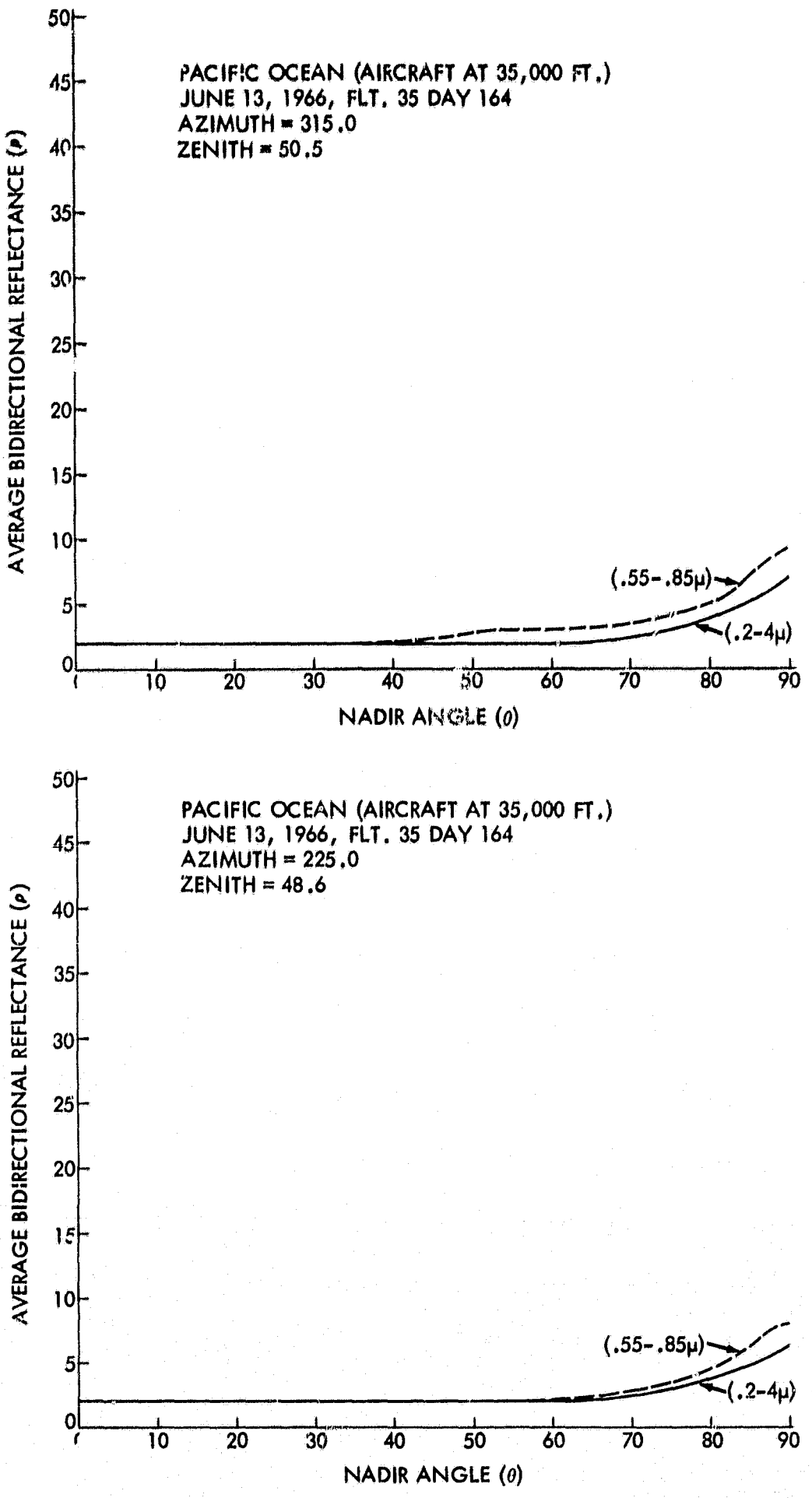

Figure 48–Bidirectional reflectances of the Pacific Ocean at 37° 40′ N 122° 48′ W.

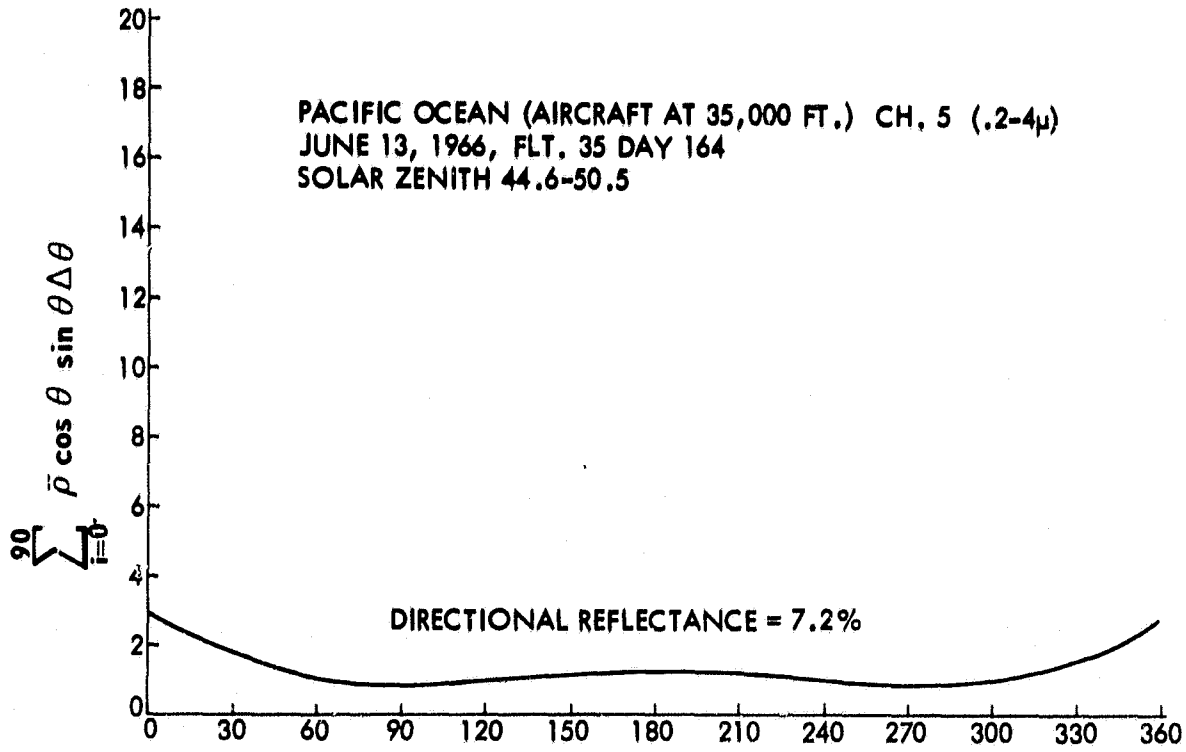

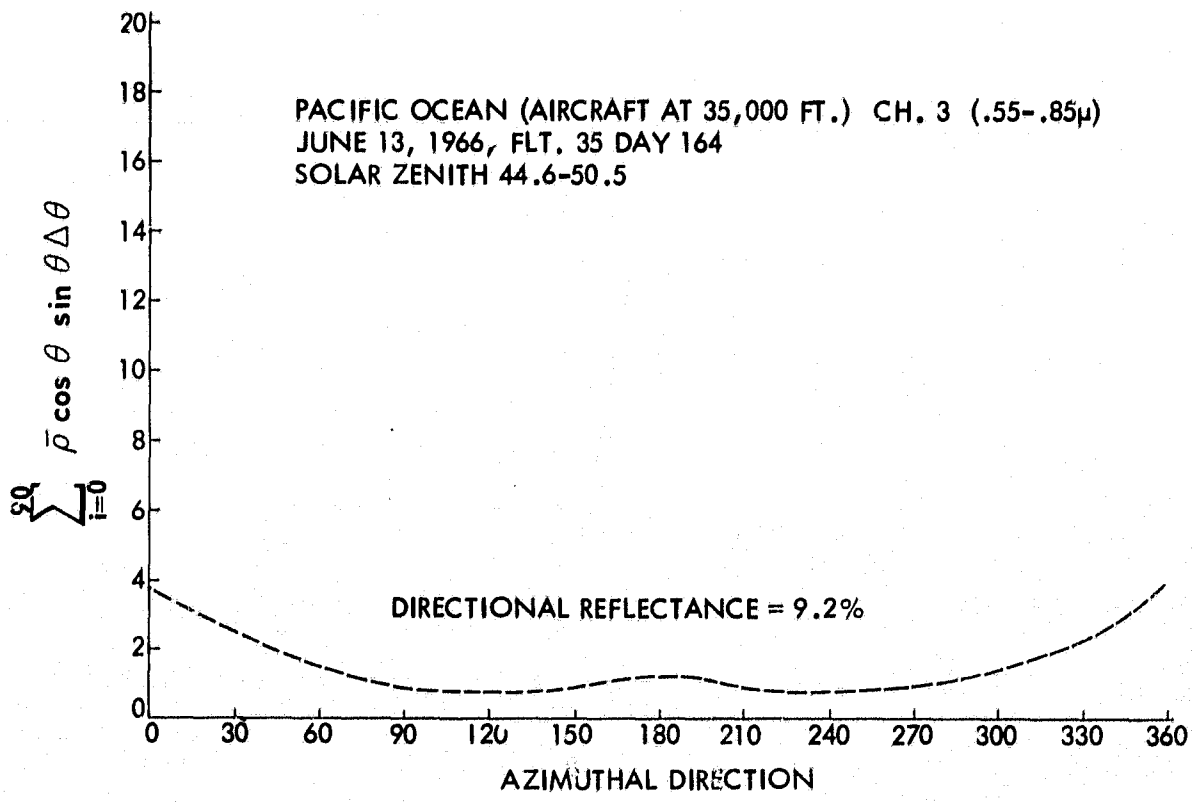

Figure 49–Numerical integration of $\bar{\rho}$ over θ vs. azimuthal direction for the Pacific Ocean at 37° 40′ N 122° 48′ W.

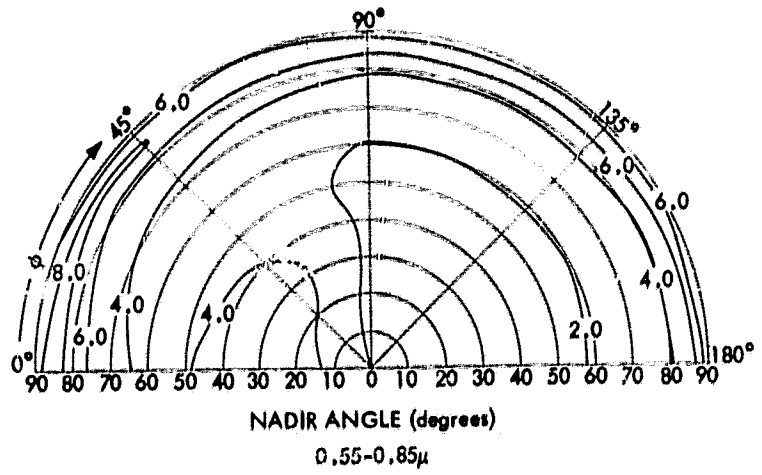

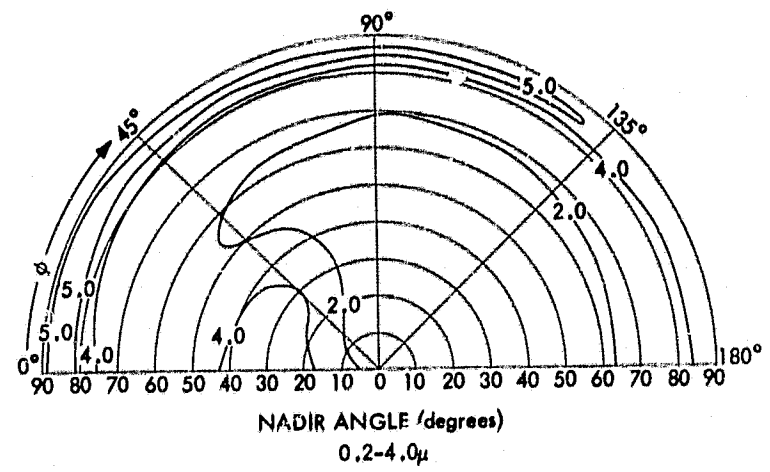

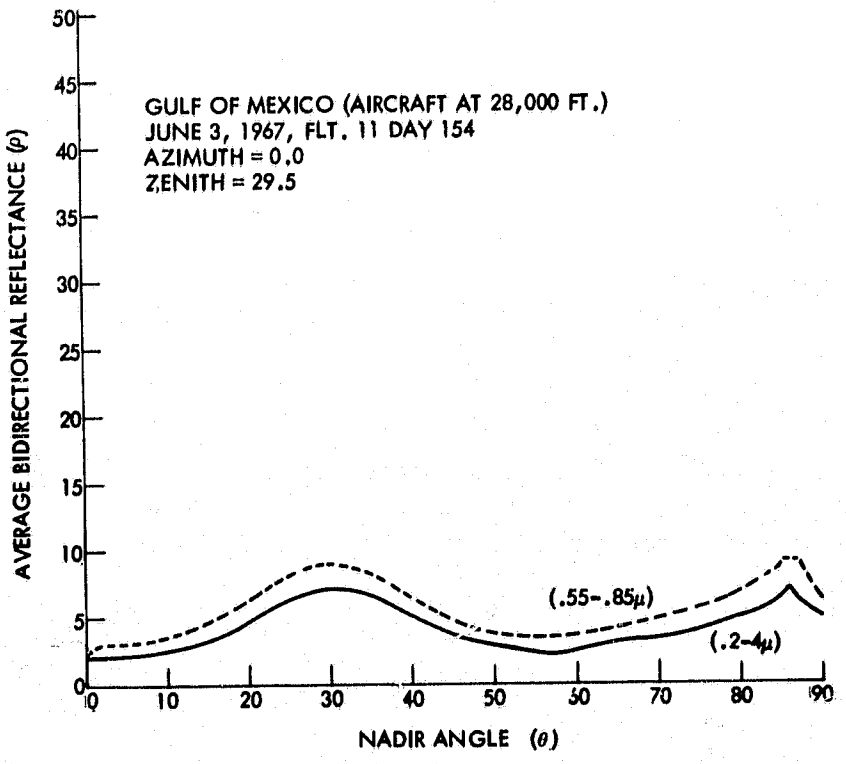

Figure 50–Bidirectional reflectances of the Gulf of Mexico.

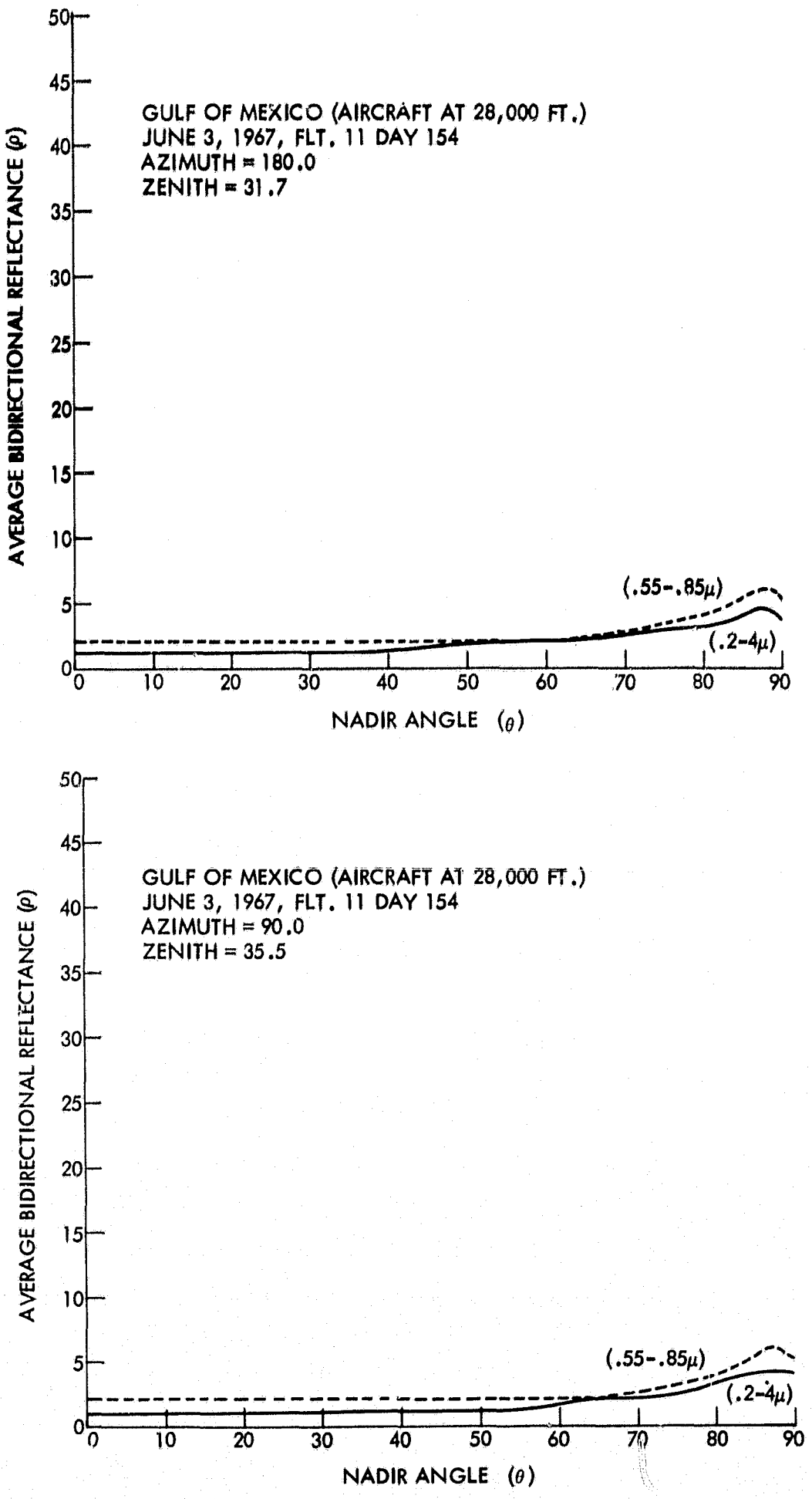

Figure 51–Bidirectional reflectances of the Gulf of Mexico.

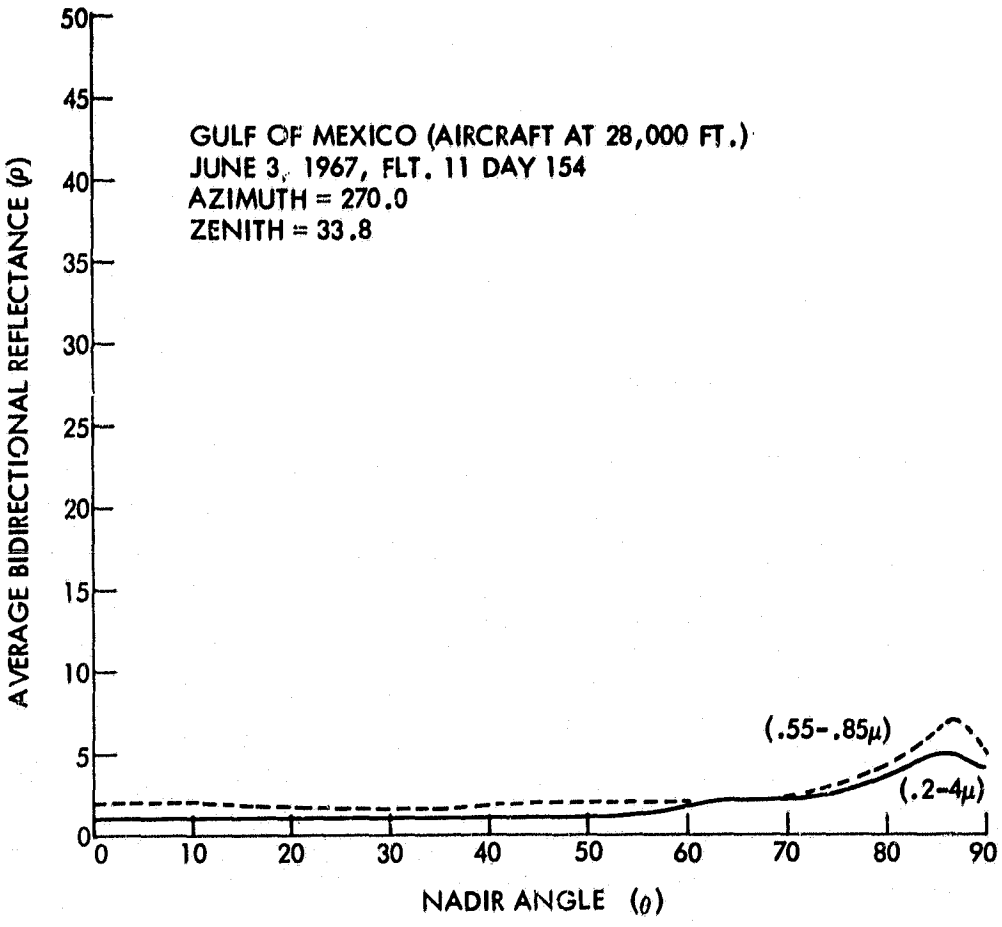

Figure 52–Bidirectional reflectances of the Gulf of Mexico.

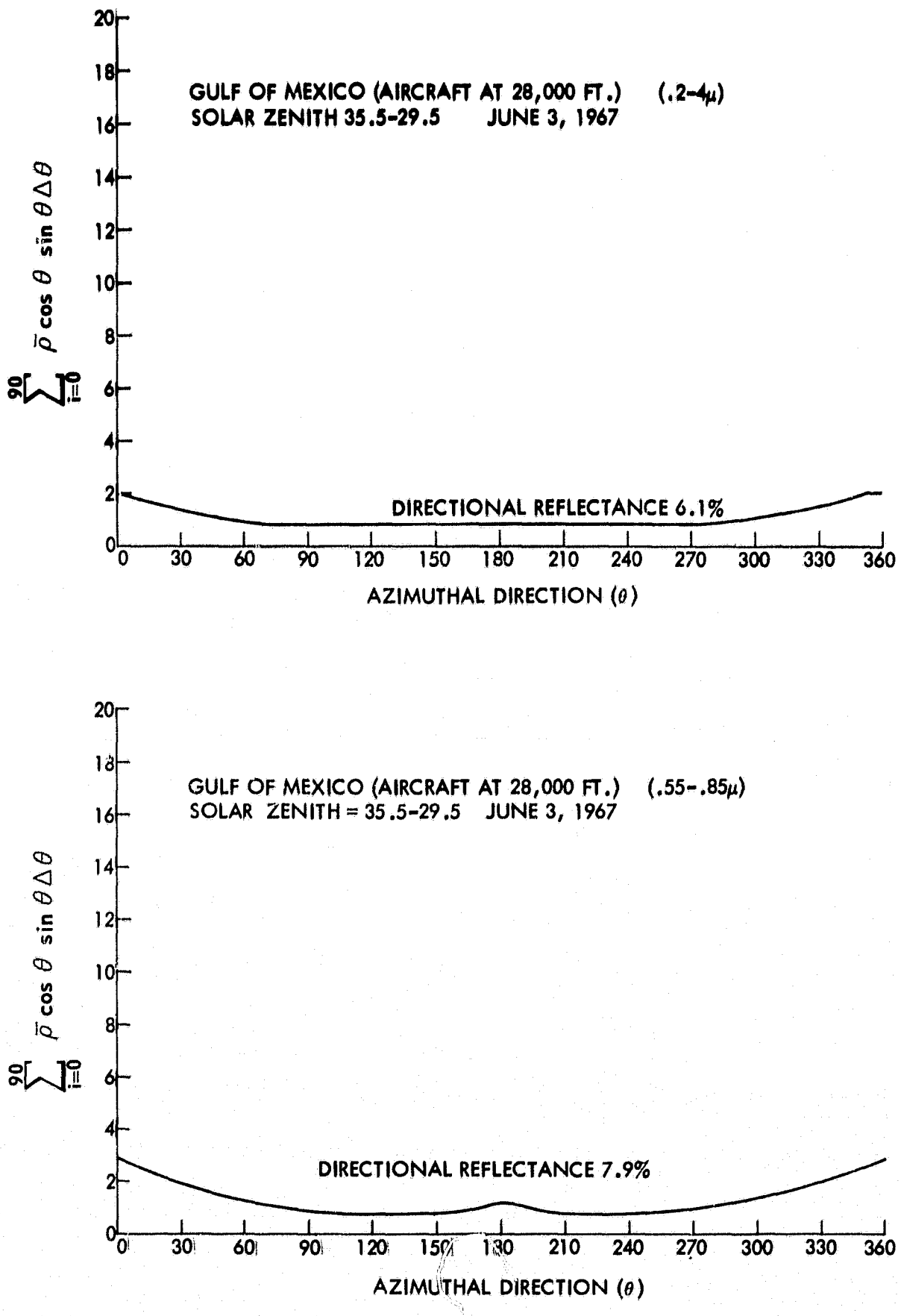

Figure 53–Numerical integration of $\bar{\rho}$ over θ vs. azimuthal direction for the Gulf of Mexico.

TABLE II

Flt. No.	Type of Surface	Surface Alt.	Aircraft Alt.	Range of Solar Zenith Angle (ζ_0) [degrees]	
		10^3 ft.			
1966: 13	Strato Cumulus Over Okeefenokee		40	80.0	85.6
16	Carson Sink	3.9	39	40.7	41.6
32	Salt Lake Desert	4.3	40	21.2	22.5
34	Strato Cumulus Over Pacific Ocean	2.3	2.5	26.8	28.8
34	Strato Cumulus Over Pacific Ocean	2.3	8	30.5	32.5
34	Strato Cumulus Over Pacific Ocean	2,3	16	32.7	33.7
34	Strato Cumulus Over Pacific Ocean	2.3	24	35.8	38.3
34	Strato Cumulus Over Pacific Ocean	2.3	32	39.9	40.8
34	Pacific Ocean		16	70.7	72.6
36	Strato Cumulus Over Pacific Ocean		40	63.9	73.3
37	Pacific Ocean		40	52.3	50.4
39	White Sands	4.0	20	9.6	10.8
41	Pacific Ocean		2.5	25.5	27.2
41	Pacific Ocean		8	22.2	23.8
41	Pacific Ocean		16	18.5	19.6
41	Pacific Ocean		24	15.5	16.1
41	Pacific Ocean		32	15.1	15.2
41	Pacific Ocean		40	22.0	2.32
1967: I	Pacific Ocean	4.5	29	85.9	86.7
I	Pacific Ocean		39	88.2	89.8

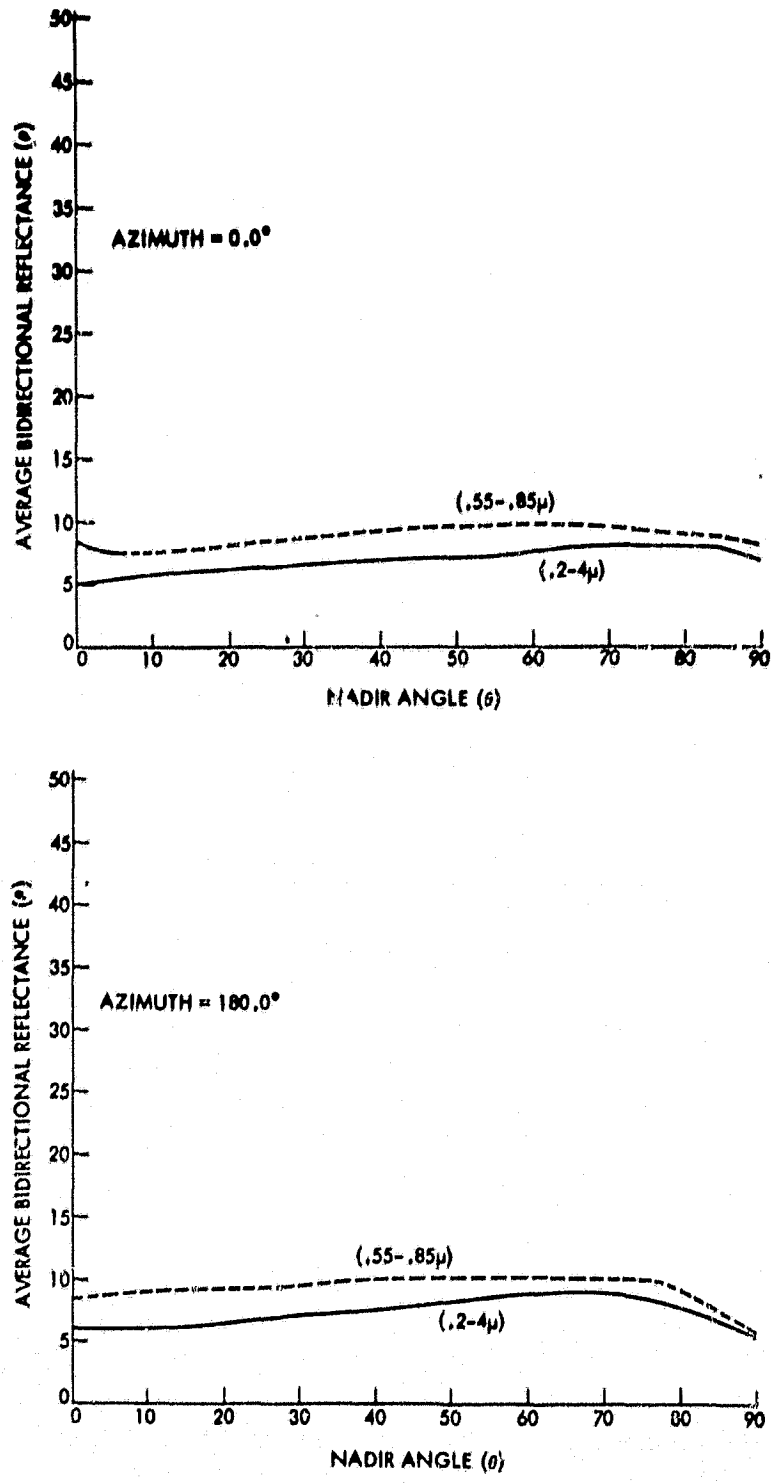

Figure 54–Bidirectional reflectances of carson sink, (aircraft at 39,000 ft) May 13, 1966, Day 133, Flt. 16. Solar Zenith 40.7-41.6°.

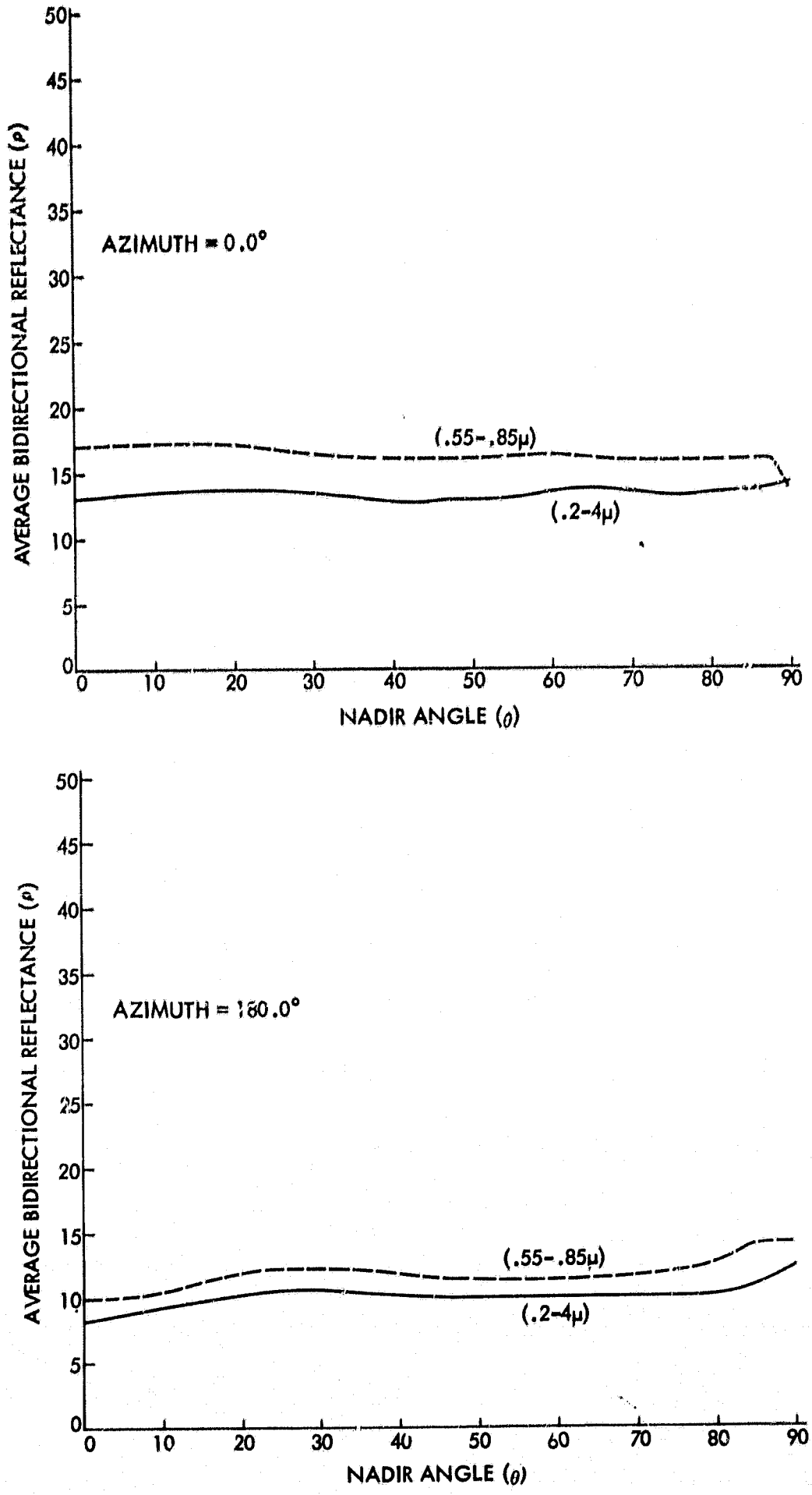

Figure 55–Bidirectional reflectances of Salt Lake Desert, (aircraft at 40,000 ft) June 9, 1966, Day 160, Flt. 32. Solar Zenith 22.5-21.2°.

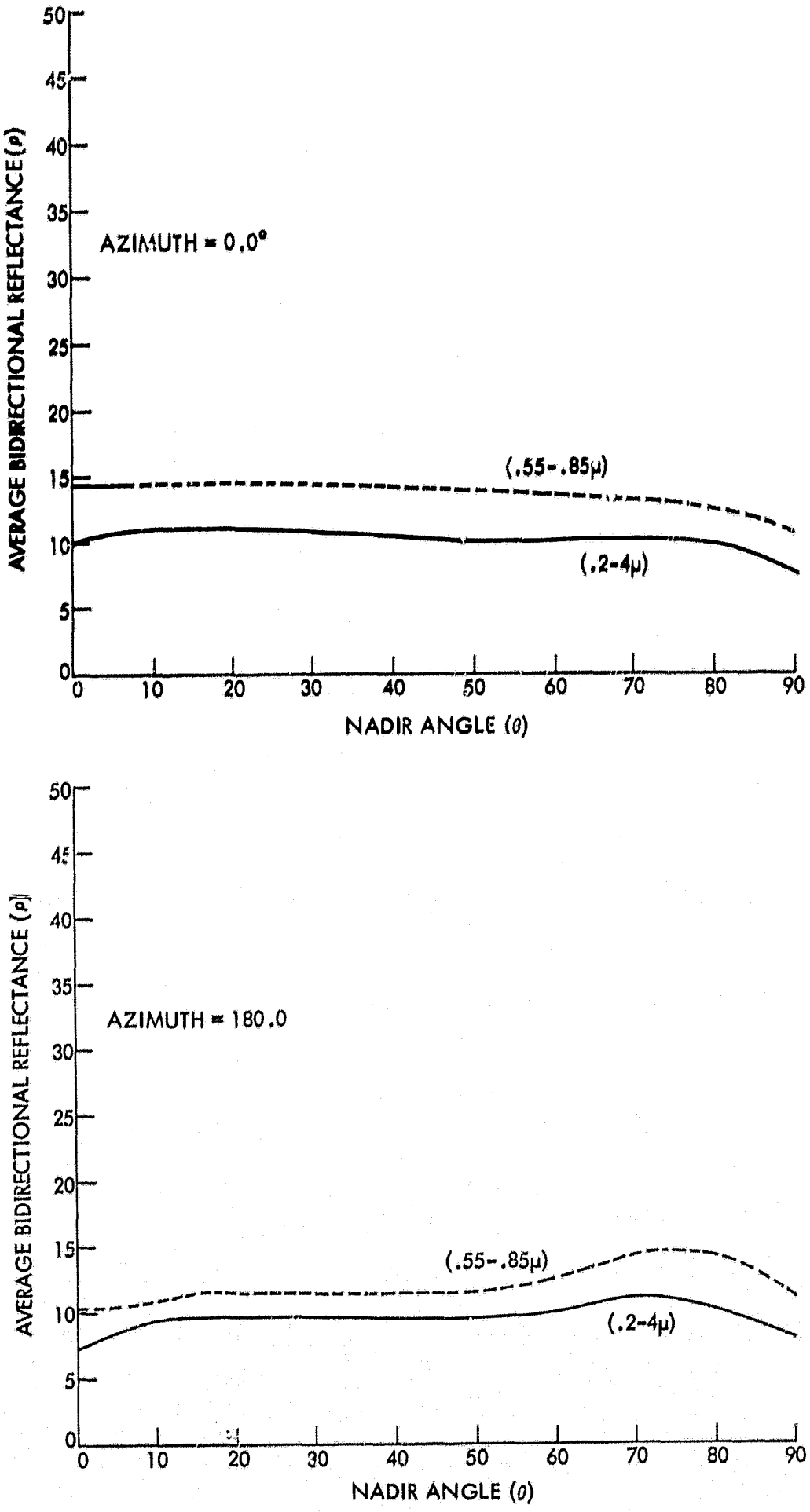

Figure 56–Bidirectional reflectances of White Sand Desert, (aircraft at 20,000 ft), June 16, 1966, Day 167, Flt. 39. Solar Zenith 9.6-10.8°.

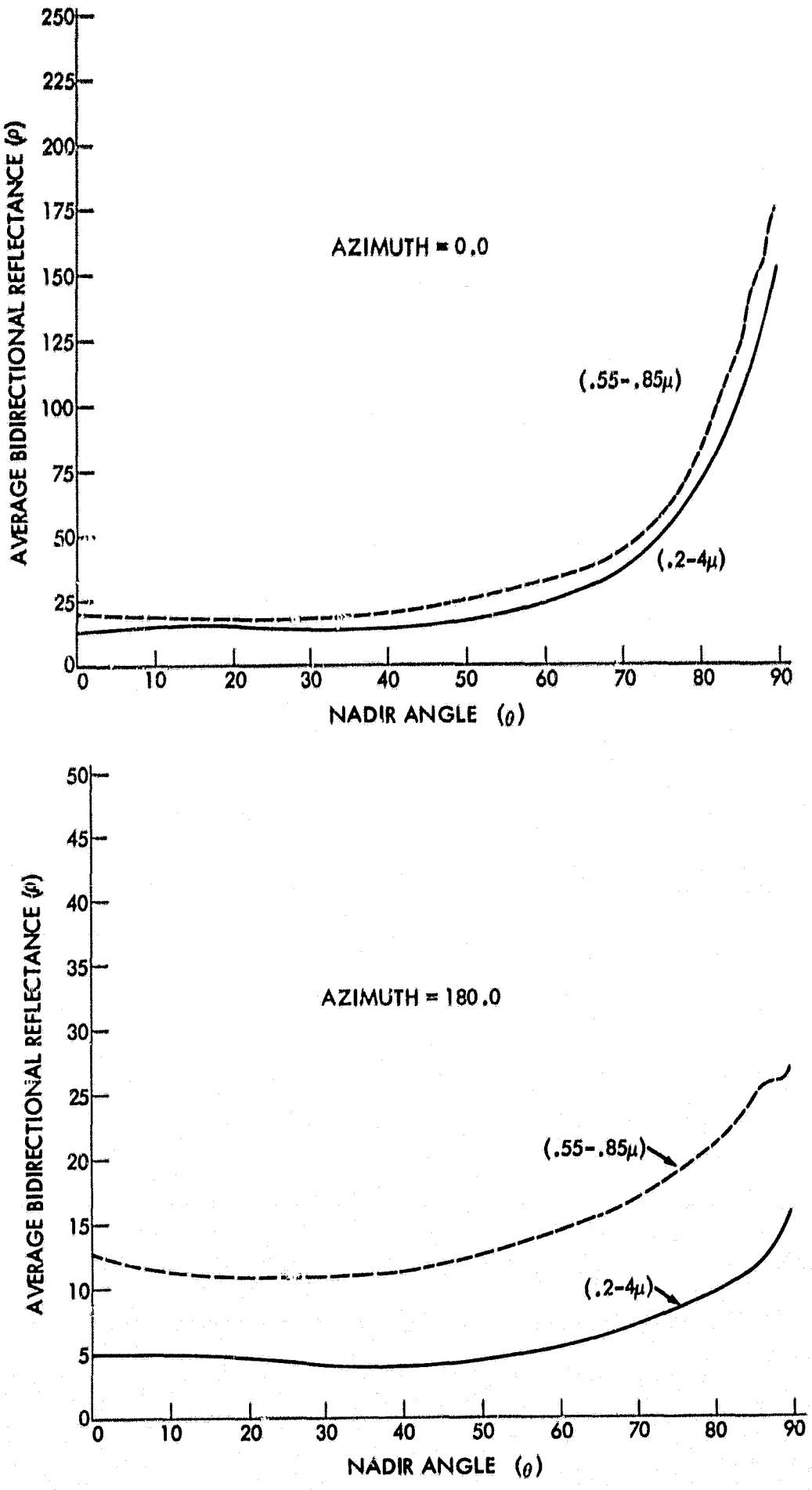

Figure 57–Bidirectional reflectances of Strato Cumulus at 1900 ft. over the Okeefenokee, (aircraft at 40,000 ft) May 10, 1966, Day 131, Flt. 13. Solar Zenith 80.8-85.6°.

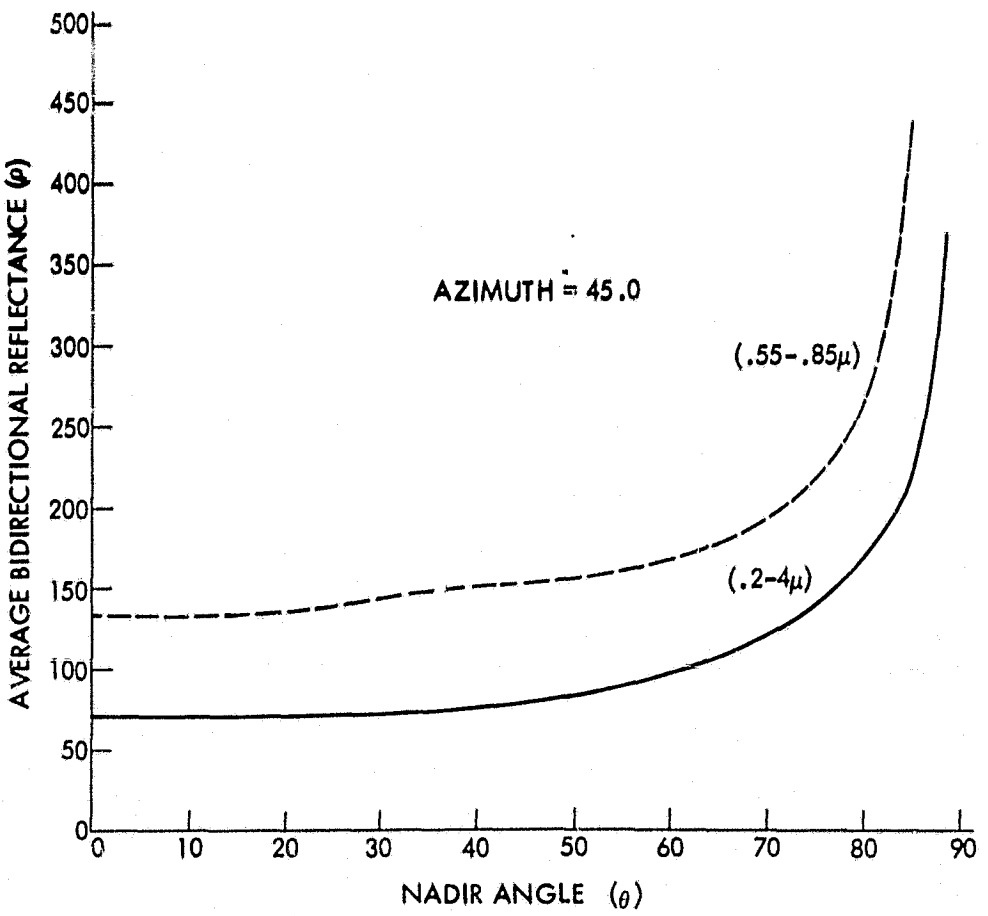

Figure 58–Bidirectional reflectances of Strato Cumulus at 1900 ft. over the Okeefenokee, (aircraft at 40,000 ft) May 10, 1966, Day 131, Flt. 13. Solar Zenith 80.8-85.6°.

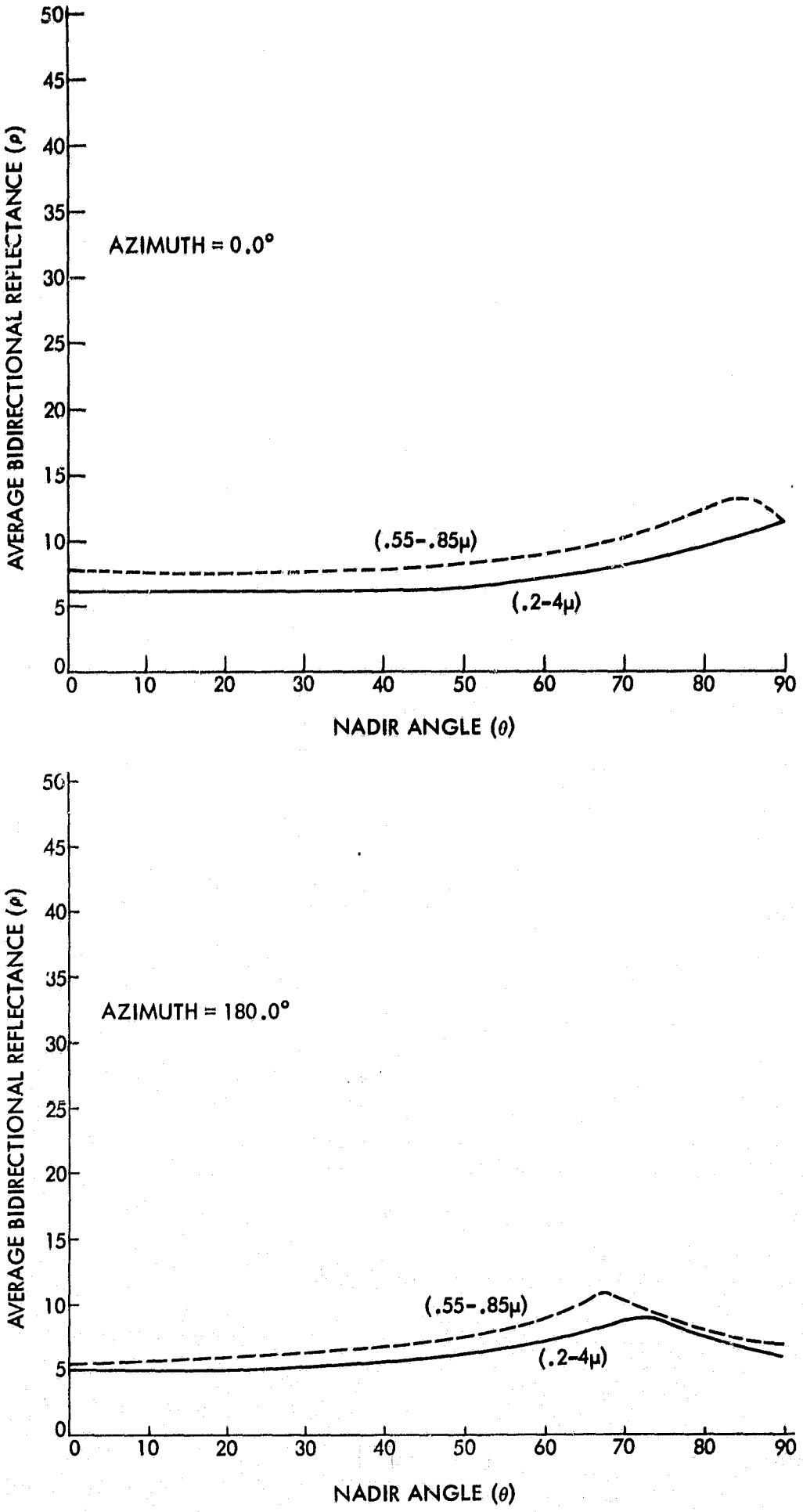

Figure 59–Bidirectional reflectances of Strato Cumulus at 2,300 ft. over Pacific, (aircraft at 2,500 ft) June 10, 1966, Day 161, Flt. 34. Solar Zenith 26.8-28.8°.

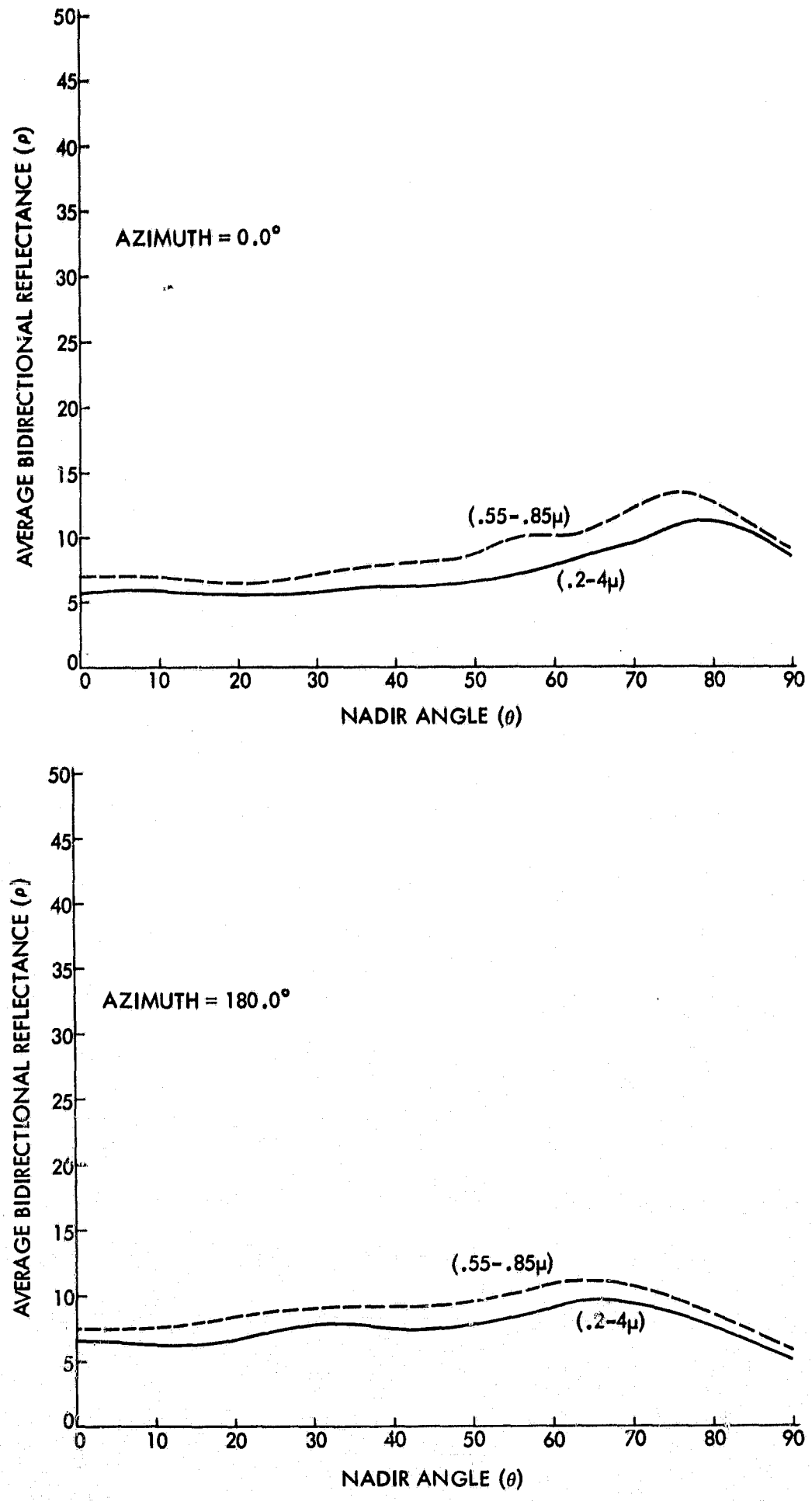

Figure 60–Bidirectional reflectances of Strato Cumulus at 2,300 ft. over Pacific, (aircraft at 8,000 ft) June 10, 1966, Day 161, Flt. 34. Solar Zenith 30.5-32.5°.

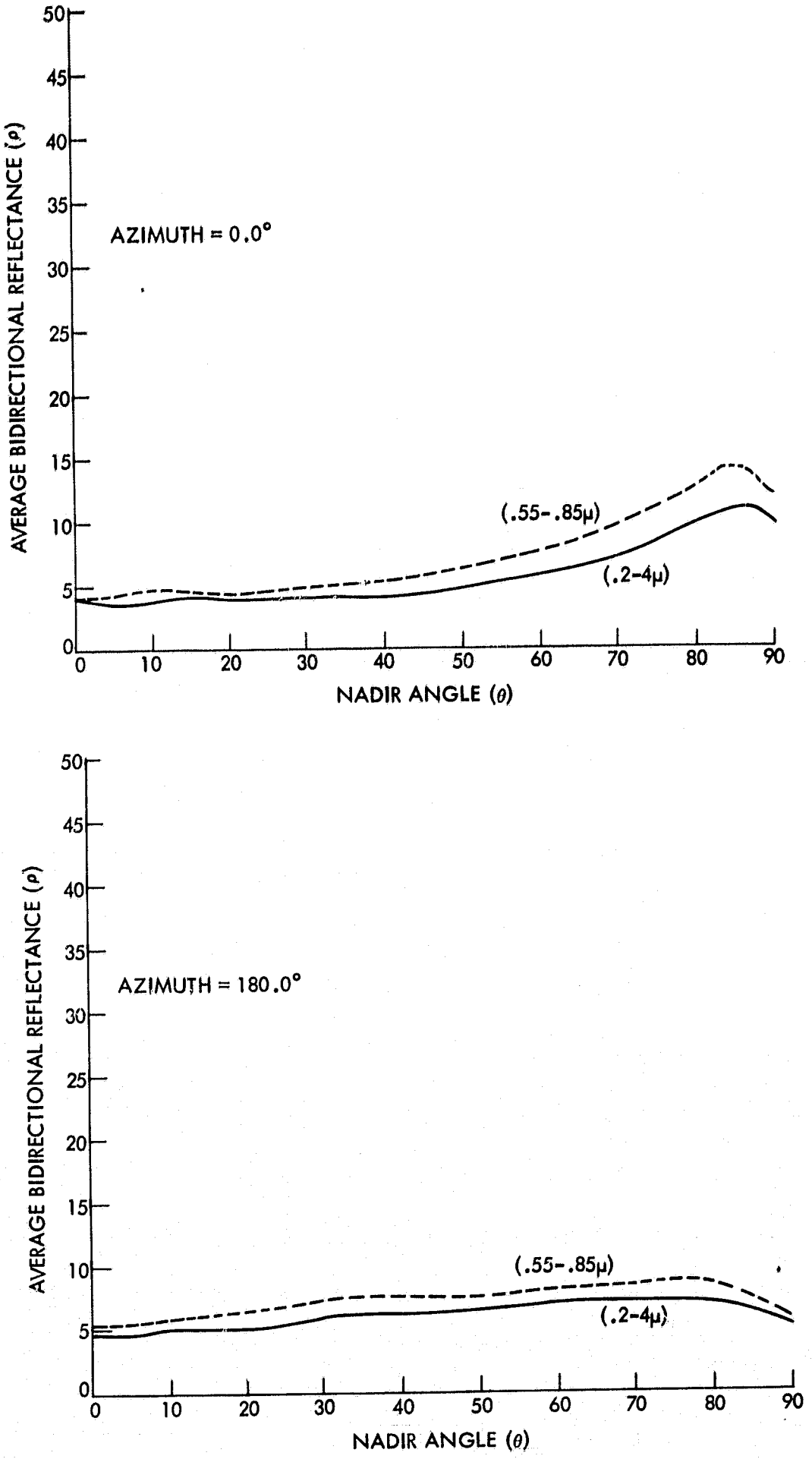

Figure 61–Bidirectional reflectances of Strato Cumulus at 2,300 ft. over Pacific, (aircraft at 16,000 ft) June 10, 1966, Day 161, Flt. 34. Solar Zenith 32.7-33.7°.

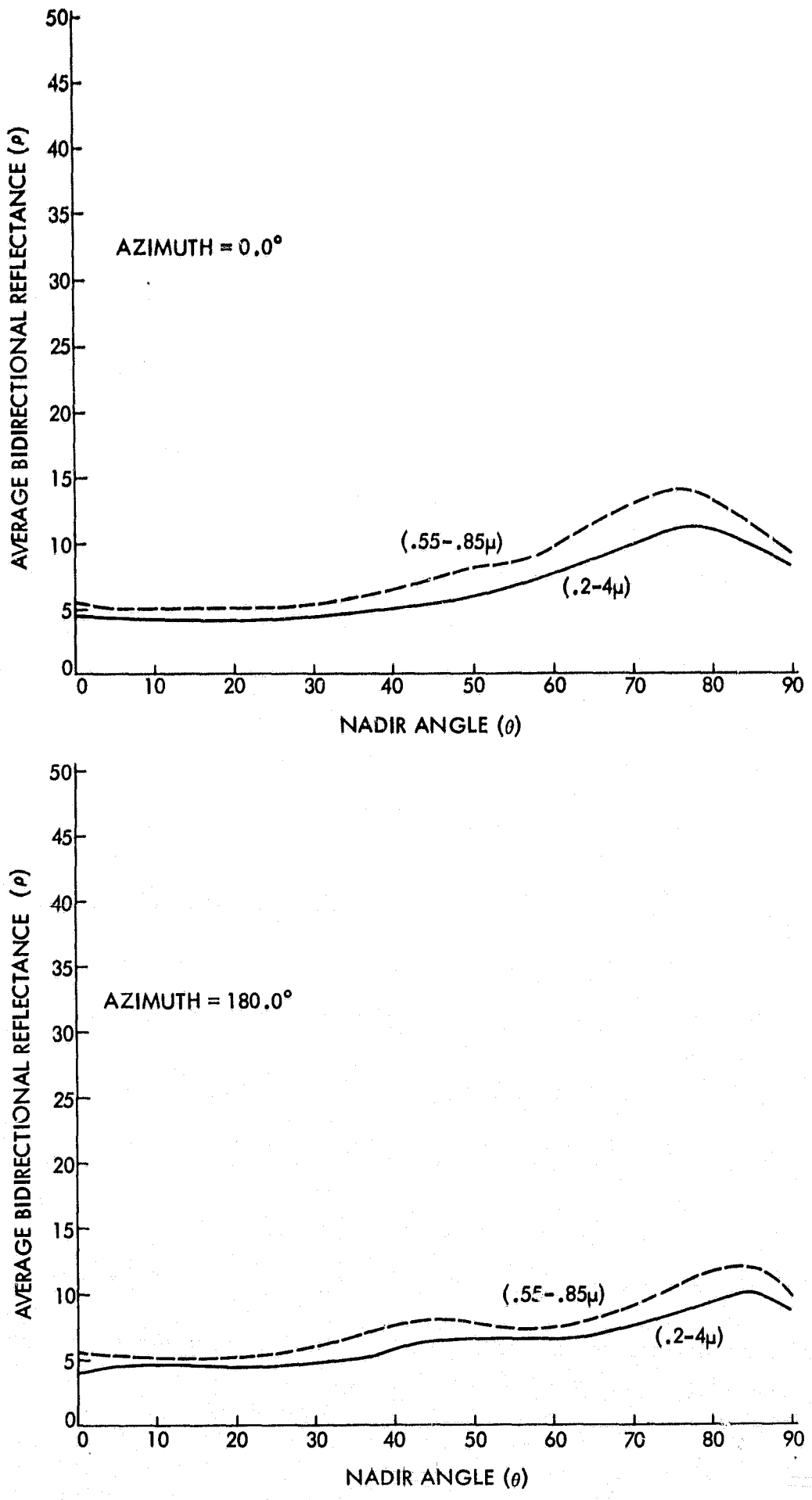

Figure 62–Bidirectional reflectances of Strato Cumulus at 2,300 ft. over Pacific, (aircraft at 24,000 ft) June 10, 1966, Day 161, Flt. 34. Solar Zenith 35.8-38.3°.

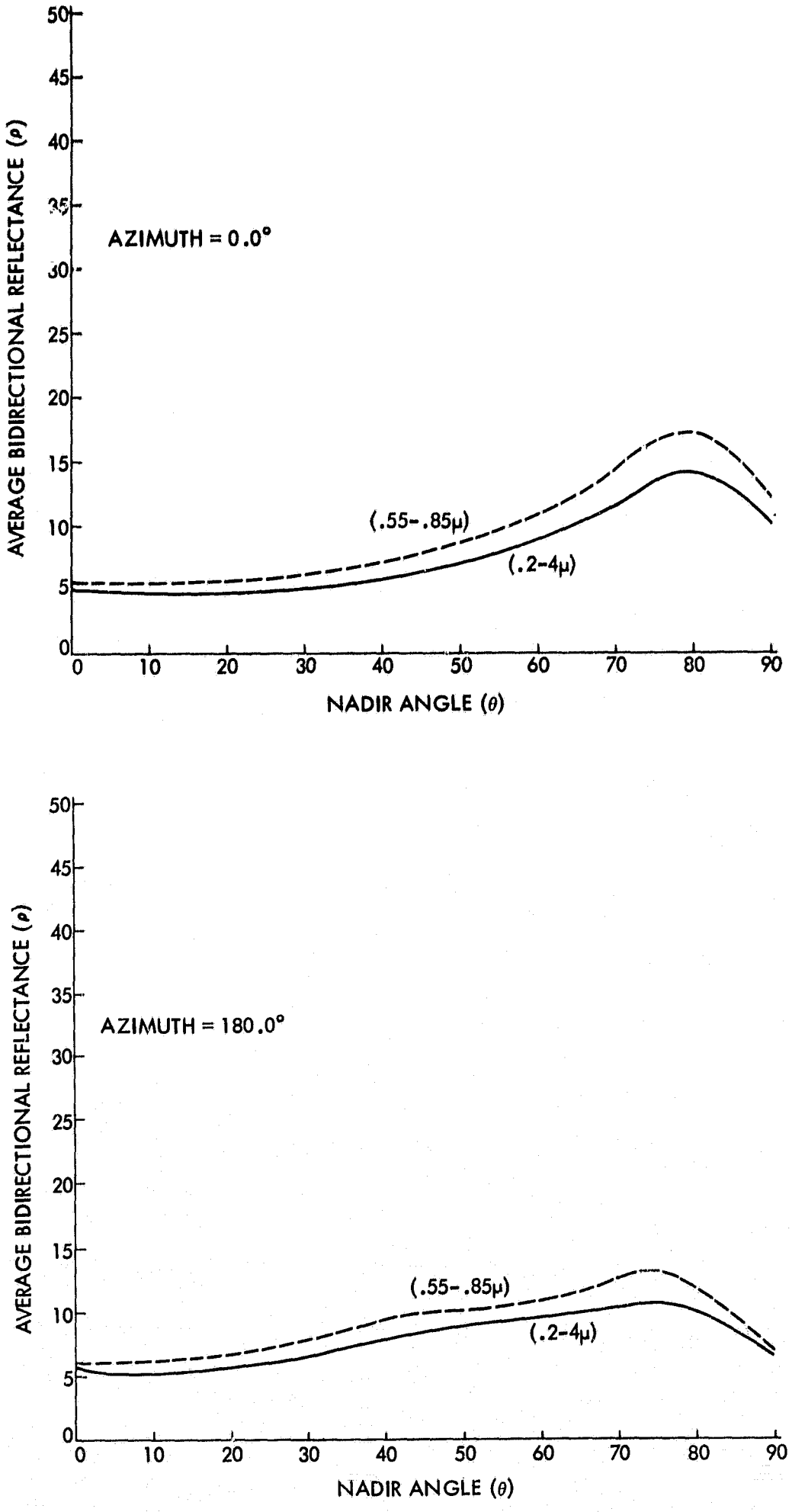

Figure 63–Bidirectional reflectances of Strato Cumulus at 2,300 ft. over Pacific, (aircraft at 32,000 ft) June 10, 1966, Day 161, Flt. 34. Solar Zenith 39.9-40.8°.

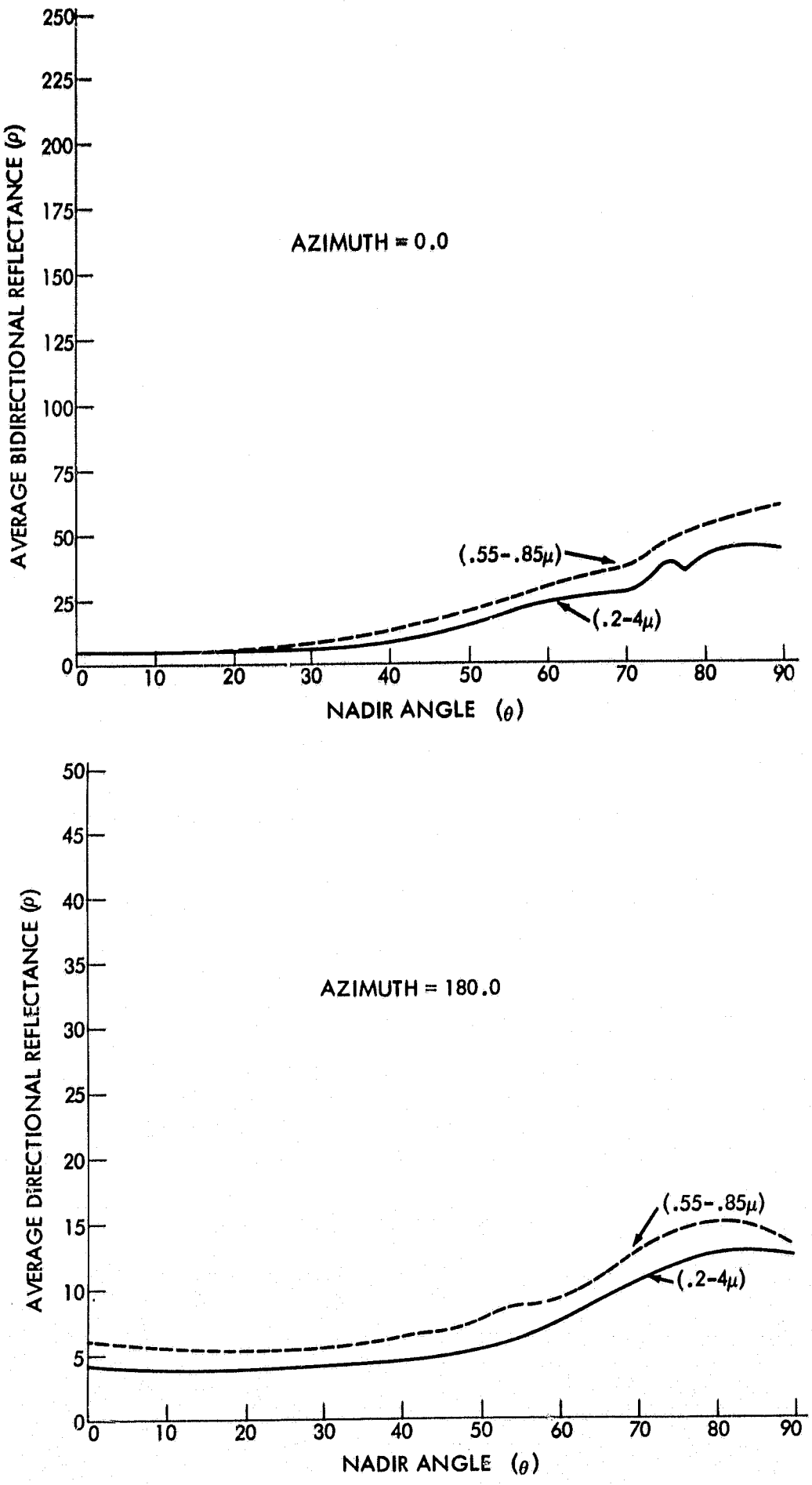

Figure 64–Bidirectional reflectances of Pacific Ocean at 37° 20′ N 122° 25′ W (aircraft at 16,000 ft), June 11, 1966, Day 162, Flt. 34. Solar Zenith 70.7-72.6°.

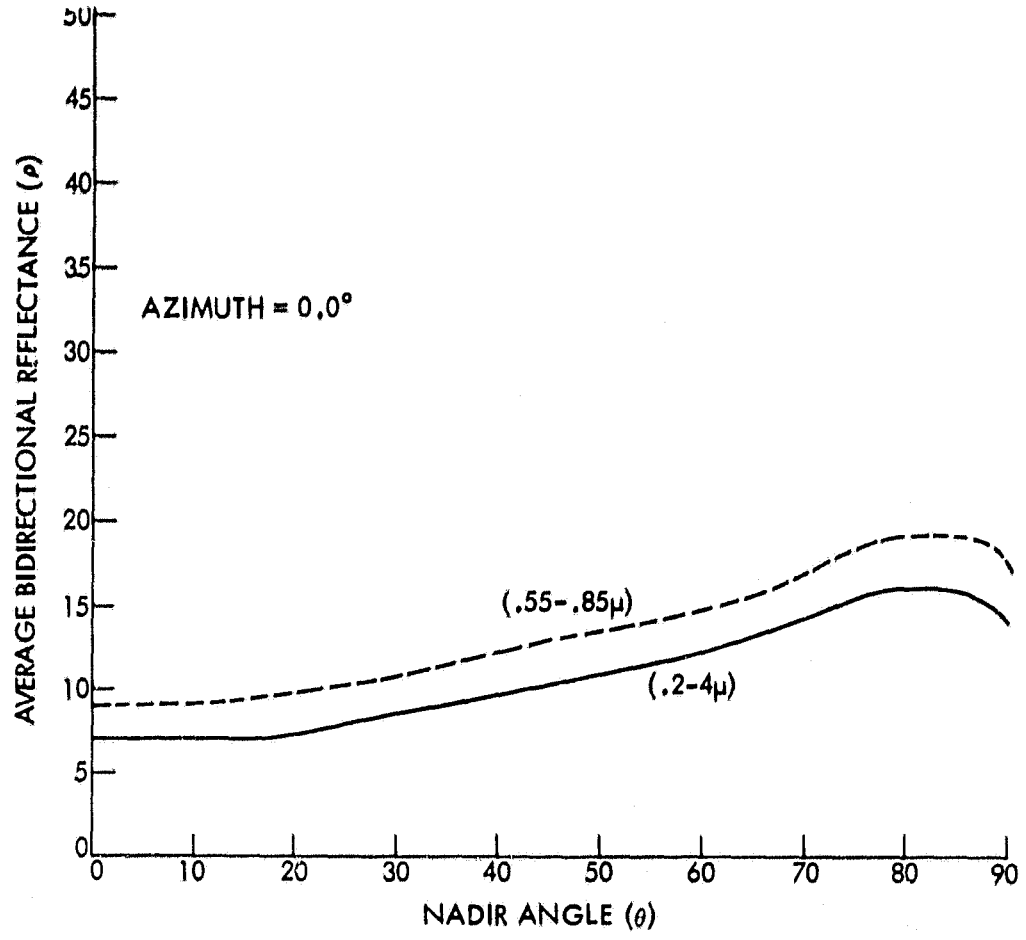

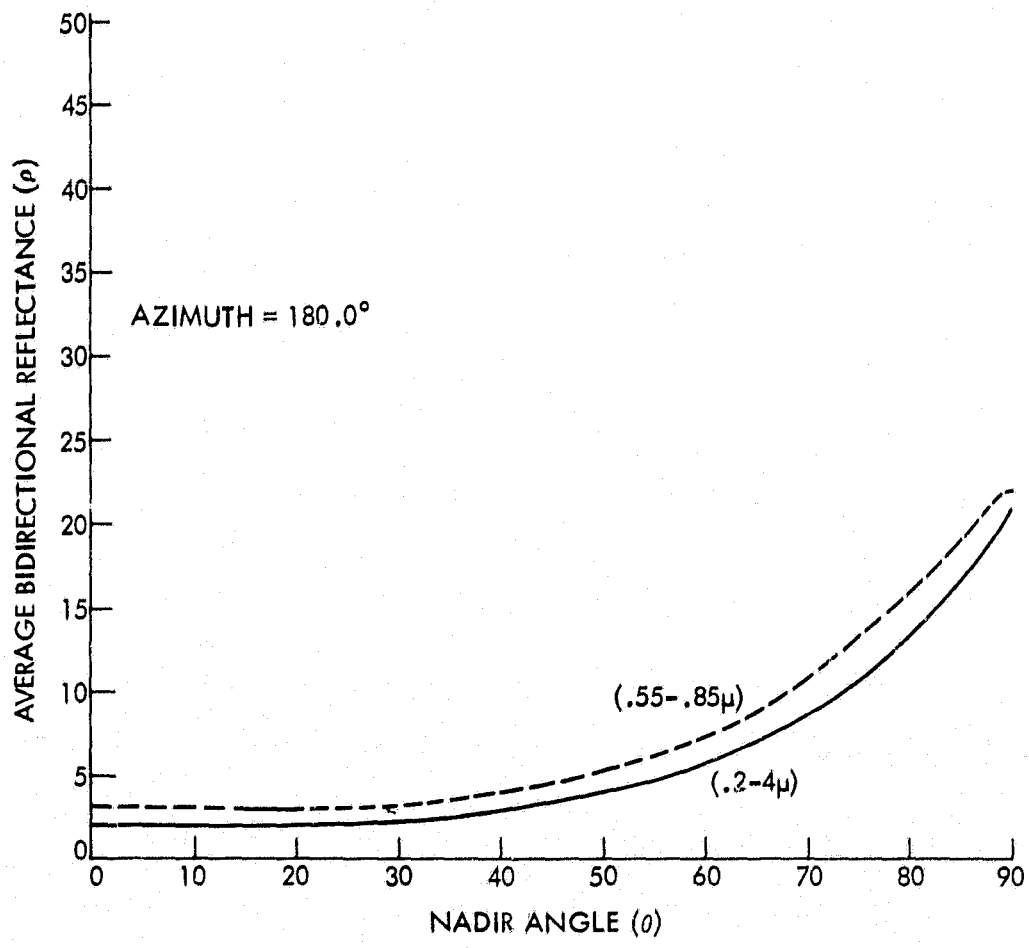

Figure 65–Bidirectional reflectances of Strato Cumulus over Pacific Ocean (aircraft at 40,000 ft.), June 15, 1966, Day 166, Flt. 36. Solar Zenith 63.9-73.3°.

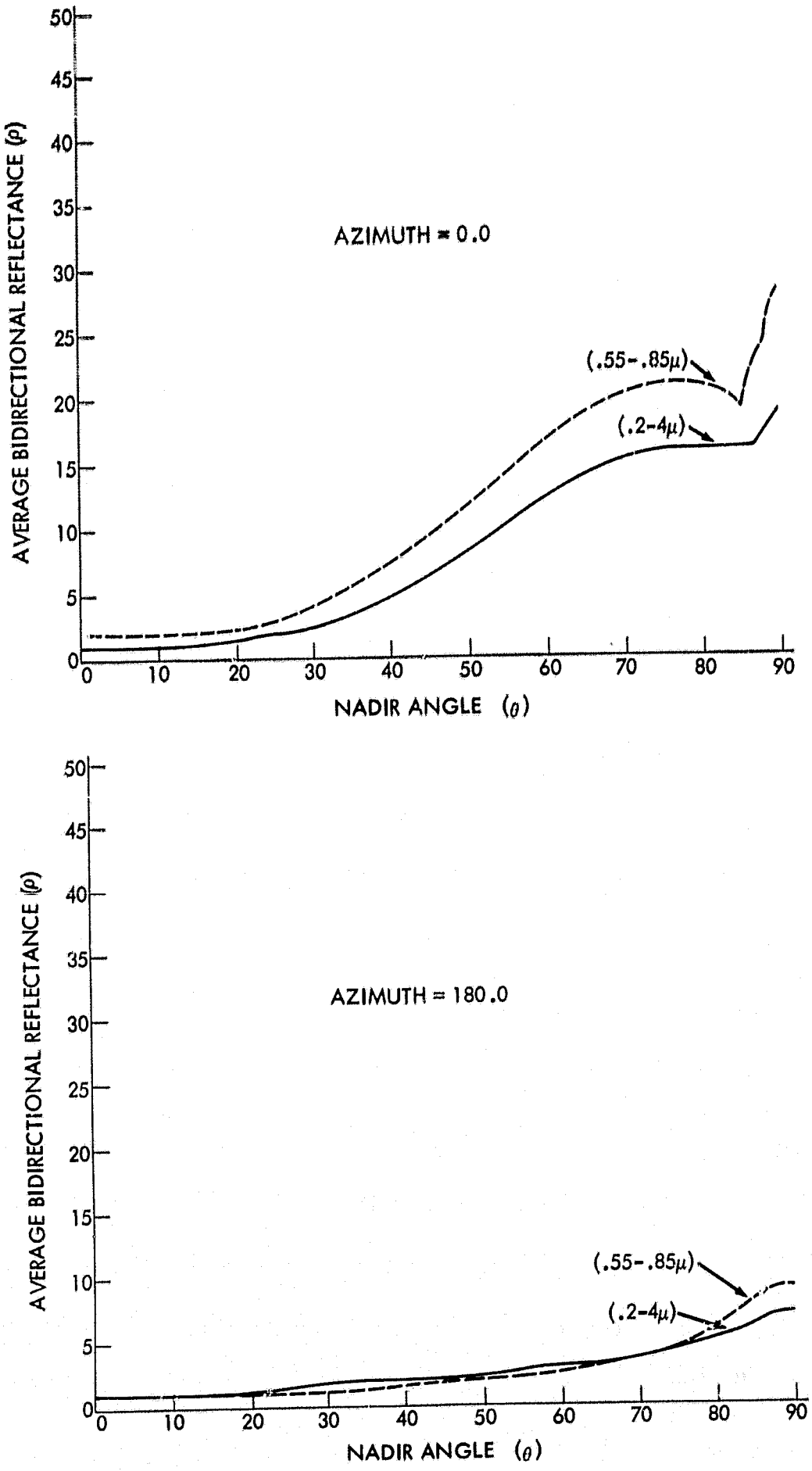

Figure 66–Bidirectional reflectances of Pacific Ocean at 39° N 127° W (aircraft at 40,000 ft.), June 15, 1966, Day 166, Flt. 37. Solar Zenith 52.3-50.4°.

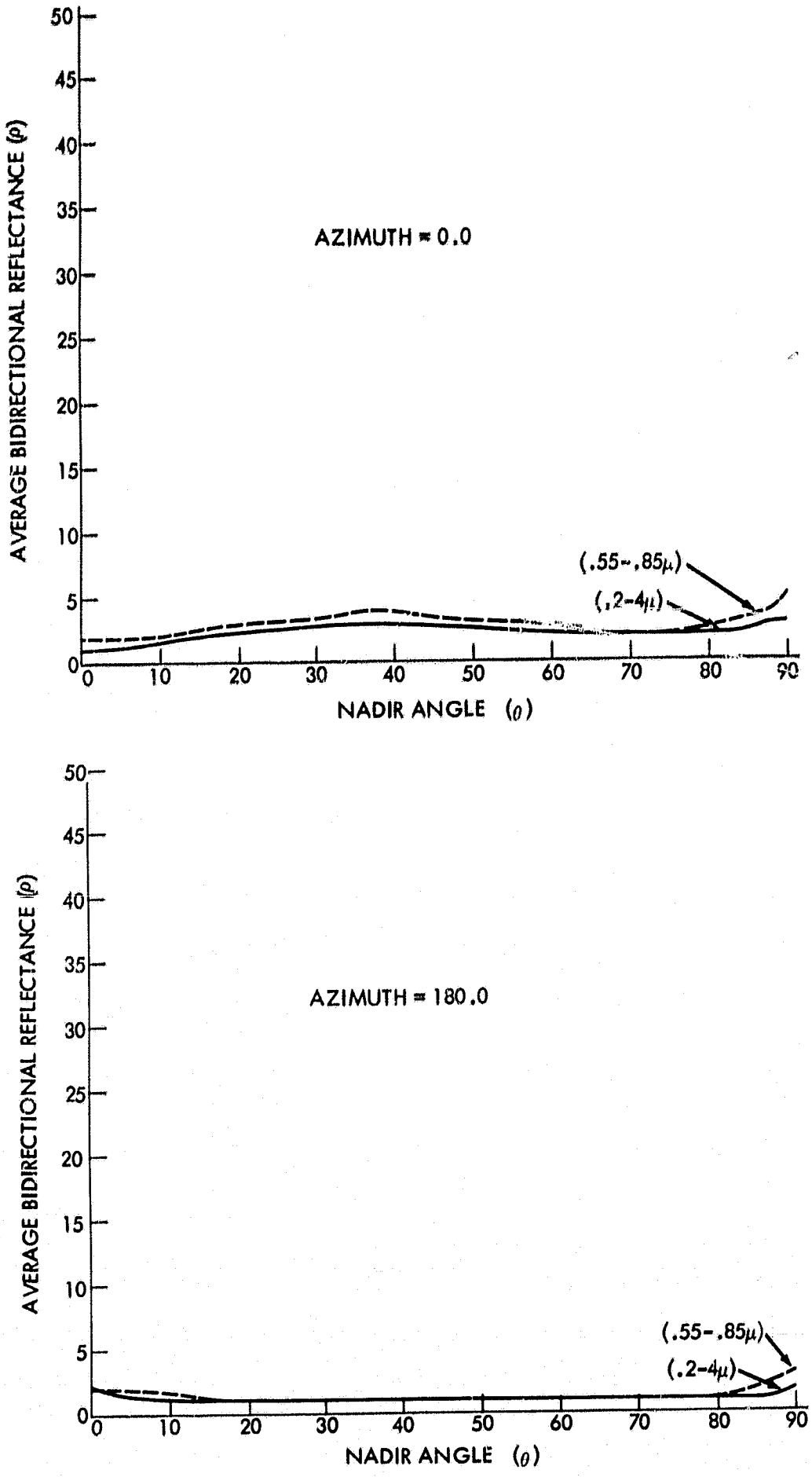

Figure 67–Bidirectional reflectances of Pacific Ocean at 38° 30′ N 126° 30′ W (aircraft at 2,500 ft), June 17, 1966, Day 168, Flt. 41. Solar Zenith 25.5-27.2

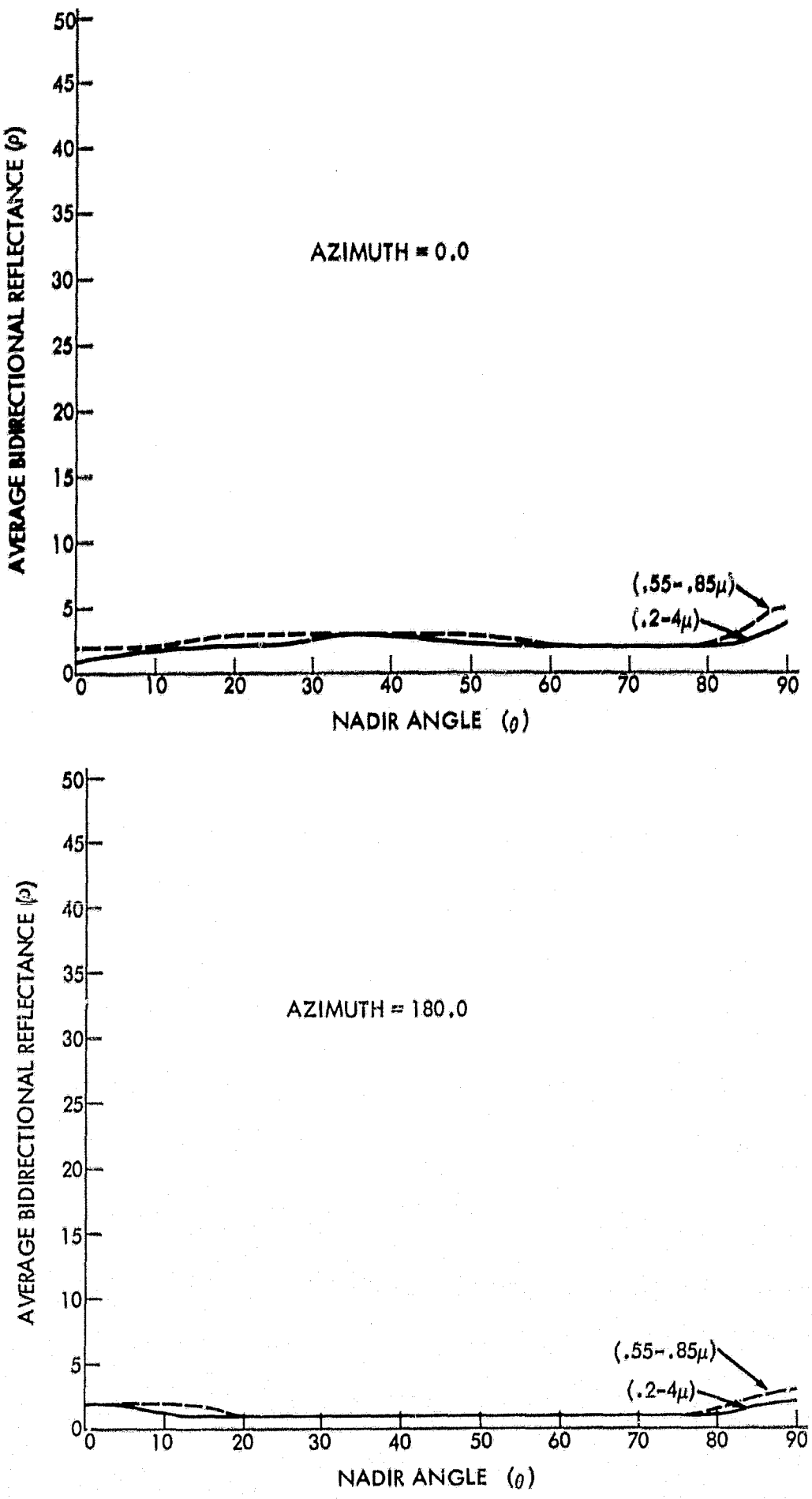

Figure 68–Bidirectional reflectances of Pacific Ocean at 38° 30′ N 126° 30′ W (aircraft at 8,000 ft), June 17, 1966, Day 168, Flt. 41. Solar Zenith 22.2-23.8°.

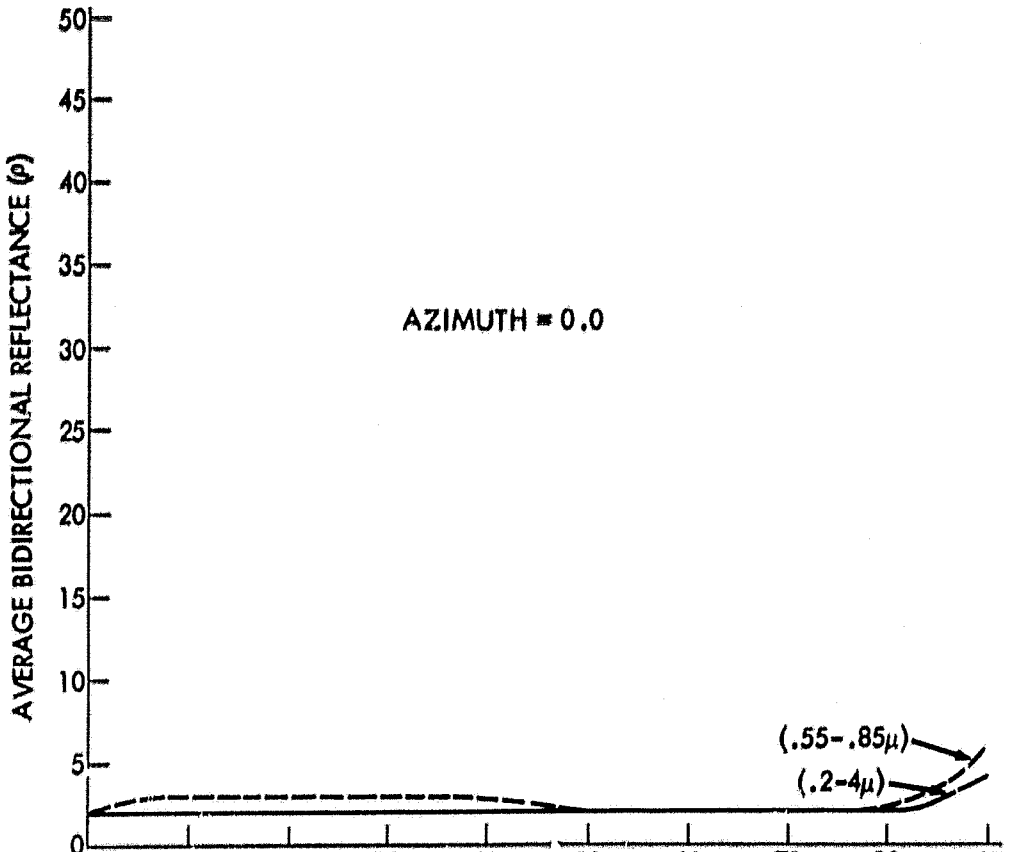

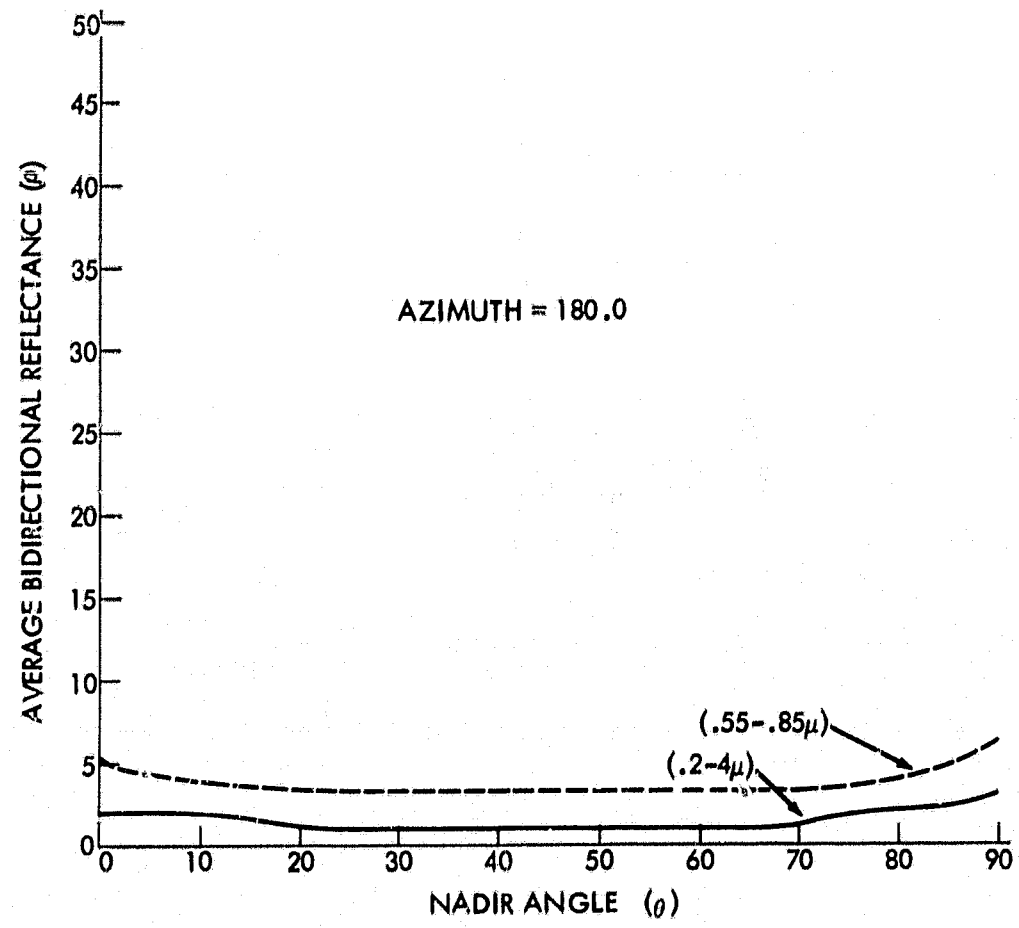

Figure 69–Bidirectional reflectances of Pacific Ocean at 38° 30′ N 126° 30′ W (aircraft at 16,000 ft), June 17, 1966, Day 168, Flt. 41. Solar Zenith 18.5-19.6°.

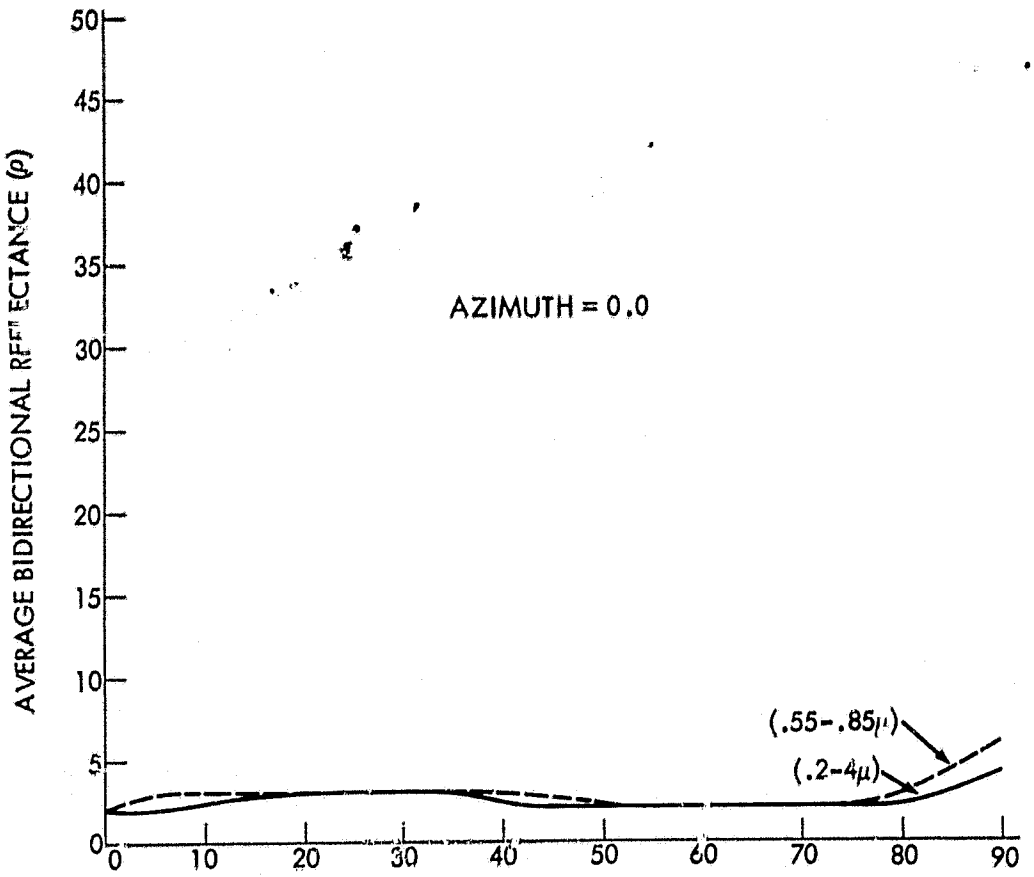

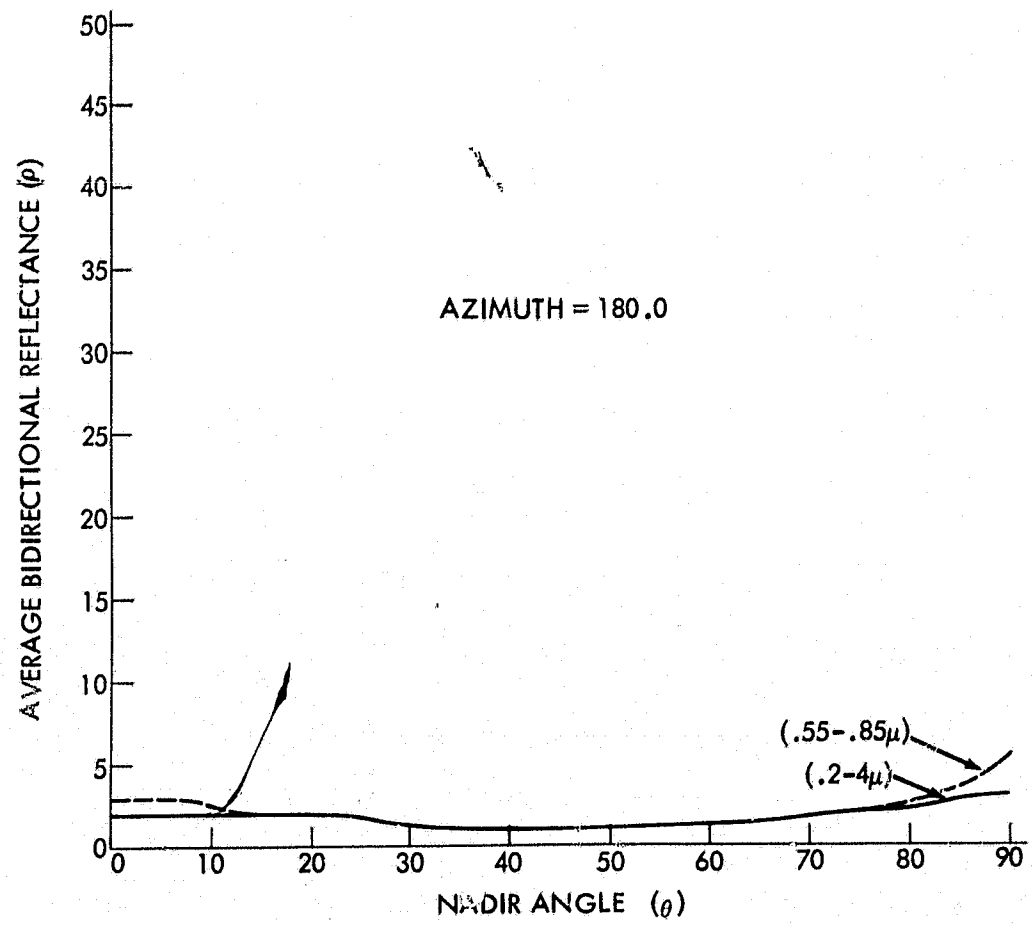

Figure 70–Bidirectional reflectances of Pacific Ocean at 38° 30′ N 126° 30′ W (aircraft at 24,000 ft), June 17, 1966, Day 168, Flt. 41. Solar Zenith 15.5-16.1°.

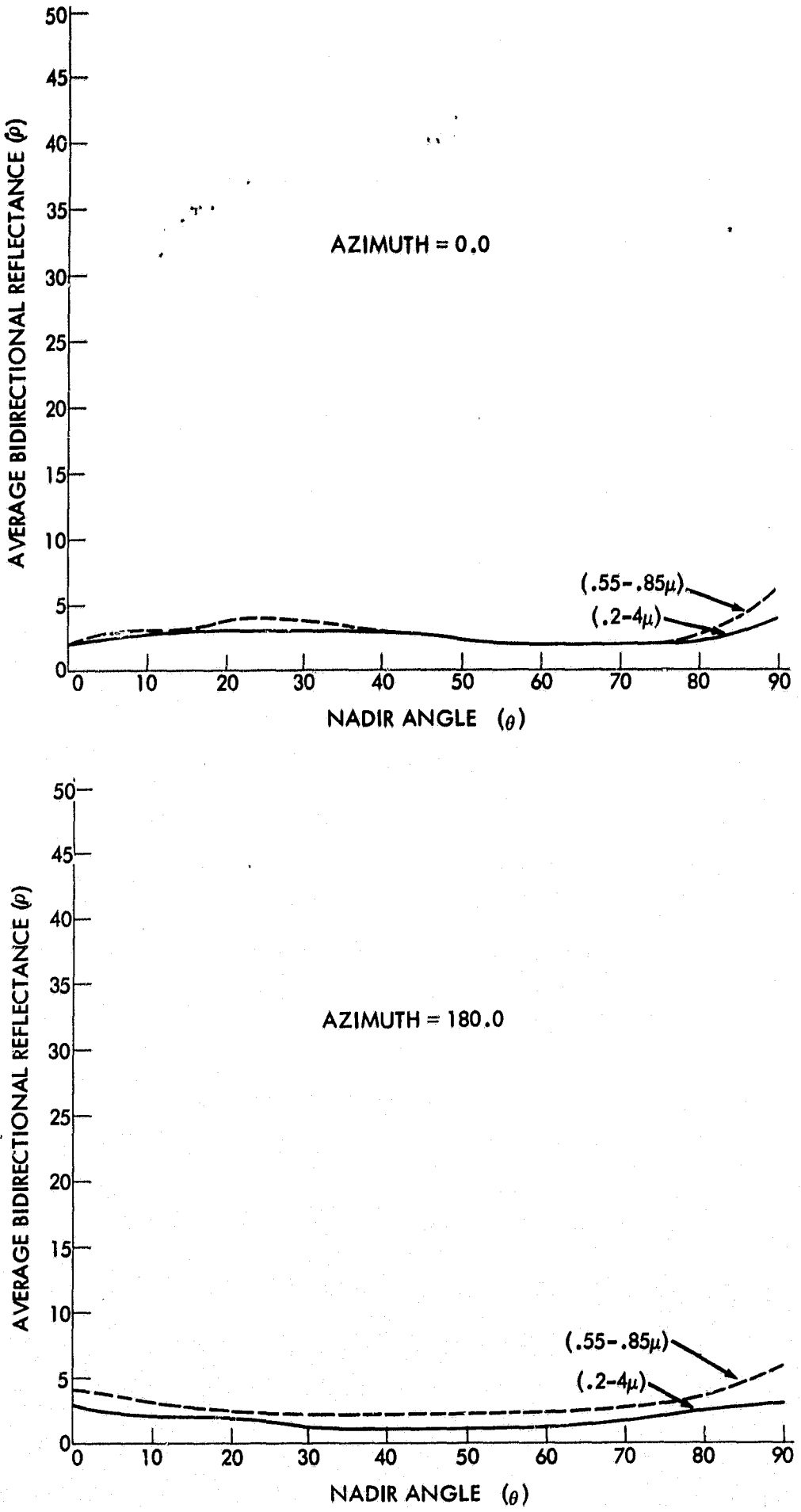

Figure 71–Bidirectional reflectances of Pacific Ocean at 38° 30′ N 126° 30′ W (aircraft at 32,000 ft), June 17, 1966, Day 168, Flt. 41. Solar Zenith 15.1-15.2°.

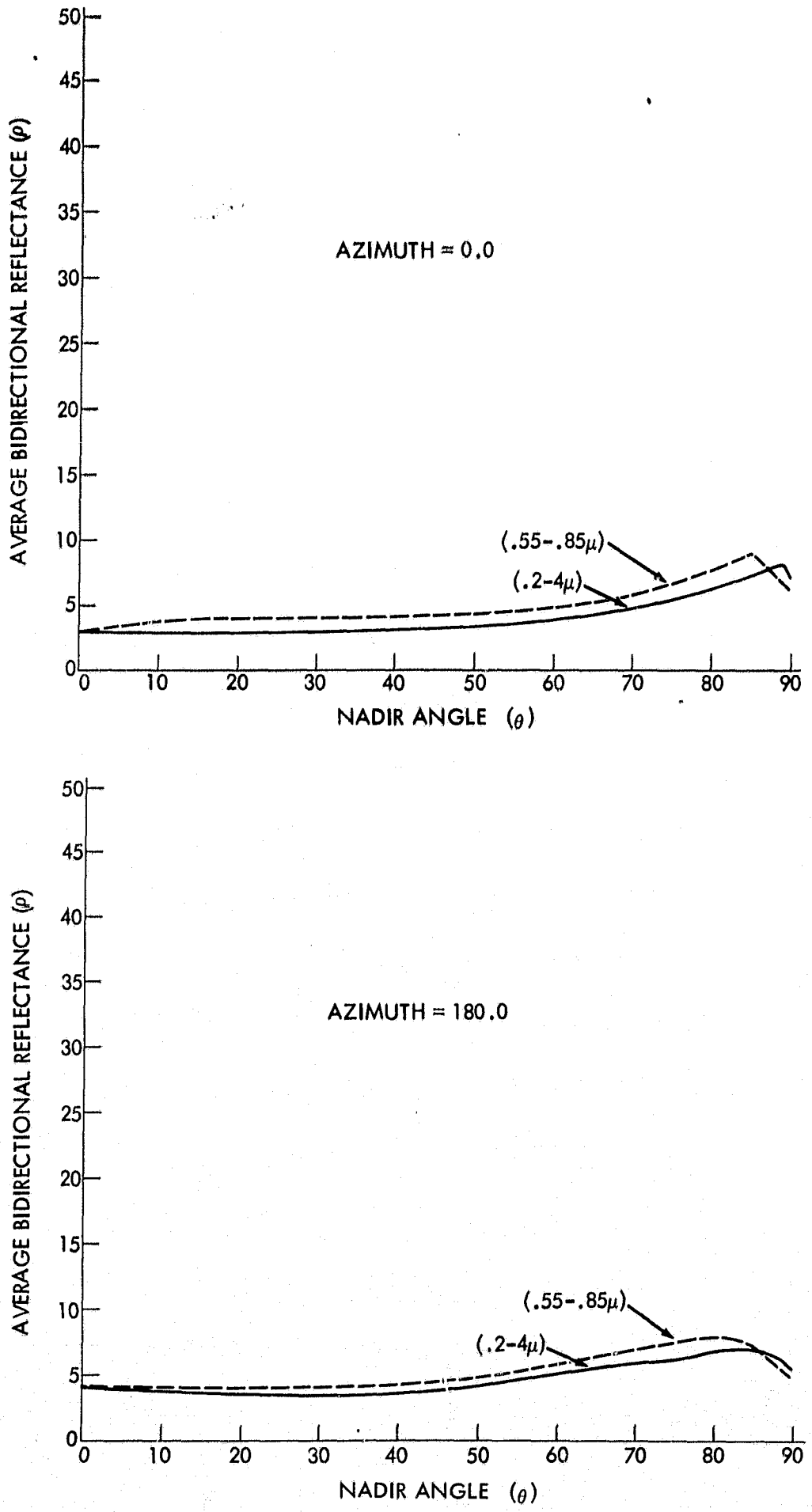

Figure 72–Bidirectional reflectances of Pacific Ocean at 38° 30′ W 126° 30′ W (aircraft at 40,000 ft), June 17, 1966, Day 168, Flt. 41. Solar Zenith 22.0-23.2°.

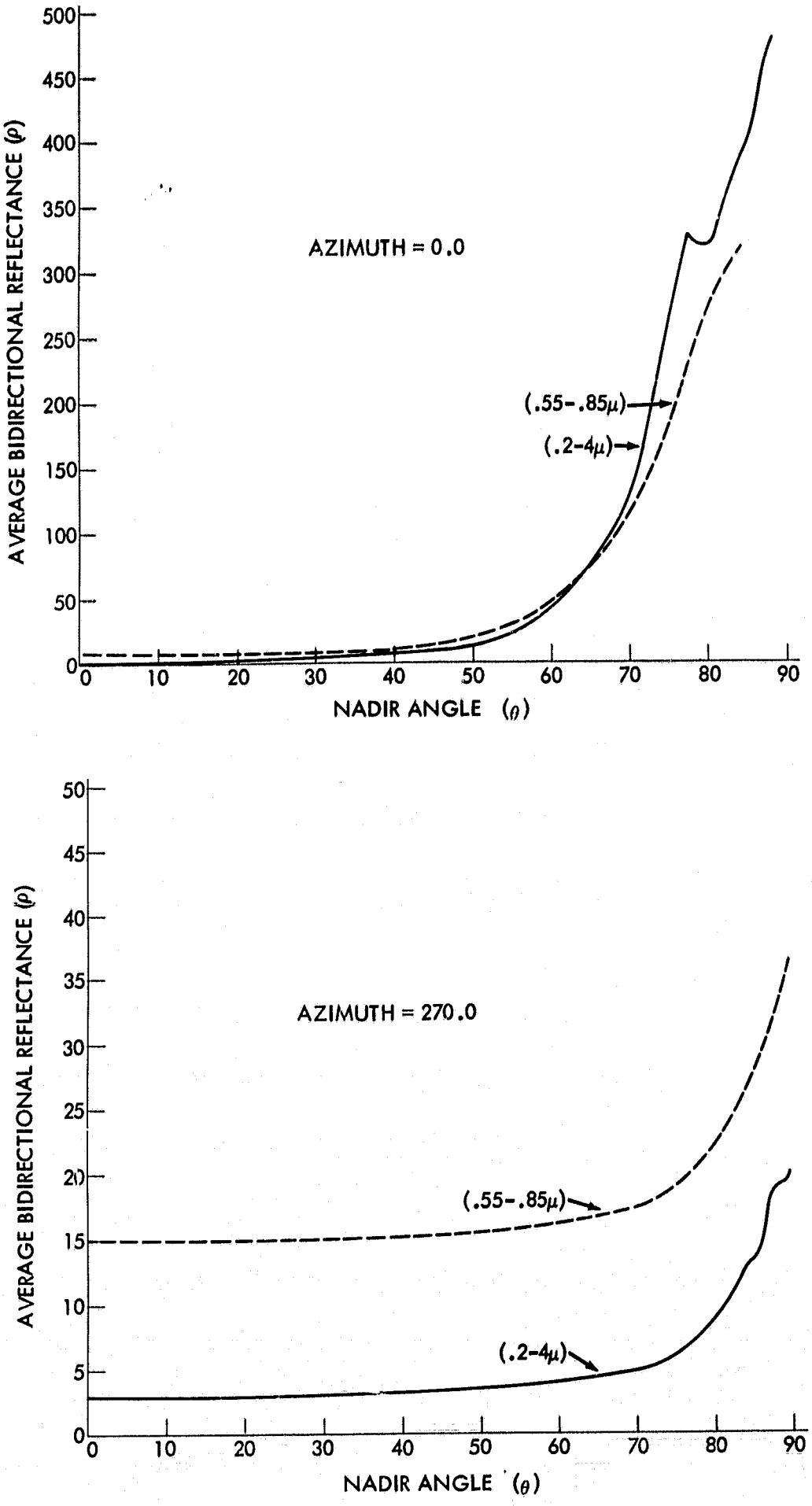

Figure 73–Bidirectional reflectances of Pacific Ocean at 34° 45′ W 121° 15′ W (aircraft at 29,000 ft), May 6, 1967, Day 126, Flt. 1. Solar Zenith 85.9-86.7°.

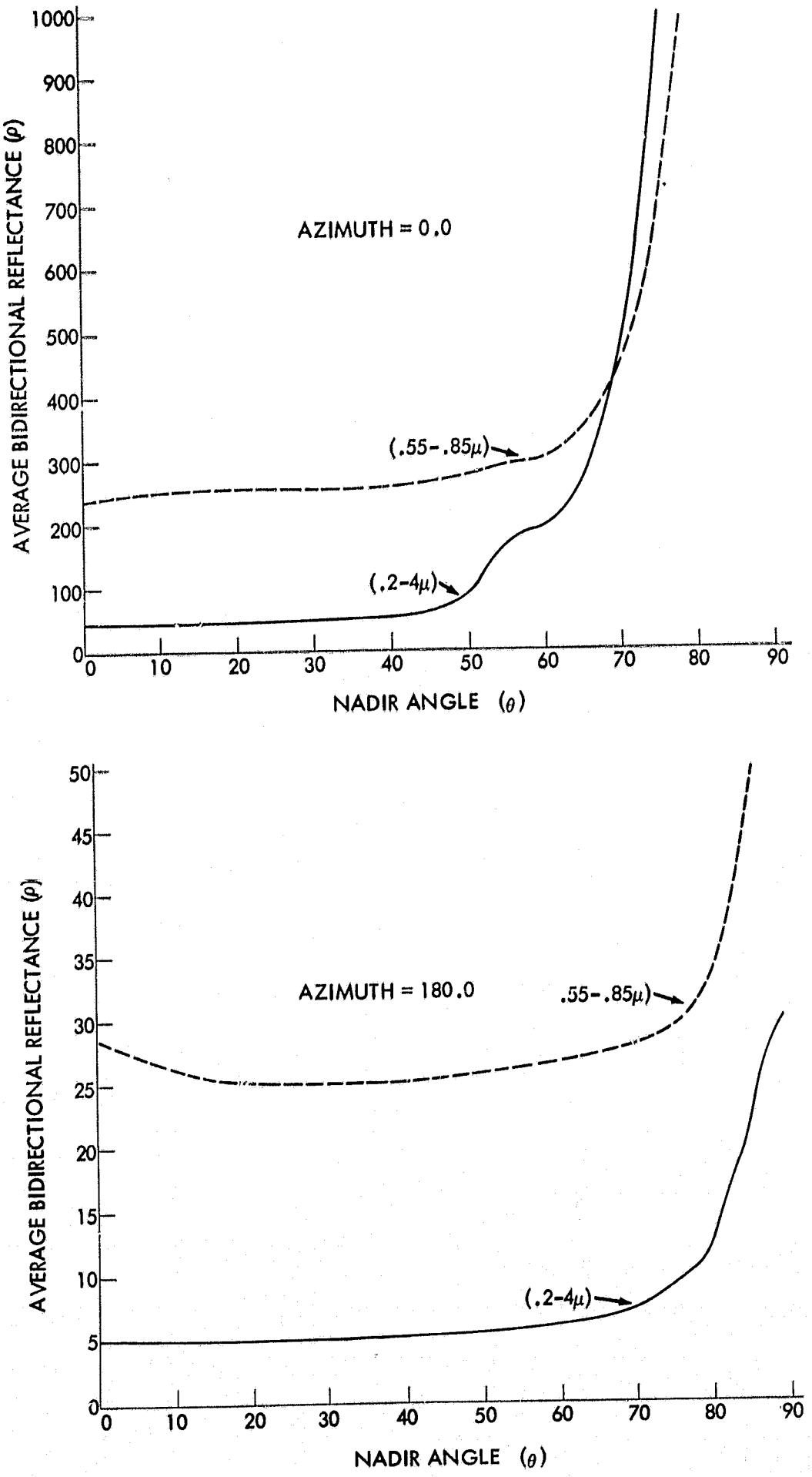

Figure 74–Bidirectional reflectances of Pacific Ocean at 34° 45' N 121° 15' W (aircraft at 39,000 ft), May 6, 1967, Day 126, Flt. 1. Solar Zenith 88.2-89.8°.